CERN-THESIS-2011-379

Proton-proton Collisions at the Large Hadron Collider's ALICE Experiment: Diffraction and High Multiplicity

Zoe Louise Matthews

Thesis submitted for the degree of

Doctor of Philosophy

Particle Physics Group,

School of Physics and Astronomy,

University of Birmingham.

November 20, 2011

Abstract

Diffraction in pp collisions contributes approximately 30 % of the inelastic cross section. Its influence on the pseudorapidity density is not well constrained at high energy. A method to estimate the contributing fractions of diffractive events to the inelastic cross section has been developed, and the fractions are measured in the ALICE detector at 900 GeV (7 TeV) to be f_D=0.278±0.055 (f_D=0.28±0.054) respectively. These results are compatible with recent ATLAS and ALICE measurements. Bjorken's energy density relation suggests that, in high multiplicity pp collisions at the LHC, an environment comparable to A-A collisions at RHIC could be produced. Such events are of great interest to the ALICE Collaboration. Constraints on the running conditions have been established for obtaining a high multiplicity pp data sample using the ALICE detector's multiplicity trigger. A model independent method to separate a multiplicity distribution from 'pile-up' contributions has been developed, and used in connection with other findings to establish a suitable threshold for a multiplicity trigger. It has been demonstrated data obtained under these conditions for 3 months can be used to conduct early strangeness analyses with multiplicities of over 5 times the mean. These findings have resulted in over 16 million high multiplicity events being obtained to date.

To Phil

Acknowledgements

"*Per Ardua Ad Alta*"

This motto has been staring at me from the University of Birmingham's crest for the past eight years of my life, and as I approach the completion of my PhD I can think of nothing more fitting.

I have been delighted to find that scientific research attracts many people with a similar philosophy to mine - an unquenchable interest in the world around them and a passion and determination to work for answers to the big questions. One of the most useful things physics has taught me is that the best rewards in life can be the most difficult to win. There is no better feeling than solidifying a concept in your mind, piecing it into place as part of a global jigsaw, after hours, weeks, months of struggling in the dark. This thesis has by far been the biggest challenge of my life to date, and the most rewarding journey.

People I would like to thank:

My Phil, for his unending support through the challenge of long-distance. For smiling through the stress of difficult times. For always pushing me to keep going. For setting the bar incredibly high. For sharing my passion for science. For having genuine interest in my work and making the effort to understand me. For the many cups of tea, meals cooked and hot baths run, and for the many nights divorced from me as I locked myself away working. For believing in me. For loving me.

My Mom, who has given me so much from the very beginning. For always being there, keeping me sane, reminding me of what's important. For being proud of her strange daughter. For being blown away by what I have achieved whilst still pushing me to go further. For picking me up after every knock. For countless chats on the phone. And, as the opportunities I have had for the past few years have been strongly time-dependent, for bringing me into being at just the right time.

My Dad, for his incredible strength. For many "taxi rides" and hugs. For answering my constant questions as best and honestly as he could, even if they were about parallax or Santa Claus. For

soothing the sobs when I lost hope, and having faith in my ability even when I didn't. For gushing to his work friends about me. For teaching me the importance of 1. up-to-date antivirus software and 2. a trip home every now and again.

My brother Connor for joining me in many daft experiments and exploits. For making me laugh on Skype when I lived far away and missed him like mad. For pretending he thinks I'm cool to make me feel good.

My Nan, for telling me at every opportunity that I can do anything I set my mind to. Because of her, the phrase "the world is your oyster" echoes in my mind and is reflected in my ambitions. My Grandad, who taught me my first words, how to solve the cryptic crosswords, and the joys of correcting other people's English. For listening to me, seeing great things in my future, and advising me to never stop singing. I know he would be so proud if he could see me now. My soon-to-be parents in law, and fellow thesiser Alex Kersting, for putting me up/putting up with me during those final days.

My school Physics teacher, Mr Russell, and Mathematics teacher, Mr Pearson, for loving their subjects so much, and encouraging my ambition. My Chemistry teacher, who shall remain unnamed, for inadequately answering my question about atomic nuclei defying Coulombic forces in an "it-just-does" fashion, sparking in me an interest in nuclear physics and a passion for honest, challenging teaching methods in later life.

Prof Peter Watkins, for jumping excitedly into a lecture hall one morning many years ago and dazzling me with the delights of CERN. From that day on particle physics became my favourite thing in the world, and I have never looked back. John Wilson, for many years as a tutor. For advice, guidance and a positive attitude. Alan Watson, for enlightening me to the utter madness of quantum mechanics, and for advising me that passion and hard work is more important than a flawless First Class academic record. Chris Hawkes, for shining a light on research. Paul Newman, for preparing me for good habits in statistics and warning me that even those in high places can be wrong sometimes. Lawrie Lowe, Mark Slater, Jan Fiete Grosse-Oetringhaus and Martin Vala

for saving me many times in technical or coding-related crises!

David Evans, for offering the incredible opportunity of working on the ALICE experiment. For being so passionate about the experiment that as a student I was inspired immediately. For being honest, and for looking out for the best interest of the group and his students. For many brilliant debates on science, religion, politics and education. For encouraging me to engage with schools and the public. For reminding me to have a life. For lending a mathematics book to me for a good 4 years without complaint (sorry about that, you will get it back).

Orlando Villalobos Baillie - for everything. For his honesty and enduring patience. For encouraging better habits. For never belittling a question but always having a note-book somewhere from years ago that has the answer in it. For being one of those rare Windows-using physicists, and as a result knowing all the best Windows-to-Linux software. For pointing me in the right directions at all the right times. For seeing my constant questioning as a positive attribute. For countless advice-for-life lines, any one of which I could have used as the quote for this thesis, but the most useful of which has been "Keep calm and carry on". For genuinely caring about my welfare. For being human.

Daniel Tapia Takaki, Marek Bombara, Lee Barnby, Roman Lietava, Cristina Lazzeroni, Gron Tudor Jones, Anton Jusko, Marian Krivda and Pedja Jovanovich, for help, kindness and patience. Mostly for putting up with me! Jean-Pierre Revol, Karel Safarik, Jurgen Schukraft and Federico Antinori, for appreciating the importance of my work and offering help and advice in early physics studies. Rainer Schicker for his interest in my work on diffraction.

Alberto Pulvirenti and the resonances group for their help in understanding the challenges in measuring the ϕ. The ALICE Soft Physics working group, for taking an interest in the potential for High Multiplicity p-p measurements and helping me to understand their implications; particularly those involved with Strangeness analyses, who assisted me in estimating the required statistics for reasonable measurements in this area.

James Daniel Bjorken for first proposing potential interest in High Multiplicity p-p collisions, and for taking the time to discuss with me the potential for ALICE to investigate this fascinating area. Johann Rafelski for fascinating and highly educational discussions on strangeness in quark-gluon-plasma. Giorgio Torrieri for his thought-provoking conversations.

Hamish Johnston and Michael Banks of Physics World, for the opportunity to bring new physics and funding issues to the public. The Times, in particular Mark Henderson, for making my voice heard on several occasions. Jane Panahy, Cecil Powell's daughter, for her moving letter in 2008. Those behind the relaunch of Quantum Diaries - I have loved being a part of it all these years. Lynne Long, Mohammed Ansar and the Birmingham STEM group, and all the teachers and staff who shared my enthusiasm for outreach and worked with me on various projects (including my dear friend Helen Walker and her colleagues at Calthorpe Park High School).

My St Genis neighbours Alex Martiniuk, Graham Jones, Gemma Fardell and Kyle Stevenson, and the other lovely folk of the CERN LTA collective, for emotional support via the medium of hugs, cups of tea, movies, food, RPG games and the occasional party. Also for enforcing the "no work after 6pm on a Friday" rule. I really appreciated that rule. David Hadley, Tim Martin, Chris Curtis, Owen Miller, Neil Collins, Angela Romano, Jody Palmer, Tony Price and other Birmingham PhD students past and present, for many beers, cake-breaks and sunny lunches on the grass. Tom McLaughlan for being a fellow giddy physicist and for keeping me singing. And of course my fellow ALICE buddies, Ravjeet Kour, Sparsh Navin, Arvinder Palaha, Plamen Petrov, Patrick Scott and Luke Hanratty. Wishing you all a happy and hopefully not too confusing future, far far away from the days of the RAL Summer School. I feel compelled to quote the Red Queen from Lewis Carroll's Alice Through The Looking Glass;

"Fan her head! She'll be feverish after so much thinking!"

Finally, I would like to thank the Science and Technology Facilities Council, for funding my PhD (and, as it turns out, my current employment) despite times of financial difficulty. I would also like to thank my employers, Marielle Chartier and Roy Lemmon, for seeing my potential, for giving

me the opportunity to work for them on a heavy ion experiment at GSI, which took place earlier this year, and for giving me the space and time to complete my thesis.

"Per Ardua Ad Alta: Through difficulties to the heights"

University of Birmingham motto

Contents

List of Figures

List of Tables

Glossary of Abbreviations and Terms

0.1 Acronyms and Initialisms

A-A Ion-Ion (pg 135)

A, C Sides of the detector. As a suffix, this may indicate a specific subdetector, e.g V0A and V0C. (pg 40)

ACORDE A COsmic Ray DEtector (pg 56)

ADC Analogue to Digital Converter. An ADC spectrum plots the pulse heights above threshold (signals that count as a hit) (pg 98)

AGS Alternating Gradient Synchrotron at Brookhaven National Laboratory (pg 11)

ALICE A Large Ion Collider Experiment (pg 1)

bc Bunch Crossings (pg 80)

BG Beam Gas (pg 79)

BRAHMS Broad RAnge Hadronic Magnetic Spectrometers at RHIC (pg 11)

CERN European Organization for Nuclear Research (pg 11)

CTP Central Trigger Processor (pg 2)

DAQ Data AcQuisition (pg 58)

DCA Distance of Closest Approach (pg 149)

DD Double Diffraction (pg 28)

DDL Detector Data Link (pg 59)

DPE Double Pomeron Exchange (pg 26)

EOS Equation of State (pg 22)

FMD Forward Multiplicity Detector (pg 43)

FPGA Field ProGrammable Array (pg 43)

GDC Global Data Concentrator (pg 59)

GFO Global Fast "OR" for the SPD (pg 44)

HLT High Level Trigger (pg 59)

HMPID High Momentum Particle IDentification detector (pg 56)

HV High Voltage (pg 44)

I, O Inner and Outer pixel chip layers (pg 120)

ITS Inner Tracking System (pg 39)

L0, L1, L2 Trigger Levels (pg 57)

LDC Local Data Concentrator (pg 59)

LHC Large Hadron Collider (pg 1)

LTU Local Trigger Unit (pg 57)

MB Minimum bias (pg 80)

MC Monte Carlo. The MC method is a kind of computing algorithm that uses random numbers to generate inputs, and is used for simulating particle physics events such as pp collisions at LHC (pg 1)

MRPCs Multi-gap Resistive Plate Chambers (pg 49)

NA49 A large acceptance hadron detector at CERN SPS (pg 16)

ND Non Diffraction (pg 70)

NI No Interaction (pg 80)

PHENIX Pioneering High Energy Nuclear Interaction eXperiment at RHIC (pg 11)

PHOBOS (not an initialism - named after a moon of Mars) RHIC experiment (pg 11)

PHOS PHOton Spectrometer (pg 56)

PID Particle Identification (pg 2)

PMD Photon Multiplicity Detector (pg 56)

p-p Proton-Proton (pg 1)

proc Process Type (pg 78)

$\mathbf{p_T}$ Transverse momentum (pg 12)

QCD Quantum Chromo-Dynamics (pg 2)

QED Quantum Electro-Dynamics (pg 5)

QGP Quark-Gluon Plasma (pg 2)

q, $\overline{\mathbf{q}}$ Quark, Anti-quark (pg5)

RHIC Relativistic Heavy Ion Collider (pg 3)

RICH Ring Imaging CHerenkov detectors (pg 56)

SD Single Diffraction (pg 28)

SDD Silicon Drift Detector (pg 41)

SPD Silicon Pixel Detector (pg 2)

SPS Super Proton Synchrotron at CERN (pg 11)

SSD Silicon Strip Detector (pg 41)

s, t Mandelstam Variables, see definition (pg 158)

STAR Solenoidal Tracker At RHIC (pg 11)

T0 ALICE forward timing Cherenkov counter array detectors (pg 52)

TOF Time Of Flight (pg 49)

TPC Time Projection Chamber (pg 2)

TRD Transition Radiation Detector (pg 49)

V0 ALICE forward scintillator counter array detectors (pg 50)

ZDC Zero Degree Calorimeter (pg 54)

ZEM Electromagnetic Calorimeter (pg 54)

ZN Neutron ZDC (pg 54)

ZP Proton ZDC (pg 54)

0.2 Terms

Beam-gas An event where beam particles interact with the gas in the beam-pipe (pg 79)

Coulombic Associated with electric charge (pg 7)

Coupling constant Indication of the strength of a force or interaction (pg 7)

Fugacity, Occupancy Fugacities, λ_i, relate to the chemical potential, μ_i, of quarks i, and $\mu_{\bar{i}}$, of antiquarks $\bar{i}$: λ_i=exp $\left(\frac{\mu_i}{T}\right)$, and $\lambda_{\bar{i}}$=λ_i^{-1}. Occupancies, γ_i, relate to how close the system gets to chemical equilibrium of quark flavour i, and these affect i and $\bar{i}$ equally. (pg 15)

Lorentz invariant Unchanging with relativistic "boosts" of the frame of reference (pg 9)

Multiplicity Number of particles produced in a collision (pg 2)

Perturbative QCD The use of perturbation theory in QCD to do calculations. This works best at high Q^2, low r region of QCD where α_s is weak. (pg 8)

Pile-up Multiple interactions in a single bunch-crossing (pg 120)

Pseudorapidity η, Rapidity Y See "Kinematics and Centrality", section 1.3.3 (pg 12)

Strangeness Measurement of particles with strange flavour quark content (pg 6)

x scaling In deep inelastic e-p collisions, x refers to the fraction of the proton's momentum carried away by a given parton. (pg 118)

Introduction and Author's Contribution

The Large Hadron Collider (LHC) and its experiments have been two decades in the making and are a result of the collaboration of thousands of scientists and engineers. The work contained within this thesis was undertaken at the end of this journey, and at the dawn of ALICE's (A Large Ion Collider Experiment) long awaited physics programme. The LHC circulated protons for the first time in late 2008, but soon afterwards shut down for over a year following a serious electrical fault. As a result, although the ALICE experiment's main objective is to study heavy ion collisions, much of the author's PhD work involved planning and developing early proton-proton (p-p) measurements. Data-taking began in November 2009, and it was then possible to begin putting these preparations to use. For this reason, the thesis contains studies using Monte Carlo (MC) simulation as well as early analysis using data from the LHC's first p-p collisions in the ALICE detector, at 900 GeV and 7 TeV centre of mass energy ($\sqrt{s}$). The LHC is the first particle accelerator powerful enough to produce 7 TeV p-p collisions, as well as the first to collide lead ions at $\sqrt{s}$=2.76 TeV per nucleon pair. The ALICE experiment is primarily designed for observation of these heavy ion collisions, in which a phase transition to a new form of matter is expected, and the p-p collisions are a vital standard candle for comparison. In addition to this, because the LHC p-p collisions break a new energy frontier, they also provide a completely new area of physics to explore.

The first chapter of the thesis introduces Quantum Chromo-Dynamics (QCD) and the quark-gluon plasma (QGP), explaining the physics motivation for the ALICE experiment and its heavy ion physics programme. It also motivates the experiment's interest in p-p physics and introduces the ideas behind the p-p analyses that were undertaken by the author. The second chapter introduces the LHC and describes the ALICE detector and its sub-detectors, focusing mainly on the detector capability that the author's work benefits from, particularly the Silicon Pixel Detector (SPD) and V0 detectors, used for triggering, and the Time Projection Chamber (TPC) used for Particle Identification (PID). It also goes on to describe the Central Trigger Processor (CTP), the particular responsibility of the Birmingham group, which has played a large role in obtaining and understanding the data used for the author's analyses. The chapter finally details some CTP firmware called "TooBUSY" that the author tested and developed software for. The resulting software tool has been very useful for diagnostic purposes during data-taking.

The subsequent chapters go on to describe the analysis undertaken by the author, starting with an estimate for the fractions of diffractive events contributing to p-p collisions at the LHC at 900 GeV and 7 TeV. This work was initially undertaken as part of ALICE's early p-p physics effort, in an attempt to estimate quickly the magnitude of the effect that these events have on the pseudorapidity distribution (although in the ALICE publication of this measurement a simpler estimate was used, not by the author, by simply comparing MC predictions for the fractions [1]). However, due to LHC delays, the method could be developed further alongside other detector measurements of diffraction. After introducing p-p diffraction and the challenges of measuring it, chapter 3 describes a study using MC to develop a way of measuring the fractions using a combination of measurement and MC simulation. The author developed this method as an extension of the UA5 experiment's strategy, and has summarised it in an ALICE internal note [2]. The chapter goes on to describe the various stages of development of the method from a MC study to a real data analysis. Finally, the author's measurement at 900 GeV and 7 TeV is presented and compared to recent findings.

Chapter 4, split into three parts, describes the author's work investigating p-p collisions with high-multiplicity (HM, large number of particles in a collision). The first section describes work

carried out by the author to obtain the data sample using a trigger. It begins by motivating the analysis of such events, as well as describing ALICE's capability in obtaining an enhanced sample of such events using a multiplicity trigger and analysing them effectively. It then describes the main background contribution, and how it can be understood using Poisson probability. In addition to simulating the effect background would have on the multiplicity distribution, the author has also developed a method for extracting the multiplicity distribution of pure events given their probability, described in the text. The section explains how this method was tested and developed, and finally used with real data in order to calculate the purity of a sample of high multiplicity events given a trigger threshold. This was combined with data-taking rate limitations to choose an optimum high multiplicity trigger threshold. The method was used successfully in obtaining a large sample of high multiplicity events ready for analysis.

As will be explained, given the high energy density that could be involved, much interest lies in investigating whether p-p events with high multiplicity at the LHC might produce a similar environment to that seen in central heavy ion collisions at the Relativistic Heavy Ion Collider, RHIC. For this reason, observables of interest for heavy ions are also of great interest in p-p data. The next section of Chapter 4 describes one of these probes, strangeness, which involves measuring the yields of particles with strange quark flavour. First the current understanding of strangeness in heavy ion vs p-p collisions is described, and expectations for high-multiplicity are discussed. This section then describes a feasibility study carried out by the author to see how much can be achieved in three months of data-taking. It begins by taking an approximation to the required statistics for various strangeness analyses and scaling to high multiplicity. This was carried out with assistance from the ALICE Soft Physics working group. The author's method for estimating purity of the rare trigger data sample is then used to see how high in multiplicity an enhanced sample, taken over three months, could reach (expressed as a trigger threshold), whilst obtaining the required statistics for each strangeness analysis. The results are very promising and have since been supported by successful acquisition of a large quantity of high-multiplicity events. The studies in these sections are summarised in a paper written by the author for the proceedings of an oral

presentation at the Strangeness in Quark Matter conference, 2009 [3].

The final part of the chapter focuses on one of these strangeness analyses - the $\phi(1020)$ resonance - and motivates interest in the production of such a resonance in heavy ion vs p-p collisions. A summary of this motivation is described in a paper written by the author for proceedings of a poster presentation at the Quark Matter conference 2008 [4]. The section describes the current difficulty in understanding measurements of ϕ to date, and what makes it especially interesting at high multiplicity. The method of detection and analysis of ϕ via the K^+K^- channel is described, and the author takes a very early look at the ϕ yield in 7 TeV collisions. This includes an early measurement supporting previous MC studies in the idea that ϕ can be measured in p-p even in the absence of PID, followed by an improvement of low p_T significance by using limited TPC PID information.

Chapter 5 concludes on the author's diffraction and high multiplicity work.

Chapter 1

Theory

1.1 The Standard Model

Experiments using high energy electrons have shown that atomic nucleons, protons and neutrons, are made up of "up" and "down" flavoured quarks [5]. They are held together by massless gluons, the mediators of the strong interaction, described by Quantum Chromo-Dynamics (QCD) [6]. As shown in Figure 1.1 (current accepted values taken from [7]) other, more massive quark flavours exist ("strange", "charm", "bottom" and "top"), and nucleons are part of a zoo of particles known as hadrons that can be created from different combinations of these quark flavours.

As well as having a fractional electric charge, as also indicated in Figure 1.1, quarks (q) possess a colour charge, (red, green or blue). This colour charge is analogous to the electric charge described by Quantum Electro-Dynamics (QED). However, unlike the electromagnetic force carrier, the neutral photon, gluons also possess colour charge (colour, anti-colour). Free quarks are not observed in nature, and instead they are confined to the (colourless) hadrons, as qqq bound states called baryons, such as nucleons, or as $q\bar{q}$ states called mesons, such as pions. Other states, such as pentaquarks ($qqq\bar{q}q$), glueballs (gg, ggg) and hybrids ($q\bar{q}g$) are also theoretically possible, but

have not been established definitively by experiment [8].

In addition to having the quantum numbers J (spin), P (parity), C (charge conjugation) and m (mass), hadrons also have flavour quantum numbers, e.g. I (isospin, representing the ratio of up quarks to down quarks) and S (strangeness, where a strange quark has -1 "strangeness", and an anti-quark has +1 "strangeness"). B (baryon number, 1/3 for quarks and -1/3 for anti-quarks) is 1 for baryons and 0 for mesons. Leptons possess a lepton number, which is zero for hadrons.

QCD predicts that at very high energy density, these quarks and gluons can become deconfined, making a state of matter known as Quark Gluon Plasma (QGP).

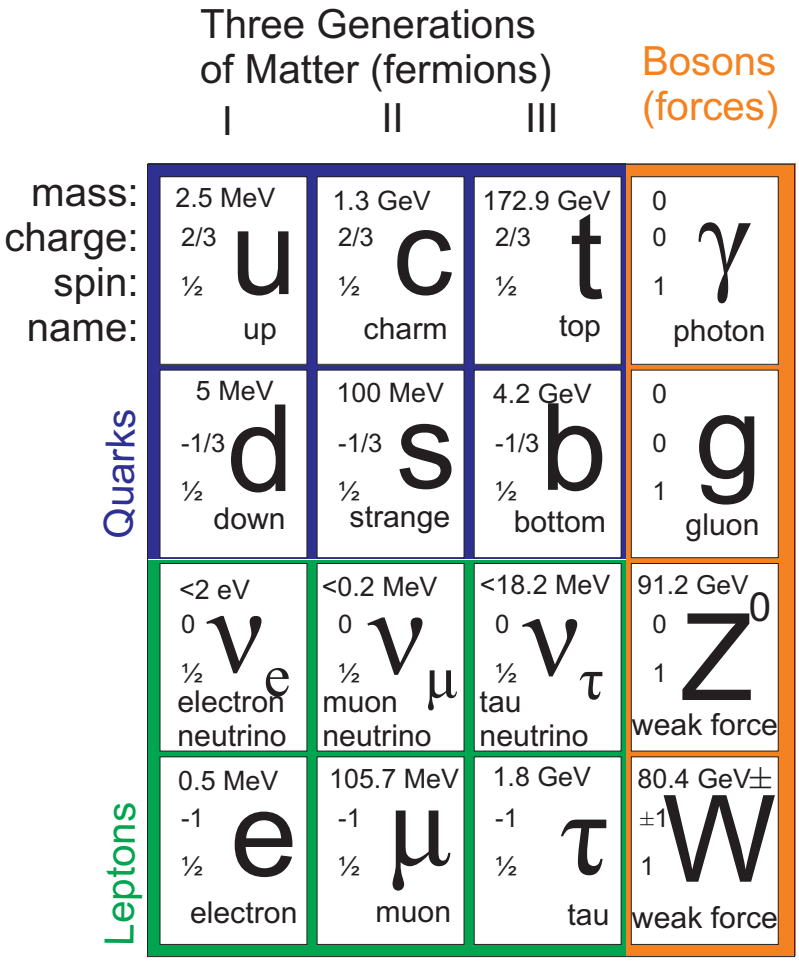

Figure 1.1: The quarks, leptons and bosons of the Standard Model.

1.2 Quantum Chromodynamics (QCD)

The QED and QCD potentials at first appear similar. In the case of an electric charge, the potential increases as the separation between charges decreases:

$$V(r) \propto -\frac{A}{r}. \tag{1.1}$$

In the case of QCD, a Cornell potential model can be used [9]:

$$V(r) \propto -\frac{A(r)}{r} + Br. \tag{1.2}$$

For small distance r, the potentials appear to behave in the same way, and for this reason the first part of the potential is referred to as the "Coulombic" term. However, as the quarks are separated, increasing r, the additional term dominates, causing the potential to increase. The increasing energy needed to separate the quarks eventually creates a new $q\bar{q}$ pair. In this way, the quarks cannot be separated and are confined to colourless hadrons.

In addition to this, the QED and QCD coupling constants vary with r, Q^2, and they behave quite differently. Because of the self-interaction of gluons, an increase in Q^2 has the opposite effect on the effective strong coupling constant $\alpha_s(Q^2)$ to that on the effective electromagnetic coupling constant $\alpha_{em}(Q^2)$. $\alpha_{em}(Q^2)$ increases [10], whereas $\alpha_s(Q^2)$ gets smaller. This is known as a running coupling constant.

In the QED case;

$$\alpha_{em}(Q^2) \approx \alpha_{em(0)}(1 + \frac{\alpha_{em(0)}}{60\pi^2}\frac{Q^2}{{m_e}^2}). \tag{1.3}$$

In the case of QCD,

$$\alpha_s(Q^2) \approx \frac{1}{(b \ln \frac{Q^2}{{\Lambda_{QCD}}^2})}, \tag{1.4}$$

where ${\Lambda_{QCD}}^2$ is a scale parameter and

$$b = 11N_c - 2n_f \tag{1.5}$$

where n_f is the number of flavours and N_c is the number of colours [6, 8]. This b term is dominated by the self interaction of gluons, making up the term $11N_c$. These equations show that an increase in Q^2 has the opposite effect on α_s as α_{em}.

Although various models have been used to attempt to describe the matter produced in heavy ion collisions, the equation of state is not known, and determining it is a major goal for particle and nuclear physics. In the asymptotically free environment of high Q^2 and small r, a perturbative approach to QCD can be used (perturbation theory). However, describing confined matter and the phase transition to a QGP in heavy ions using perturbative QCD is not appropriate because, where the energy scale is low and α_s is strong, "high-order" contributions to the interactions are no longer perturbations from a simple picture but dominate. Here, non-perturbative "Lattice QCD" calculations can be carried out, which simulate quarks on a lattice and provide thermodynamic predictions for phase-transitions [11].

The early Universe, up to 10 microseconds after the Big Bang, is thought to have been a Quark Gluon Plasma. Both perturbative QCD and Lattice QCD calculations predict that this form of matter will exist at very high temperatures above around 170 MeV, which corresponds to around 10^{12}K. In this way, high energy heavy ion experiments like ALICE aim to recreate this form of matter and probe its properties, in order to try to better understand the nature of the strong interaction.

1.3 QCD Phase Transitions

1.3.1 Chiral Symmetry

The helicity, or handedness, of a particle is the projection of its spin σ on to its momentum $\mathbf{p}$:

$$\frac{\sigma.\mathbf{p}}{|\mathbf{p}|} \tag{1.6}$$

If quarks were massless, their left and right handed helicity would be conserved. Because of the finite mass of quarks, helicity cannot be a perfectly conserved quantity - it is always possible for an observer traveling close to the speed of light to change the observed helicity [12]. Instead, a Lorentz invariant quantity called "chirality" is considered, equivalent to Helicity in the case of zero quark masses. If this were a conserved quantity, a "chiral symmetry" would exist in the universe. However, even this symmetry is broken in the QCD Lagrangian, because of finite hadron quark masses [6].

The mass of a hadron is observed to be much greater than the sum of the masses of its bare quarks. Part of this additional mass is thought to be caused by the spontaneous breaking of chiral symmetry, giving rise to a "constituent mass" of quarks, around 300 MeV for up and down quarks. Only partial chiral symmetry can ever exist because the bare quarks themselves have finite mass, leading to an explicit chiral symmetry breaking in the QCD Lagrangian, which cannot be removed. Heavy ion experiments hope to probe this effect, by bringing about the partial restoration of this symmetry in collisions and studying the effects on particles produced in QGP.

1.3.2 Quark Gluon Plasma

Figure 1.2 shows a phase diagram in temperature and baryo-chemical potential, μ_B, where μ_B relates to the net Baryon number of a system. μ_B is zero in a vacuum, and around the mass of a nucleon for nuclear matter. The QGP of the early Universe is described by the region where

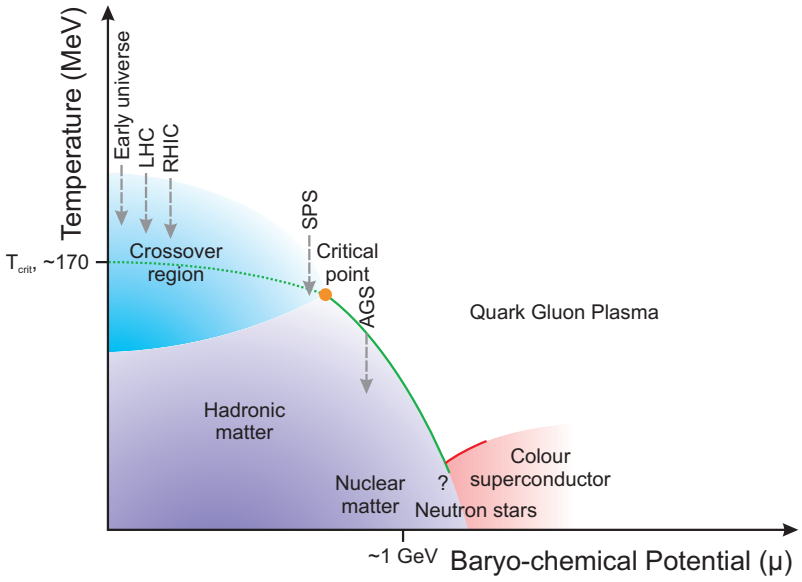

Figure 1.2: The QCD phase diagram.

μ_B is almost zero, and temperature is high, where matter and anti-matter were produced in equal amounts. Heavy ion collisions produce less high temperatures, with small but finite baryo-chemical potential, because of the ion valence quarks. The LHC produces collisions at higher energies than before, reaching not only higher temperatures but smaller μ_B values than previous experiments. This is because in such collisions QGP is formed at central "rapidity" (See "Kinematics and Centrality", in this section). At higher energies the valence quarks are pushed to more forward rapidity regions and replaced with the new $q\bar{q}$ pairs produced in equal amounts in the collisions.

The phase transition to a QGP can either be a first order transition, or, beyond the critical point, a higher order transition. The value of the critical temperature T_{crit} indicated in Figure 1.2 is predicted by Lattice QCD. The M. I. T. bag model [13] describes hadrons as potential wells containing quarks which move freely within them. In this model, the region outside the potential is of high pressure. The phase transition from deconfined to confined quarks occurs when these pressures are equal, at a temperature of around 170 MeV (or $\sim 10^{12}$ K).

The early Universe is thought to have existed in the form of a QGP until around 10 microseconds after the Big Bang, when the energy density dropped to below around 1 GeV/fm^{-3} . At this

stage, the medium was extremely low in net baryon density, since $\frac{N_b}{N} \simeq 10^{-10}$, where N is the total number of particles. The baryon number density of the system depends on μ [14].

The maximum temperature achieved in collisions at ALICE is expected to far exceed T_{crit}, and it should be possible to reach a point above the crossover region indicated in 1.2, where a complete transition to QGP can take place.

1.3.3 QGP in Heavy Ion Collisions

Previous heavy ion accelerators and the areas of the strongly interacting matter phase diagram they have explored in collisions are indicated in Figure 1.2. Experiments at the AGS (Alternating Gradient Synchrotron), Brookhaven looked at collisions of silicon and gold nuclei at incident beam momenta of up to 15 GeV/c per nucleon ($\sqrt{s}$=5.5 GeV/nucleon) from 1992 (e.g. [15]) , whilst CERN's SPS used beams of oxygen, sulphur and lead ions, at momenta up to 200 GeV/c per nucleon ($\sqrt{s}$=19.42 GeV/nucleon), until 2003 [16]. RHIC collided a combination of heavy ions, reaching up to 200 GeV per nucleon [17]. Its four detectors are STAR [18], PHOBOS [19], PHENIX [20] and BRAHMS [21], and in the relativistic energy collisions, new signatures for QGP were observed (see Section 1.6).

The environment in which QGP existed in the early Universe was quite different to that in which it is formed in heavy ion collisions. The baryon density is initially much greater in the A-A case because the initial collision begins with the two ions. The higher energy the collisions reach, the more $q\bar{q}$ pairs are produced and the smaller μ_B becomes. These effects reduce the net baryon number density. In the LHC collisions μ_B should be negligible [22].

In ALICE, the QGP exists for only around 10 fm/c or 10^{-22} seconds [22], before expanding and cooling. The evolution of a heavy ion collision is shown in more detail in Figure 1.3. The ions are shown in the centre of mass frame as "pancakes", because of Lorentz contraction caused by their relativistic velocities.

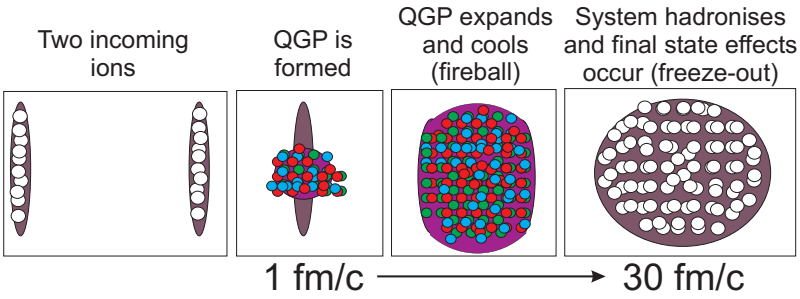

Figure 1.3: The time evolution of QGP in a heavy ion collision.

Thermal equilibrium in LHC Pb-Pb collisions is expected to occur after around 0.1 fm/c [22]. Provided this temperature exceeds the critical limit, QGP should exist here, and is expected to exist in LHC Pb-Pb collisions for around 10 fm/c. The energy density is expected to be up to 150 GeV/fm^3 [23] - far beyond that required for the phase transition. Chemical equilibrium is governed by the temperature, baryo-chemical potential μ, and respective masses. It is thought to be reached first for u and d quarks and later for heavier quarks, before the QGP cools.

As the plasma cools, it expands, dropping in temperature. This hot dense system is usually referred to as a "fireball". The particles "hadronise", forming confined hadrons, but another stage continues, known as "freeze-out", lasting 30-40 fm/c. Here, final state effects such as rescattering and recombination occur, until the point where interactions cease and final state particles remain.

Kinematics and Centrality

There are certain variables used for analysis in heavy ion physics and high energy physics which it is useful to define for clarity. Rapidity is a variable described by the following equation;

$$y = \frac{1}{2} \ln \left[\frac{E + p_z}{E - p_z} \right], \tag{1.7}$$

where p_z and E are the longitudinal momentum and energy of the particle respectively. (Let us here also define p_T - transverse momentum.) The shape of the distribution of rapidity in a collision

is invariant under boosts along the z (beam) axis.

Another variable, dependent on the angular distribution, is pseudorapidity,

$$\eta = -\ln\left[\tan\left(\frac{\theta}{2}\right)\right], \tag{1.8}$$

where θ is the angle between the momentum $|\vec{\mathbf{p}}|$ and the z axis. Unlike rapidity, it does not require the measurement of the energy of the particle. In the relativistic limit, pseudorapidity and rapidity are similar. In this way, when describing the "forward" region of the detector, which refers to high $|\eta|$, this can usually be thought of as the high end of the rapidity range.

Figure 1.4 shows the geometry for collisions of varying centrality.

It is useful here to define the "impact parameter" b of a heavy ion collision, or the "distance of closest approach" of the colliding nuclei. It is defined as the smallest distance between their central points, in the xy plane, shown in Figure 1.4. It is clear that for central collisions this is zero, and the more peripheral a collision, the closer to the sum of the two radii b becomes.

Using this, one can define the "reaction plane" of the collision, as the plane between b and the momentum vector of the colliding particle in its centre of mass. This is a useful plane to consider for certain heavy ion measurements such as elliptic flow (see Section 1.3.5).

The amount of overlap of the ions in the event roughly, but not completely, correlates with the pseudorapidity density of the remnants. Generally, the more central a collision, the greater is the multiplicity, as more nucleons are involved in the interaction. However, in the text, reference to a "central" collision (small impact parameter) should not be confused with reference to a "central" region of pseudorapidity, as these are not related. "Central" and "forward" pseudorapidity refers to low and high values of η respectively.

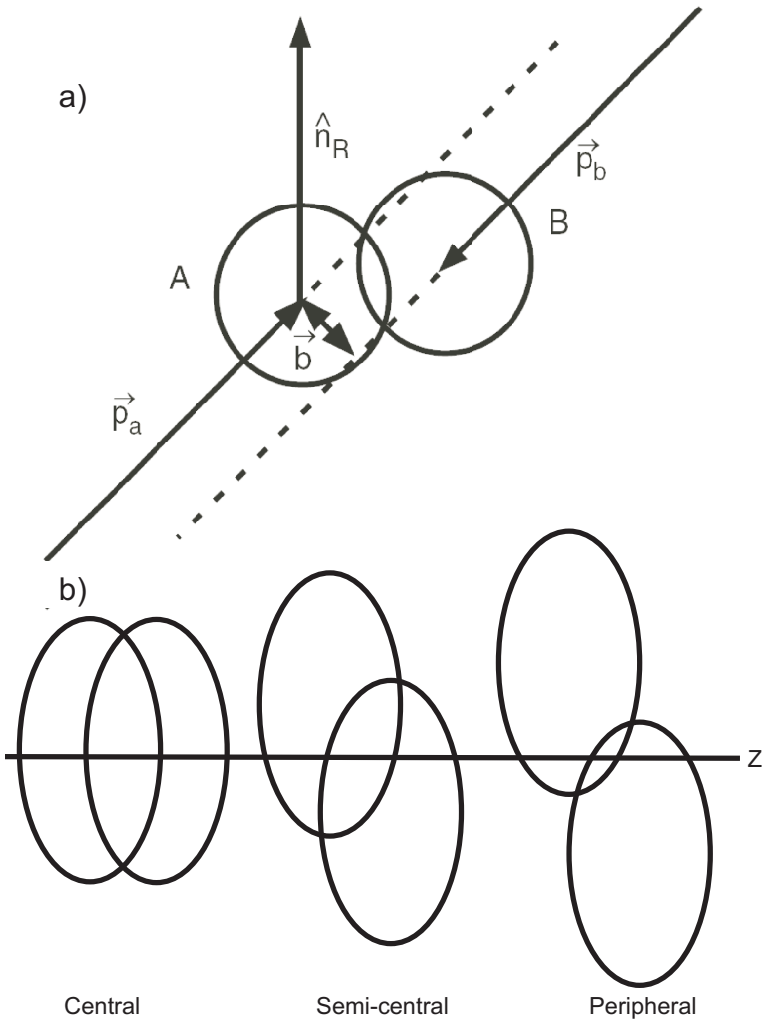

Figure 1.4: (a) The impact parameter b and the "reaction plane". (b) Central, semi-central and peripheral collisions.

1.3.4 Evidence for QGP: SPS

The presence of deconfinement and the properties of a QGP are not seen directly. Instead, the final-state particles measured in the detectors are used as indicators. Certain effects on these observables are predicted following the presence of a QGP, or can probe its properties. These effects are known as QGP "signatures" and some are outlined below.

Strangeness in QGP

The hadrons observed following a heavy ion collision are believed to be produced with relative abundances based on their quark content, assuming chemical equilibrium is reached, because flavour-production ratios are thought to be governed by the "fugacities" and "occupancies" of the quarks [24]. If the system lives long enough, strangeness production can reach chemical equilibrium in A-A collisions.

In a QGP, strangeness production should occur more quickly than in a hadron gas. This is partly because of deconfinement - interactions are with quarks rather than hadrons. However, chiral symmetry also plays a role. As previously described in Section 1.3.1, broken chiral symmetry causes quarks to have a higher, "constituent" mass. For example, if chiral symmetry were to be partially restored in an A-A collision, strange quarks would have their bare mass of $\sim$ 125 MeV, rather than the $\sim$ 550 MeV mass they have in normal strange matter. The lighter s quark mass is of the order of the temperature of QGP, which leads to unbound strange quark anti-quark pairs being produced abundantly. This fast chemical equilibration leads to a predicted strangeness enhancement with respect to proton-proton collisions, and a larger enhancement for particles with larger strange quark content. As freeze-out occurs, the system "hadronises", and the global quark flavours are conserved as they are bound into hadrons.

In a thermodynamic hadron-gas picture, where no QGP is formed in heavy ion collisions, strangeness enhancement is still predicted (or, rather, suppression of strangeness in proton-proton collisions

with respect to A-A collisions), because of the limited volume of the p-p system. This enhancement is expected to increase in hadrons with higher net strangeness. This means that there is no predicted enhancement of the $\phi(s\bar{s})$ resonance, which has no net strangeness. An important point to note is that this interpretation assumes chemical equilibrium is reached in both p-p and A-A systems.

Strangeness enhancement in heavy ion collisions was observed at AGS [25]. Further observations showed that the more strange quark content a particle has, the more its yield increases - as seen by SPS experiments [26], [12]. For example, for Λ, with strangeness of 1, the multiplicity per participating nucleon in heavy ions was around double that in p-p collisions, but for the strange hyperon Ω, which contains sss, an enhancement of 20 times that of p-p collisions was seen at WA97 [27].

For more discussion, see Section 4.2.

Resonances and QGP

Whilst most hadrons form during the hadronisation phase, some can form very quickly. Resonances have short lifetimes, such that they only travel distances comparable to the size of the QGP, and some could decay before freezeout [28], [29]. Therefore, by reconstructing their decay products to observe any mass shifts, they could provide a potential probe of partial chiral symmetry restoration within a QGP. If they decay hadronically, their masses and mass widths are susceptible to possible final state effects that may happen as the fireball cools. In the case of a leptonic decay, the decay products are not strongly interacting and so are not affected by this process, meaning mass shift effects can be more clearly identified.

The ϕ meson, a resonance made up of $s\bar{s}$, with a lifetime of 44 fm/c, is a particularly interesting resonance not only for mass and width measurements but also for the study of strangeness enhancement. In the NA49 experiment [30], and the STAR experiment [31], the ϕ yield per participating

nucleon in heavy ions was measured to be several times enhanced with respect to p-p collisions despite having no net strangeness - an effect not described by thermodynamic hadron gas models.

For more detail, see Section 4.3.

Quarkonia Suppression

Another signature, first predicted by Matsui and Satz [32] and expected by Lattice QCD calculations [33] is the suppression of heavy quarkonia, by a phenomenon known as "colour screening" - a QCD effect analogous to Debye screening. Consider again the QCD potential at short range. At zero temperature it follows:

$$V(r) \propto -\frac{\alpha_{eff}(r)}{r} \tag{1.9}$$

In fact, at finite temperature, it becomes;

$$V(r,T) \propto -\frac{\alpha_{eff}(r)}{r} \exp\left(-\frac{r}{r_D(T)}\right) \tag{1.10}$$

where r_D is the "Debye radius", which decreases with increasing temperature. This contribution means that a bound system with a large radius relative to r_D will be "melted", as the potential between its constituent particles is screened.

The J/ψ meson ($c\bar{c}$) was predicted to be "melted" at temperatures above the critical temperature needed to form a QGP, making it a very interesting measurement in the field, and the suppression effect was observed at the SPS [34]. Other, hadronic interpretations of this measurement exist [35]. At RHIC and LHC energies the high temperature means many c$\bar{\text{c}}$ pairs are produced in the plasma, leading to a possible relative increase in J/ψ production during freeze-out (recombination). In fact, ALICE observes less suppression than was observed at RHIC [36]. The excited states of ψ, with larger radii, are expected to melt at lower temperatures. The Υ meson ($b\bar{b}$) is expected to be suppressed at higher temperatures because of its larger mass.

1.3.5 Evidence for QGP: RHIC

Jet Quenching

"Hard interactions" in p-p/A-A collisions are parton-parton interactions that result in two back-to-back high p_T partons, e.g. quarks. In ordinary matter, colour-confinement means that as the quarks separate, fragmentation and gluon radiation occurs and "jets" (high p_T hadronic showers) form. Jet quenching, predicted first by Bjorken [37] and later by Wang and Gyulassy [38], is an effect that was first seen at RHIC in Au-Au collisions at $\sqrt{s} = 200$ GeV [39], [40], [41].

Within a QGP, the quarks do not need to fragment - only once they are confined to colourless hadrons does this occur. Instead, as they travel through the dense medium they lose energy by radiating gluons. This effect is shown in Figure 1.5 (taken from [42]). The quark that travels through most plasma suffers the most energy loss, and the resulting jet can be suppressed or even completely absorbed. This is what was seen at RHIC in Au-Au collisions, as shown in Figure 1.6 [40]. The effect is largest for particles with p_T of around 10 GeV/c in central collisions, and is quantified by the value R_{AA}:

$$R_{AA}(p_T) = \frac{d^2N^{AA}/dp_T d\eta}{T_{AA} d^2\sigma^{NN}/dp_T d\eta} \tag{1.11}$$

where T_{AA} is the scale factor related to the number of binary NN collisions expected for a given centrality, $\frac{<N(binary)>}{\sigma^{pp}_{inelastic}}$. Essentially, R_{AA} is a measure of the deviation of measured A-A particle distribution with respect to proton-proton collisions, as a function of p_T and centrality. The R_{AA} for the RHIC data given in [39] is shown in Figure 1.7. At LHC, sufficiently high momenta are reached that some partons can punch through the plasma, and so R_{AA} rises again at very high p_T. These results are also shown in Figure 1.7 [43].

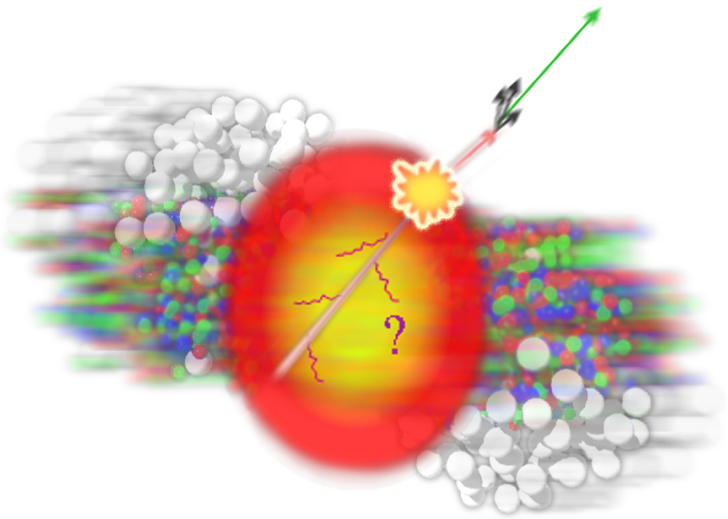

Figure 1.5: Visual representation of a jet's energy being lost in QGP.

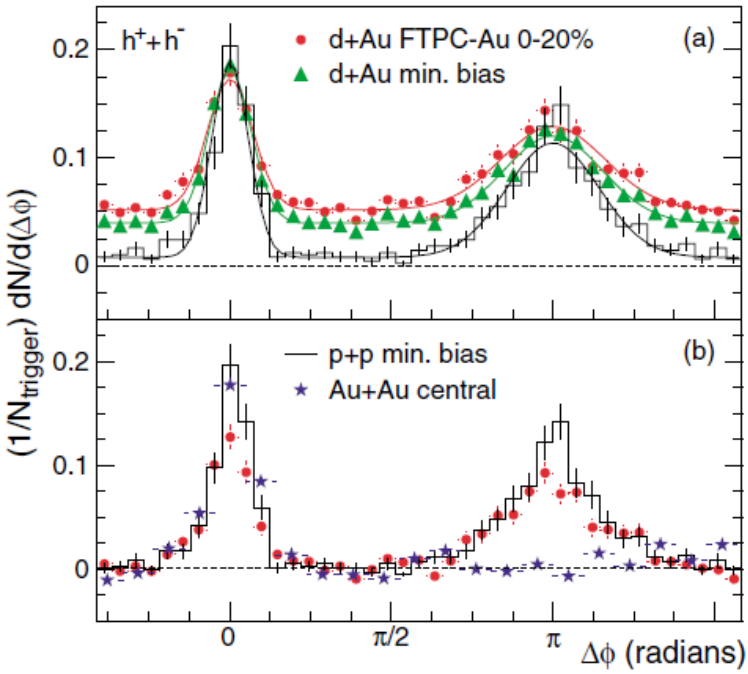

Figure 1.6: (a) Two-particle azimuthal distributions for minimum bias central d-Au collisions and p-p collisions. (b) Comparison of two-particle azimuthal distributions for central d-Au collisions to those seen in p-p and central Au-Au collisions.

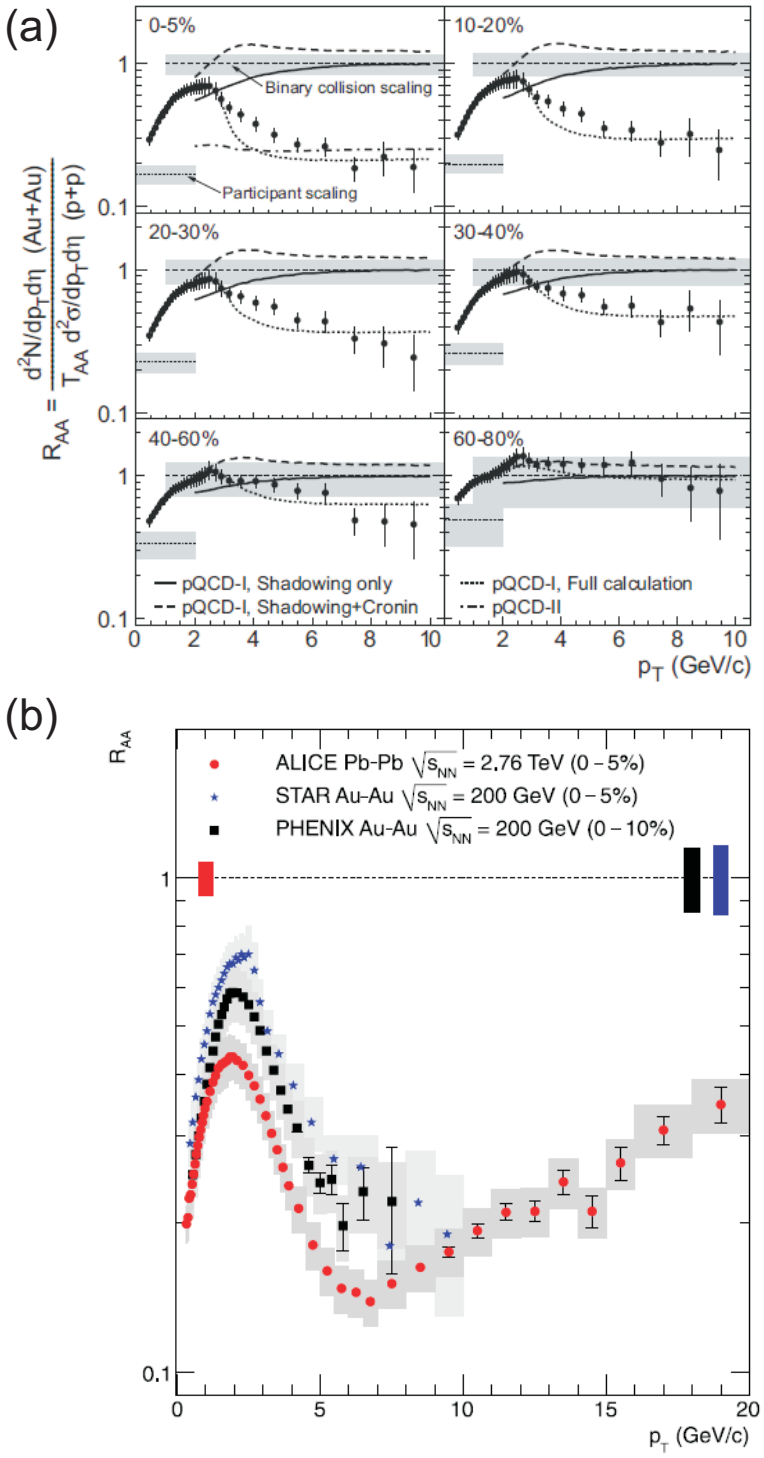

Figure 1.7: (a) R_{AA} as a function of p_T, $|\eta|$ <0.5, $\sqrt{s}$ =200 GeV, for varying centrality, in Au-Au collisions at RHIC. 0-5% is most central, 60-80% is most peripheral. (b) R_{AA} as a function of p_T at ALICE for most central Pb-Pb collisions at LHC ($\sqrt{s}$=2.76 TeV), compared with RHIC results.

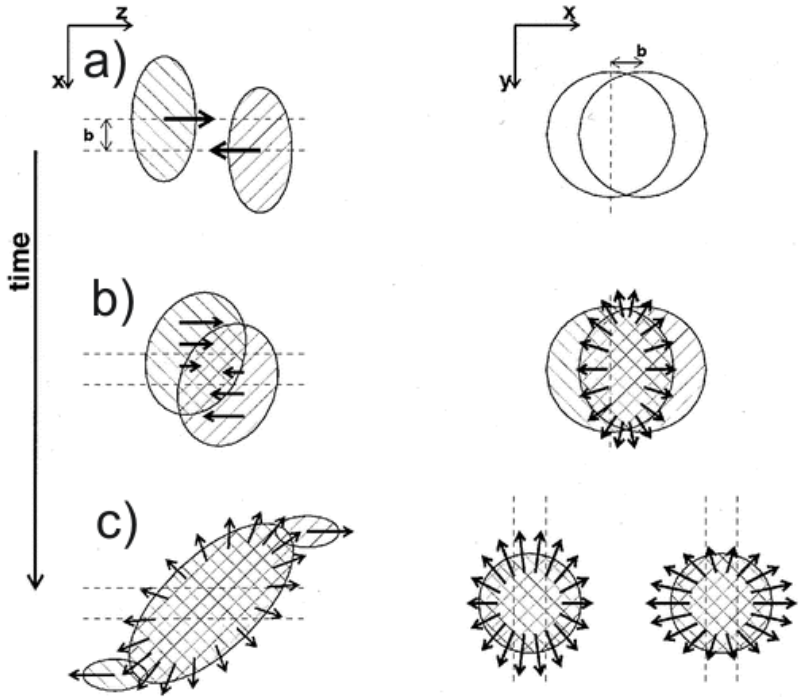

Figure 1.8: (a) A schematic representation of 'flow' indicating the reaction plane and overlapping ellipse. (b) The pressure gradient as it varies with ϕ. (c) The resulting transverse momentum ellipse. Taken from [50]

Flow

Another interesting measurement in heavy ion collisions, sensitive to early-evolution effects (such as rescattering), is the 'flow' [44], or 'collective motion' of the collided system in a preferred direction. The azimuthal flow of momentum of particles in a heavy ion collision can be simply radial (symmetric in ϕ), or anisotropic in the transverse plane. Anisotropic transverse flow was first measured at the Berkeley Bevalac [45], and has since been observed at AGS [46], SPS [47], RHIC [48] and LHC [49].

Transverse flow in heavy ion collisions is measured as an anisotropy in ϕ of the momentum distribution of particles in the collision with respect to the 'reaction plane' - the plane defined by the impact parameter (as a vector) against z, as shown in figures 1.4a and 1.8a. This can be

quantitatively described by expanding the azimuthal angle distribution in a Fourier series,

$$\frac{dN}{d\phi} = 1 + v_1 \cos\phi + v_2 \cos 2\phi + ...v_n \cos n\phi, \tag{1.12}$$

where harmonics v_n contribute to the anisotropy, much of which is thought to arise in the first few fm/c. v_1 is known as 'directed flow', and v_2 as 'elliptic flow'. In non-central collisions there exists an initial spatial anisotropy - an overlapping ellipse in the transverse plane, as shown in Figure 1.4b, whose width is given by b. At very low energies, this causes a preferred direction for the Coulombic deflection of surface nucleons in the reaction plane (along b). In collisions at around 400 MeV per nucleon and above, the elliptical region of overlap causes pressure gradients to arise as shown in Figure 1.8b. In these collisions, the spectator nucleons (those not involved in the interaction) have some stopping power and particles are "squeezed out" perpendicular to the reaction plane, measured as negative v_2. This kind of flow holds information about compressed, high density nuclear matter. With increasing energy, particles such as pions can begin to be produced in the collisions, and less flow is measured at mid rapidity. From around 2 GeV per nucleon, "side-splash" (v_1) of nucleons involved in the interaction is seen at increasing rapidity.

In very high energy collisions such as those at RHIC and the LHC, the overlapping region can be thought of as a bulk system of partons responding to the pressure collectively. Spectator nucleons escape the collision much faster than at lower energies and the initial pressure gradients are able to evolve into an in-plane elliptic momentum anisotropy during the expansion of the system, as shown in Figure 1.8c. There has been great interest in elliptic flow because variation in pressure gradients with density is linked to the nuclear equation of state and viscosity [51]. Rescattering of particles during freeze-out can also contribute.

It is important to note that 'non-flow' effects, such as jets or resonances, as well as a small multiplicity, can also cause anisotropy in ϕ (which would not be correlated with the reaction plane). The key difficulty with measuring flow is that the 'reaction plane' cannot be measured *a priori*, and there are various ways to calculate it, each of which has its limitations, [44].

Hydrodynamical models link flow measurements to the EOS and viscosity of the system, in par-

ticular through the interpretation of v_2 [52]. In fact, the interest is in the viscosity to entropy ratio, η/S (otherwise known as 'Reynold's number') [53]. Measurements at RHIC suggested much rescattering and very low η/S [41], implying that the nature of the QGP produced at RHIC might be that of a strongly interacting 'perfect' fluid. Measurements at ALICE of flow in Pb-Pb collisions still show liquid-like behaviour [49].

1.3.6 QGP in Proton-Proton Collisions

Before heavy ion collisions, ALICE acquired data from the LHC proton-proton collisions [54]. This is an interesting area for the ALICE experiment because its physics should provide a comparison with heavy-ion collisions. As a QGP is not expected to occur in most proton-proton collisions, QGP signatures should be absent. Additionally, the ALICE detector is capable of very low transverse momentum (p_T) measurements with high resolution, and has excellent PID. In this way it can provide a unique look at proton-proton collisions at new energies.

A particularly interesting aspect of proton-proton collisions for ALICE to consider is the behaviour of high multiplicity events. To understand this, the Bjorken energy density is introduced [55]. Bjorken showed that the environment required to form a QGP can be represented in terms of energy density (a critical value of 1 - 3 GeV/fm^3 corresponding to a critical temperature of around 200 MeV/c). The energy density in a nucleus-nucleus collision can be related to the transverse energy;

$$\varepsilon = \frac{1}{\tau A}\frac{dE_t}{dy} \tag{1.13}$$

where A is the transverse area of the nuclei, which is approximately 60 fm^2 for central Pb-Pb collisions, and the proper time τ is taken from the point of thermal equilibrium. The transverse energy per unit of rapidity can be related to the mean transverse momentum and the multiplicity of the event:

$$\frac{dE_t}{dy} \simeq < p_T > \frac{dN}{dy} \tag{1.14}$$

The Bjorken "conjecture" [37] suggests from this that, in very high multiplicity proton-proton collision events, energy densities could be high enough for a QGP to form.

For more detail on this topic, see Section 4.1.

1.4 Diffraction

Diffraction in pp collisions is a process that affects the shape of the pseudorapidity density, as diffractive events distribute themselves differently kinematically to non-diffractive events. Although MC simulation of diffraction is available, at new energies the cross-sections for these processes, as well as their kinematics, are not yet well constrained. For this reason, an estimate of the fractions of diffractive events in minimum bias pp data at ALICE is needed, to estimate the uncertainty on the pseudorapidity density. This thesis contains a method using data and MC to estimate the fractions.

1.4.1 What is Diffraction?

In a pp interaction, events can be classified as either elastic or inelastic. Elastic events are ones in which the protons may scatter but remain intact, with no other particles produced in the interaction (see Figure 1.9a.). These events are missed by the ALICE detector. Inelastic collisions involve the break-up of at least one of the protons, causing fragmentation which leads to the generation of final state particles. In most inelastic collisions, the protons exchange coloured gluons and both are broken up, producing particles across rapidity space (see Figure 1.9b.) Some inelastic collisions can be "diffractive". The remnants of diffractive exchanges at high energy leave characteristic rapidity gaps [56].

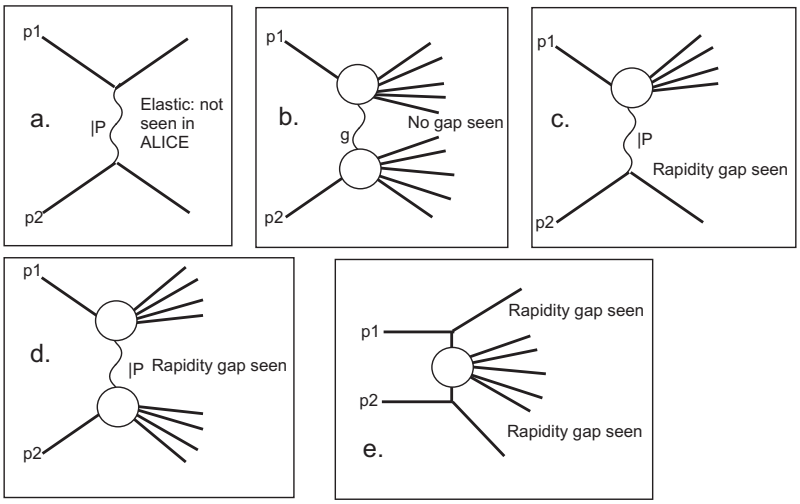

Figure 1.9: A representation of the different types of exchanges making up the total cross-section of events: (a) An elastic event; (b) A non-diffractive event; (c) A single-diffractive event; (d) A double-diffractive event; (e) A double Pomeron exchange.

Diffraction is an interaction between particles in which no internal quantum numbers are exchanged. This implies that a virtual particle with vacuum quantum numbers is responsible for the interaction (this would be necessary for an elastic exchange). The particle proposed to dominate this process at high energy, is known as the Pomeron [57].

Pomerons were originally proposed to prevent an unphysical rise with energy of the total cross-section in hadron-hadron interactions, which seemed to be a consequence of the exchange of virtual particles with finite integer spins. Regge theory [58], [59] describes the exchange of "Regge poles" - objects with complex angular momentum. Resonances that belong to the same "Regge Trajectory" of complex angular momentum have the same isospin, strangeness and baryon number, but different real values of J. The dominant p-p exchange required to control the total cross-section was proposed from Regge Theory to be one of a Regge trajectory which must have vacuum quantum numbers (i.e. capable of elastic exchange), and this is known as the Pomeranchuk Trajectory [57] after Isaak Pomeranchuk (the Pomeron was also named after him).

Single-diffractive (SD) processes are events where one of the protons is dissociated in the collision, and the other remains intact (Figure 1.9c.) This leaves a rapidity gap in the very forward region,

where the intact proton escapes down the beam pipe. In double diffraction (DD) both protons are dissociated (Figure 1.9d.) and the rapidity gap is in the central region. Another diffractive process is Double Pomeron Exchange (DPE), shown in Figure 1.9e., which leaves two rapidity gaps away from mid-rapidity.

1.4.2 Regge Theory and the Pomeron

The Pomeron was introduced to describe the p-p cross-section at asymptotic energies in accordance with the Froissart Bound [60].

When describing hadron-hadron scattering with low momentum transfer (soft scattering), early models consider the exchange of a single virtual particle with appropriate quantum numbers, much like the photon in proton-electron scattering. The amplitude of the scattering is then given by the sum of all possible exchange particles, and the particle with the largest spin J (and the appropriate quantum numbers) is considered to dominate. As the energy of the interaction increases, the total cross-section is expected to go as:

$$\sigma_{tot}\left(\sqrt{s}\right) \propto s^{J} \tag{1.15}$$

where J is the spin of the exchanged particle. This would mean that at high energy the total cross-sections would "blow up" as s increased (J is only observed in integer or half integer values). In this picture, at high enough energy, the total cross-sections would eventually go beyond the Froissart bound:

$$\sigma_{tot}\left(\sqrt{s}\right) \leq \frac{\pi}{m_{\pi}^{2}} log^{2}\left(\frac{s}{s_{0}}\right) \tag{1.16}$$

where s_0 has dimensions E^2.

Regge theory tackles this problem by describing J as a complex and continuous variable $\alpha(t)$ (where t is the Mandelstam variable, see Appendix A), following a "Regge Trajectory" in the complex plane that changes with energy. In this plane, physical observable states (resonances) lie where $\mathbb{R}(\alpha)$ is an integer or half-integer (observed values of J), and sit on a line satisfying:

$$\alpha(t) = \alpha_0 + \alpha' t \tag{1.17}$$

where, when $\alpha(t)$ is J, t is M_J, the mass of the exchange particle. The trajectories can then be projected in a "Chew-Frautschi" diagram (as shown in Figure 1.10), showing $\mathbb{R}(\alpha)$ as a function of invariant mass M^2. α_0 is the intercept and α' is the gradient of each trajectory, and resonances with the same isospin I, baryon number B and strangeness S lie on the same trajectories.

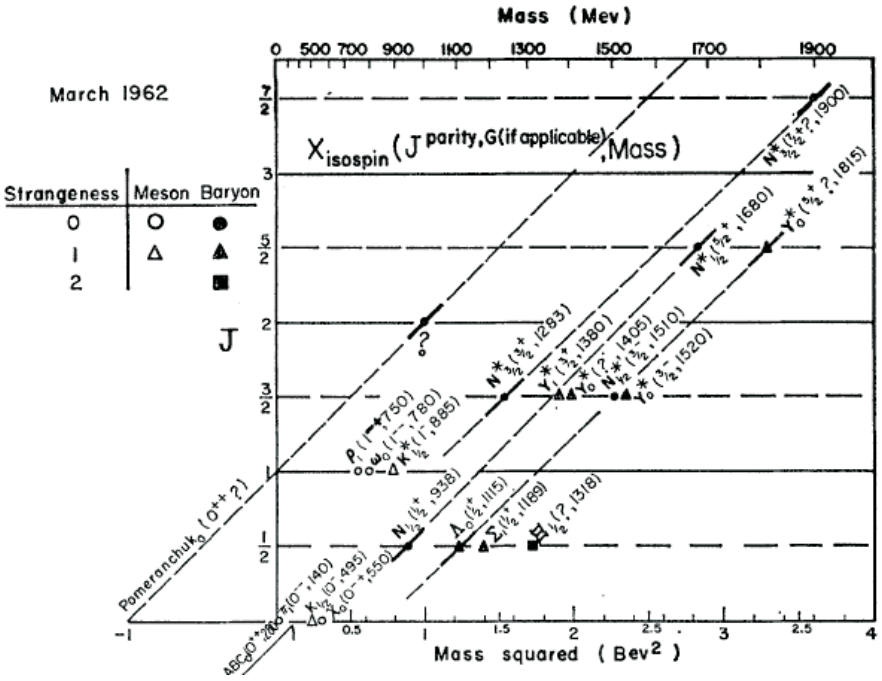

Figure 1.10: Chew-Frautschi plot showing Regge Trajectories in J and M^2 [61]. Resonances with the same I, B and S sit on the same line.

From the optical theorem, the total cross-section of hadron-hadron scattering can be related to the elastic scattering amplitude, at very high energy, in the following way;

$$\sigma_{tot} \propto s^{-1}\mathbb{I}m(A_{el})(t=0) \tag{1.18}$$

So the leading trajectory (the dominant exchange) should have vacuum quantum numbers. Exchange of the Regge trajectories contribute to the total cross-section as:

$$\sigma(\sqrt{s}) \propto s^{\alpha_0 - 1} \tag{1.19}$$

so in order to prevent violation of the Froissart bound, the dominant contribution to σ_{tot} at infinite energy would have its intercept at 1 or less. In fact, experimentally the total cross-section up to 1 TeV for pp scattering is measured to rise a little, favouring an intercept for the Pomeranchuk trajectory of α_0=1.08. In the Donnachie Landshoff approach [62], total cross-section has two components. At low energy, Reggeon exchange dominates, but this drops off with energy. At high energies the leading exchange particle is the Pomeron, with a dependence of around $s^{0.08}$. This is known as the Pomeranchuk trajectory. One candidate for the soft Pomeron is a glueball.

1.4.3 Diffractive Dissociation

According to the Mueller-Kancheli theorem [63], [64], the elastic cross-section at high energies can be related to inclusive proton production, pp→pX, where one proton is broken apart into a number of hadrons, X. This is shown in Figure 1.11. This means that the inclusive proton production can also be described by Pomeron exchange at high energy. One can see that summing all possible final states of pp→pX leads to the triple Reggeon and Pomeron exchange amplitudes.

In diffractive dissociation one or both of the protons are dissociated and fragment into a "diffractive mass" of particles, X, with collective mass M_X. In the case where one proton is dissociated, the process is referred to as single diffraction (SD). If both protons are dissociated, it is known as double diffraction (DD). At high energy it was observed that rapidity gaps were seen in the exchanges, as

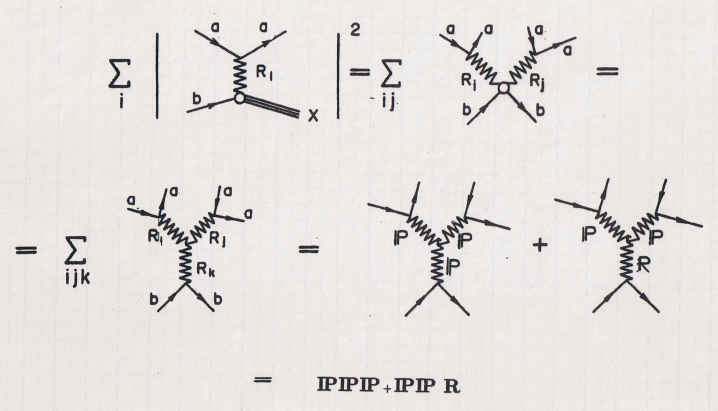

Figure 1.11: Relation of inclusive p production to the Triple Reggeon exchange, from the Mueller-Kancheli theorem. Taken from [65]

shown in Figure 1.9. The gaps can still be filled by the final state particles in the case of Reggeon exchanges, but at high energy, where diffraction is dominated by Pomeron exchange, the gaps are seen. Identifying the gaps experimentally depends on detector acceptance and granularity.

Where little momentum is exchanged in the interaction, this makes sense kinematically, as, for example in SD, the intact proton retains most of its initial velocity and in order to balance energy and momentum there must then be a substantial gap in rapidity between it and the next fastest particle. This is known as "soft" diffraction.

Because of the complicated partonic structure of protons, and in order to understand the rapidity gaps seen in high t exchanges, it is necessary to consider a QCD description of diffraction. For large t, but where $\alpha_s(t)<<1$, the Pomeron can be described by perturbative QCD, and can be thought of as a ladder-like gluon structure - essentially a pair of gluons that self-interact. An example is shown in Figure 1.12. This structure is colourless overall but has internal colour-exchanges. It was originally proposed by Bjorken [56], and explains the presence of rapidity gaps in high t Pomeron exchanges - in the case of a meson structure (as with Reggeon exchange), fragmentation of the exchange particle to quark-antiquark pairs can occur, extending across the rapidity space, filling the gap. The gluon ladder cannot be easily fragmented in the same way, and so the diffractive mass of hadrons is contained in rapidity space. This gives rise to a "hard" pomeron, and it can

contribute to the total cross-section more strongly with increased energy than the soft Pomeron.

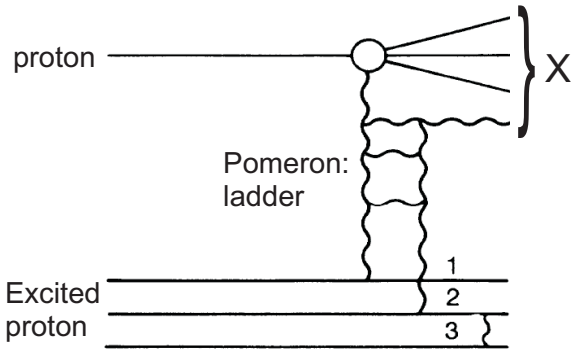

Figure 1.12: An example of a "ladder" exchange for Single Diffraction.

For very high energies such as at the LHC, hard interactions may become important. The Double Pomeron exchange (central diffraction) may have a larger cross-section. This is the hard interaction of two Pomerons, which break each other apart to leave rapidity gaps in the two forward directions, and two intact protons. This is also shown in Figure 1.9. There may also be processes such as pp→pX(jet).

1.4.4 The Diffractive Cross-Section

Some model predictions and current measurements at different energies are compared in Table 1.1. Predictions for diffractive cross sections vary considerably, particularly for 7 TeV and 14 TeV collisions, as different models take different approaches in describing inelastic diffraction. There is also some variation in experimental measurements, particularly in the total cross section.

Soft diffraction was earlier described using the Donnachie and Landshoff approach [81], based on Regge Theory. Newer predictions based also based on Gribov-Regge theory, taking into account Regge cuts, also exist [82], [83], [84]. An alternative description similar to that for light scattering from an opaque disk was developed by Good and Walker, [85]), where the potential for the process relates to the opacity and effective radius of the proton. GLM [86] and KMR [87] models use the Good and Walker approach to describe soft diffraction. The high diffractive mass part of the

Table 1.1: A summary of predicted pp($\overline{p}$) diffractive and non-diffractive cross-sections between 900 GeV and 14 TeV from various models, including the generators PHOJET and PYTHIA described in section 3.2, and the measurements of these to date by UA5, CDF, and the LHC.

Source	Energy	σ_{SD} (mb)	σ_{DD} (mb)	σ_{ND} (mb)	σ_{inel} (mb)	σ_{tot} (mb)
QGSM [66]	900 GeV	8.1	5.8	44.1	52.2	66.8
PYTHIA [67]	900 GeV	11.6	6.5	34.4	52.5	
PHOJET [68]	900 GeV	10.5	3.5	41.1	55.1	69.2
GLMM [69]	1 TeV	9.8	5.4	41.8	57	73.3
KMR [69]	1 TeV	10.9	7.2	39.5	57.6	74
LKMR [69]	1 TeV	13.8			57.4	73.7
PYTHIA [67]	7 TeV	13.7	9.2	48.5	71.5	
PHOJET [68]	7 TeV	10.7	3.9	61.6	77.3 (DPE 1.1)	
QGSM [66]	14 TeV	13	12	52	77	103
PYTHIA [67]	14 TeV	14.3	9.8	55.2	79.3	101.5
PHOJET [68]	14 TeV	11	4.1	68	84.5 (DPE 1.4)	119
GLMM [69]	14 TeV	11.8	6.1	53.3	71.2	92.1
KMR [69]	14 TeV	13.3	13.4	41.2	67.9	88
LKMR [69]	14 TeV	19			70.2	91.7
UA5 ($p\overline{p}$) [70], [71]	900 GeV	7.8 ± 0.5 ± 1.1	4.0 ± 2.5		50.3 ± 0.4 ± 1.0	65.3±0.7±1.5
CDF ($p\overline{p}$) [72], [73], [74]	1.8 TeV	9.46 ± 0.44	4.43 ± 1.18 ($\Delta\eta$ >3)		60.33 ± 1.4	80.03 ± 2.24
E710 ($p\overline{p}$) [75], [76]	1.8 TeV	9.4 ± 1.4			55.5 ± 2.2	72.1 ± 3.3
E811 ($p\overline{p}$) [77]	1.8 TeV					71.71 ± 2.02
ATLAS [78]	7 TeV				60.3±2.1	
ALICE [79], [80]	2.76 TeV				62.1 ± 1.6 ±4.3	
ALICE [79], [80]	7 TeV				72.7± 1.1±5.1	

diffractive cross section cannot be described by these soft approaches alone, and models usually describe hard diffraction in terms of the triple-Reggeon exchange diagram shown in Figure 1.11 [65]. However, they have different expectations for the high diffractive mass region. At high energies, this contribution becomes more important, but is not sufficiently constrained by the pre-LHC data, so the expected contributions start to diverge. For this reason, an experimental measurement of the diffractive cross sections at LHC energies is very important.

Chapter 2

The LHC and the ALICE Detector

2.1 The Large Hadron Collider (LHC)

The Large Hadron Collider (LHC) [88] is the largest and most powerful particle accelerator in the World. Crossing the Swiss-French border near Geneva, it is a 27 km circumference synchrotron, situated from 50 to 175 m underground. It is capable of accelerating protons from an acceleration energy of 450 GeV to 7 TeV and lead ions to 2.76 TeV per nucleon. This means protons can be collided at a $\sqrt{s}$ of 14 TeV, and lead ions at 5.5 TeV per nucleon pair - higher centre of mass energies than any other man-made collider has achieved - in order to push the limits of our understanding of the Universe. At the time of writing this thesis, it was running at half the nominal energy.

2.1.1 Performance

During nominal running protons in the LHC ring circulate in "bunches", with each bunch containing 1.15×10^{11} protons. At the nominal energy, they circulate the ring 11245 times per second. Each beam is filled with up to 2808 25ns bunches per orbit, out of the 3564 possible 25ns slots. The interaction probability for crossing bunches also depends on the beam intensity.

The machine luminosity is a measure of these effects on the number of interactions per second occurring at each collision point. The nominal luminosity of the LHC is L=10^{34}cm^{-2}s^{-1} for proton-proton collisions and L=10^{27}cm^{-2}s^{-1} for lead ion collisions. Luminosity can be written as a function of the beam parameters (assuming a Gaussian beam distribution), as shown below:

$$L = \frac{N_b^2 n_b f_{rev} \gamma_r}{4\pi\epsilon_n \beta^*} F \tag{2.1}$$

where N_b is the number of particles per bunch, n_b is the number of bunches in each beam, f_{rev} is the revolution frequency, γ_r is the relativistic factor, ϵ_n is the normalised transverse beam emittance (phase space volume), β^* is a beam-optics property that scales with the width of the beam, and F is the geometric luminosity reduction factor due to the crossing angle of the beams at the interaction point.

The number of events produced also depends on the cross-section for that event type, σ_{event}, which is a measure of the likelihood of the interaction:

$$N_{event} = L\sigma_{event} \tag{2.2}$$

Achieving high luminosity is therefore important for rare events. Two of the LHC's experiments, ATLAS and CMS, require high luminosity proton-proton collisions, at L = 10^{34}cm^{-2}s^{-1}, for this reason. The ALICE experiment, described in Section 2.2, is dedicated to measuring lead ion collisions. However, for proton-proton collisions, it requires a lower luminosity of L = 10^{30}cm^{-2}s^{-1}. LHCb will reach maximum luminosity of L=10^{32}cm^{-2}s^{-1}, while TOTEM will reach L=2×10^{29}cm^{-2}s^{-1}, with up to 156 bunches only. For LHCb and ALICE to have collisions with much lower than nominal luminosity, the beams are defocused or displaced accordingly.

2.1.2 Design

The LHC is contained within the Large Electron Positron (LEP) tunnel, which is separated into 8 segments, as seen in Figure 2.1 (taken from [89]). Each segment has a straight section at its

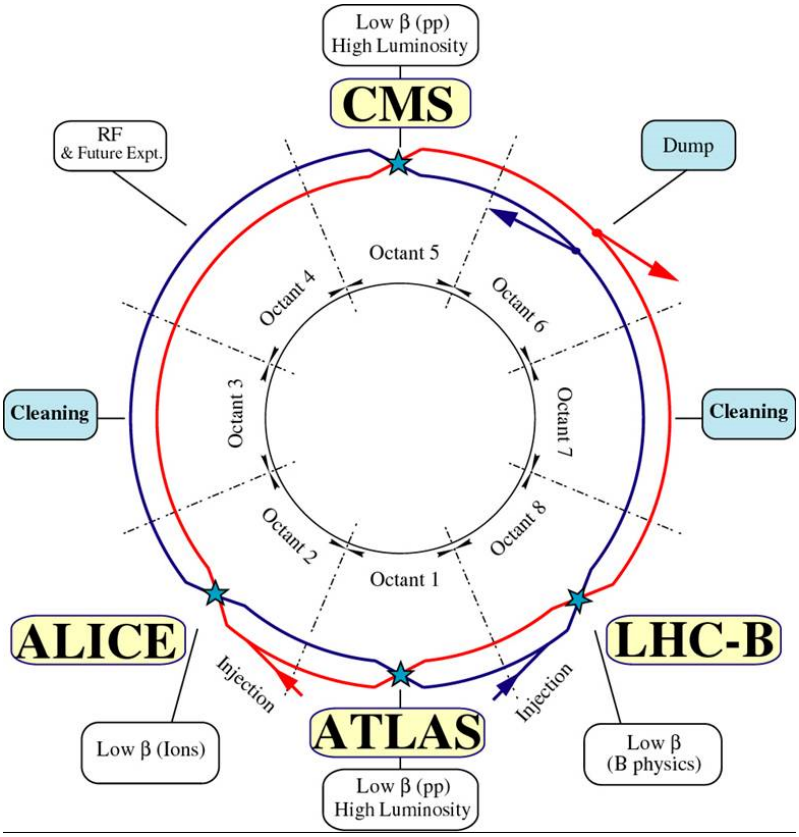

Figure 2.1: Schematic diagram of the LHC design.

centre (which can be used for colliding beams) called a point. The injection of particle beams into the beam pipes occurs before points 2 and 8. The beams are accelerated by a Radio Frequency (RF) system at point 4, consisting of 8 cavities per beam which produce a field of 5.5 MV/m. The system also compensates for synchrotron radiation energy loss (around 7 keV per turn at nominal energy) and keeps the particles in well-defined bunches. At point 6 a beam dumping "kicker magnet" system exists to eject the beam (within as little as three turns of the ring in case of loss of control of the beam). Points 3 and 7 have collimators for cleaning the beam, removing particles that have strayed from the bunch, either radially (getting close to the beam pipe) or along the beam (having been accelerated too much or too little). The beams are brought together at 4 intersection regions, points 1, 2, 5 and 8 on Figure 2.1, where the experiments are located. Joining each segment are the tunnel's arcs. The two parallel beam pipes of the accelerator are contained within "two-in-one" twin-bore magnets so that the two beams of protons (or nuclei) can still be sent in opposite directions around the ring within this spatial constraint, as shown in Figure 2.2 [90].

The main magnets, 1232 dipoles and 392 quadrupoles (see figure 2.3), are superconducting, kept at 1.9 K and powered with up to 11.7 kA current. They are used to steer (bend the trajectory) and focus the beams respectively.

The protons are taken from a hydrogen source and the beams are accelerated through part of CERN's Proton Linear accelerator, LINAC2, to 120 MeV, then the Proton Synchrotron Booster (PSB) to 1.4 GeV and the CERN Proton Synchrotron (CPS) to 26 GeV before being accelerated to 450 GeV at the Super Proton Synchrotron (SPS). Proton bunches are injected a few at a time from here into the LHC where the dipole field strength starts at 0.535 T, and the RF and magnetic fields are ramped up together to increase collision energy whilst controlling the beams. The dipole field reaches around 8.33 T for 7 TeV beams (14 TeV collision energy).

Lead ions are accelerated through CERN's ion machines, LINAC3 and LEIR, before being passed through the PS and SPS.

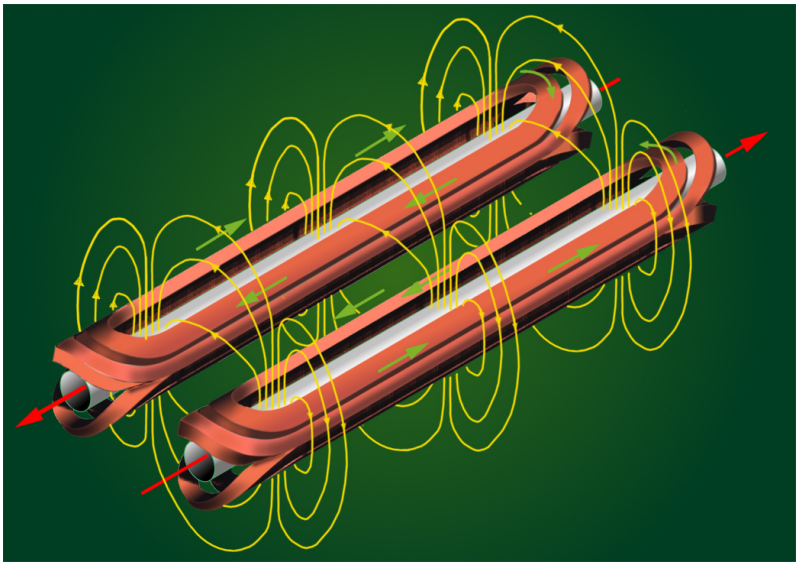

Figure 2.2: Magnetic field lines in the LHC twin-bore dipole magnet design. One can see from this arrangement that protons are driven in opposite directions in each pipe.

2.1.3 LHC 2008-2011

The last piece of the LHC beam pipe was installed in June 2008, and cooling of the magnets began, marking the start of its operational journey. Initial tests with 450 GeV proton beams from SPS were carried out in August 2008, where beams were injected and then dumped after a few octants. This gave ALICE the opportunity to begin calibrations early. On 10th September 2008, the first circulation of both proton beams was achieved, and over the next few days the magnets were ramped up slowly to increase beam energy.

On 19 September 2008, an electrical fault caused damage to the LHC and delayed progress by a year. On 23rd November 2009, LHC was up and running again and collided protons for the first time, and a few days later a World record proton beam energy of 1.18 TeV was achieved ($\sqrt{s}$=2.36 TeV). On 30th March 2010, the first collisions of 3.5 TeV beams ($\sqrt{s}$=7 TeV) began, and by November integrated luminosity (for the high luminosity experiments) was reaching 48 pb^{-1}.

On 6th November 2010, the LHC's first ion run began and successfully ran for one month. Since restarting in 2011, p-p events at 7 TeV have continued and nominal luminosity was achieved for

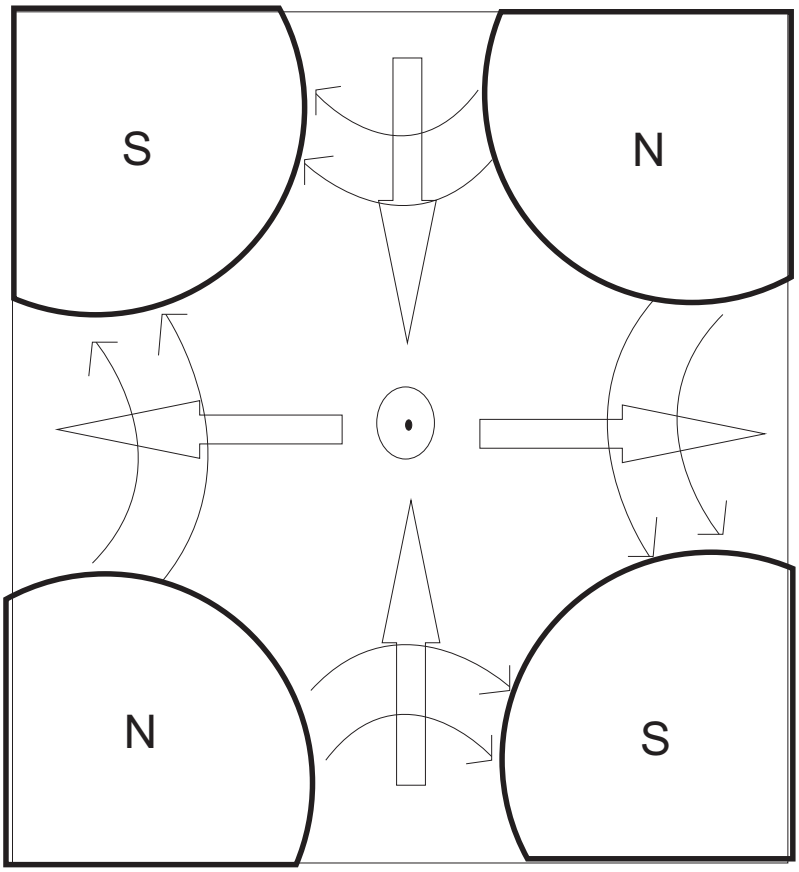

Figure 2.3: Magnetic field in quadrupole magnets, causing the perpendicular squeezing and broadening of a charged particle beam, oriented in such a way that overall focusing is achieved downstream.

ATLAS and CMS.

2.1.4 The LHC - Experiments

The LHC has four large experiments: ATLAS (A ToroidaL and Solenoidal detector) [91], CMS (a Compact Muon Solenoid detector) [92], ALICE (A Large Ion Collider Experiment) [93] and LHCb (The LHC's beauty experiment) [94], and two smaller experiments - LHCf (the LHC's forward experiment) [95]and TOTEM (for TOTal, Elastic and diffractive cross-section Measurements) [96]. ALICE is described in detail in Section 2.2.

2.2 The ALICE Detector

ALICE is primarily focused on heavy ion physics so its detectors are optimised for track reconstruction and particle identification in very high multiplicity events. It is capable of high precision measurement of primary and secondary vertices, measurement of a wide range of transverse momenta (200 MeV/$c < p_T <$ 100 GeV/c), and reconstruction of up to 8000 tracks per unit of rapidity in the central region.

The detector comprises a system of detectors covering the central region of pseudorapidity, $|\eta| <$ 0.9, some detectors covering forward regions, and a muon arm system on the C side, as labelled in Figure 2.4 [97]. The central detectors are enclosed within a large warm solenoidal magnet, with a field of up to 0.5 T. The pseudorapidity coverage of the detectors is shown in Figure 2.5 [98].

2.2.1 Inner Tracking System

The inner part of the central barrel, the Inner Tracking System (ITS) is shown in Figure 2.6 [99]. It is used to reconstruct the tracks of charged particles passing through it. Using this information, the primary vertex of each event can be localised and secondary vertices can be found for decayed

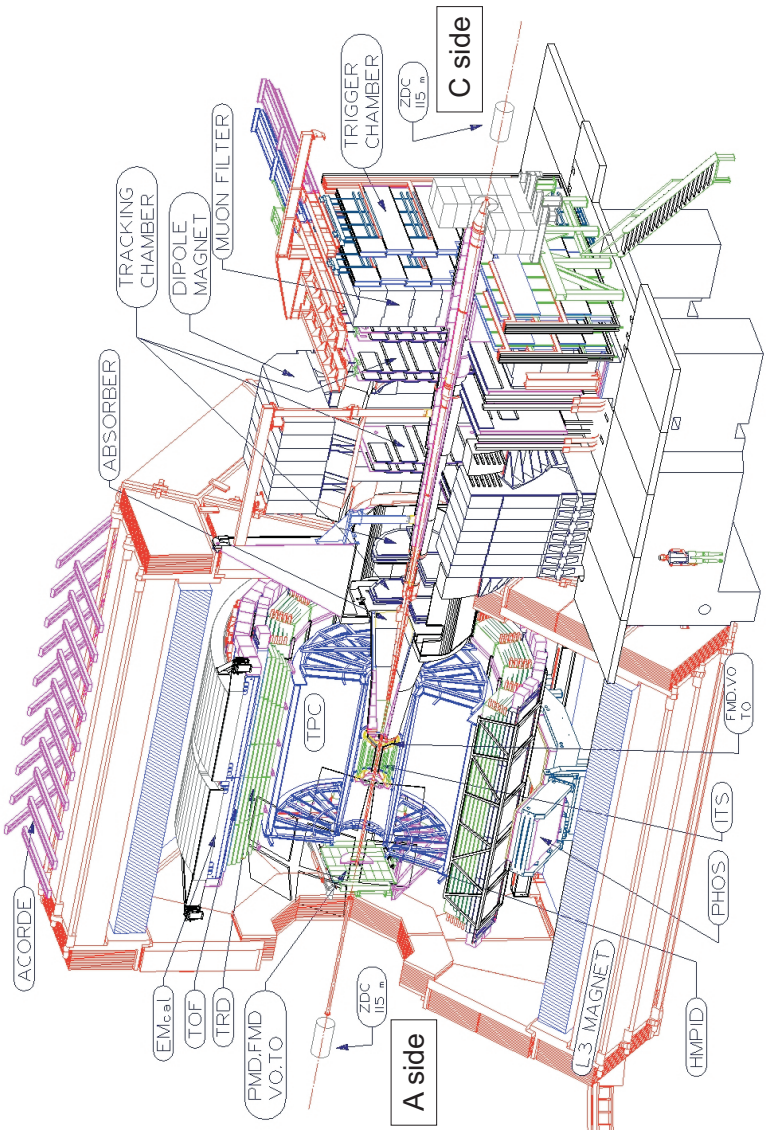

Figure 2.4: The detector layout for ALICE. The muon arm is shown on the C side, and along the beam axis in the opposite direction is known as the A side.

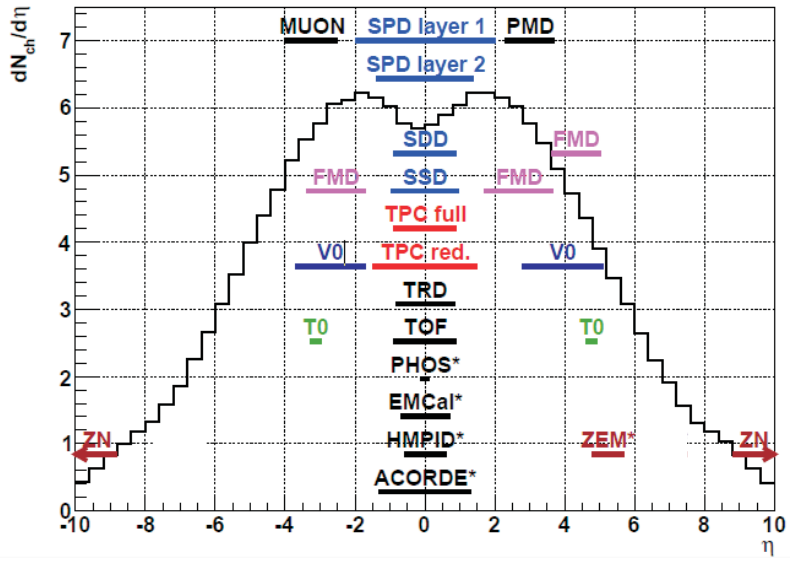

Figure 2.5: ALICE acceptance - the pseudorapidity coverage of each of the subdetectors overlayed with PYTHIA simulated pseudorapidity distribution.

particles. Charged particles can be tracked and identified with momentum above 200 MeV/c up to around 1 GeV/c.

It is made up of six cylindrical layers, the innermost two of which make up the trigger-enabled Silicon Pixel Detector (SPD) at an inner radius of 4 cm. These are followed by the Silicon Drift Detector (SDD), and finally the Silicon Strip Detector (SSD) reaching an outer radius of 43 cm.

The ITS is required to localise the primary vertex to better than 100 μm along the z axis, and to around 10μm in the xy plane, as well as to provide excellent spatial resolution so that good momentum resolution can be achieved for low momentum particles even with a high track density.

The SPD and SDD layers are best able to handle the high particle density of heavy ion collisions (up to 50 per cm^2 near the vertex point). The SSD layers are placed further from the collision, where particle densities reduce to below 1 per cm^2.

The SDD and SSD detectors also provide dE/dx information which can be used for PID (see section 2.2.2 for details on this method of PID).

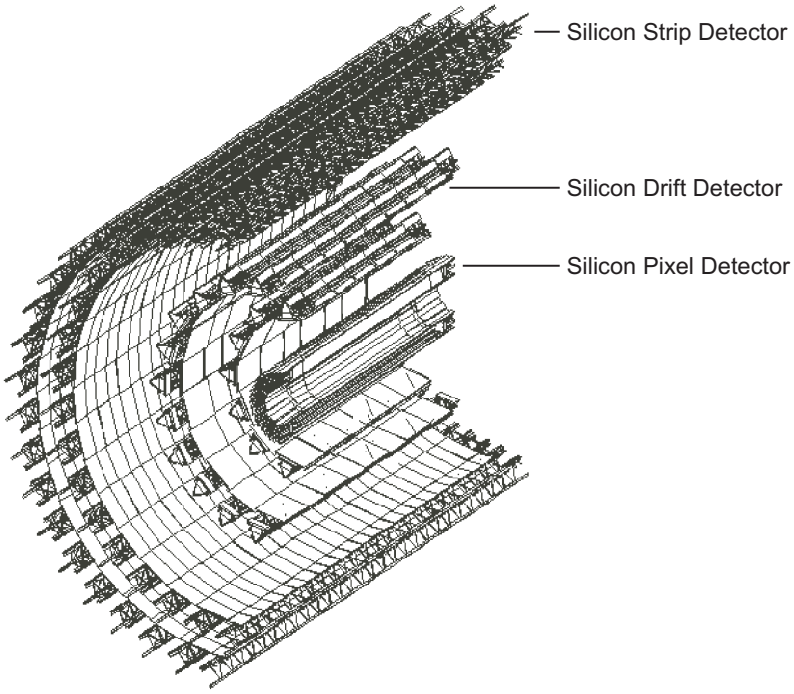

Figure 2.6: The ITS layers.

Silicon Pixel Detector (SPD)

The SPD has high granularity, and minimum material in the active volume (sensors of only a few hundred μm thick). The pixels can withstand high particle density and high radiation levels in excess of 10 Mrad (estimated exposure is 2.7 kGy over 10 years).

Each detector element is a "ladder" of 12.8 mm $\times$ 70.7 mm active area bump-bonded on to five binary readout chips. The active area is made up of 256$\times$160 silicon detector diodes or "cells", and each cell is 50 μm $\times$ 425 μm. The cells are this shape to maximise the area, avoiding damage from intense signals. They are orientated in such a way that they provide maximum spatial resolution: 12 μm (rϕ), 100 μm (z). Two ladders are connected to a pixel bus making a half-stave, and two half staves connect along z. The SPD is divided in rϕ into 10 sectors, each containing 2 inner and 4 outer "staves". There are 60 staves (240 ladders) or 1200 readout pixel chips in total. The total number of channels is 9.8 million. The inner layer covers a larger pseudorapidity region than the rest of the central system, of $|\eta| < 1.98$ rather than $|\eta| < 0.9$. This is to allow overlap with the

Forward Multiplicity Detector (FMD) (See section 2.2.9) so that a full multiplicity measurement can be made.

The SPD measures multiplicity and reconstructs primary vertices by identifying "tracklets", as shown in Figure 2.7. Achievable vertex resolution depends on the angle of incidence, but global resolution on the short pixel side was found to be 11.1±0.2 μm. This is useful not only for primary vertex finding but also to find the position of secondary vertices from weakly decaying particles.

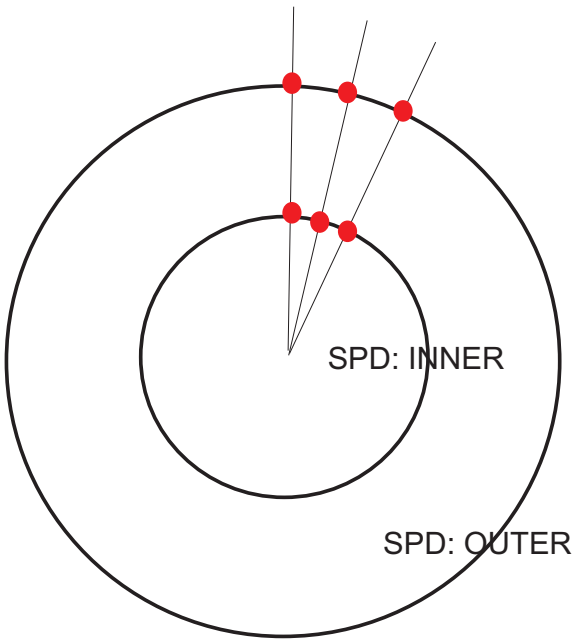

Figure 2.7: A multiplicity measurement in the SPD is made by reconstruction of "tracklets".

The SPD is one of ALICE's triggering detectors [100]. This means that it can send a signal to the Central Trigger Processor (CTP), to indicate that an interesting event has been seen. Different triggering detectors send these signals with a different latency after each collision, each providing a further level of selection (L0 after 1.2 μs, L1 after 6.5 μs or L2 after 106 μs. This is explained in more detail in Section 2.2.10), and the trigger signal SPD provides is L0. Each of the readout chips provides a "fast OR" signal (meaning that at least one pixel in the chip fired) and these signals are then sent to a Field-Programmable Gate Array (FPGA), which has a programmable boolean logic. This means that the SPD can be used to trigger events with a given number of hits in each layer (effectively, pixel-chip multiplicity). For "minimum-bias" selection, events with at least one

hit across the SPD (known as "Global Fast OR", or GFO) can be chosen, whereas interesting high multiplicity events can also be selected by setting a trigger threshold of N hits in each layer (see Section 4.1.3).

Silicon Drift Detector (SDD) and Silicon Strip Detector(SSD)

The SDD detectors are made of homogeneous 300 μm thick radiation-hard (several Mrad) "Neutron Transmutation Doped" silicon, each with a sensitive area of 70.17(rϕ)×75.26(z)mm^2. There are 14 ladders of 6 detectors each on the inner layer, and 22 ladders of 8 detectors each on the outer layer. Each one is divided into two drift regions by a High Voltage (HV) cathode strip. For 70% efficiency the SDD has an average double-track resolution of 700 μm.

There are 1698 modules in the SSD (748 inner layer, 950 outer layer), again structured in ladders (around 22 per ladder on the inner layer and 25 on the outer layer). Each SSD module has a sensor connected to 2 hybrids, one P and one N, each with 6 radiation-hard (several Mrad) front-end chips. The sensors are 300 μm thick with an active area of 73×40 mm^2. The spatial resolution of the SSD is 20 μm (rϕ) and 820 μm (z).

2.2.2 Time Projection Chamber

The Time Projection Chamber (TPC) [101], the largest in the World, is the main tracking detector of the central barrel, and is shown in Figure 2.8 [101]. It has an active volume of inner radius 85 cm, outer radius of 250 cm, and length of 500 cm. It comprises a drift gas system with multi-wire proportional chambers and is required to cope with high multiplicity events whilst giving good two-track separation, charged particle momentum measurements from 0.2 to 100 GeV/c, and particle identification using dE/dx information.

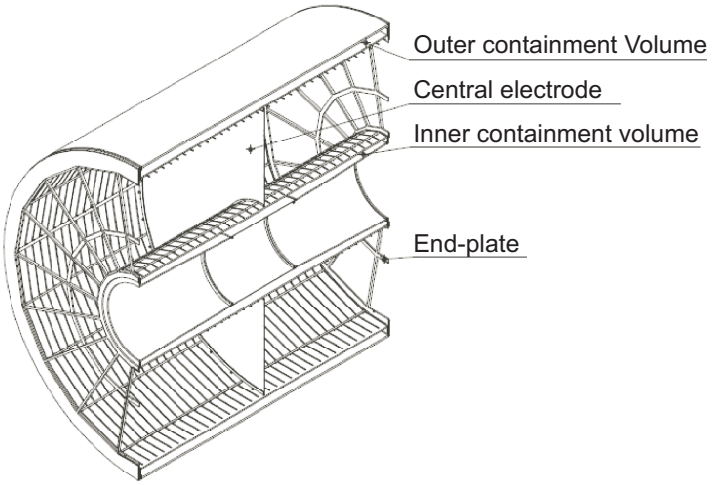

Figure 2.8: The TPC field cage.

Design

The TPC is separated into two large chambers filled with a mixture of Ne, CO_2 and N_2 gases in a 90:10:5 volume ratio [102], within the warm solenoid's 0.5T magnetic field, and a uniform electric field, along the z axis. The electric field is generated by a 100 kV electrode at the centre of the TPC, which is stretched to be only 22 μm thick to minimize the matter perpendicular to the magnetic field. An array of conductive strips around the inner and outer rings of the barrel are linked by potential dividers from the electrode to the end plates, each having 18 sectors of readout chambers filled with pads. Charged particles that pass through the gas cause ionised electrons to drift across the chamber and be detected in anode pads at the other side. The pad coordinates give the position in x and y of each track, and the time taken to cross the TPC gives the z co-ordinate from the drift, assuming a constant drift velocity. There are over 570,000 pads in total, and the drift time is long (currently 106 μs). It provides excellent position resolution (from 1100 μm at the inner radius to 800 μm at the outer radius (rϕ) and 1250 μm at the inner radius to 1100 μm at the outer radius (z)). Momentum resolution is 6.5% for 10 GeV/c tracks and 1 % for 1 GeV/c tracks [103].

The drift velocity for electrons in a gas can be described by the Langevin equation [104],

$$\overrightarrow{v_d} = \frac{e\tau}{m(1+(\omega\tau)^2)}(\overrightarrow{E} + (\omega\tau)\frac{\overrightarrow{E}\times\overrightarrow{B}}{\mid\overrightarrow{B}\mid} + (\omega\tau)^2\frac{(\overrightarrow{E}\cdot\overrightarrow{B})\overrightarrow{B}}{\mid\overrightarrow{B}\mid^2}). \tag{2.3}$$

where e and m are the charge and mass of the electrons, ω is the cyclotron frequency and τ is the mean drift time between collisions. To have a constant drift direction, the ideal is for $\overrightarrow{\mathbf{E}}$ and $\overrightarrow{\mathbf{B}}$ to be close to the same direction, so that the $\overrightarrow{\mathbf{E}}$ term dominates, and other parts tend to zero. This allows the electrons to drift out to the end plates in a straight line. ω and τ are optimised by a suitable choice of gas. Neon was chosen because it is light and has low density and a high radiation length, reducing multiple scattering. CO_2 is included as a quencher, and N_2 makes the gas more resistant to breaking down, which would cause sparks and could damage the readout pads. Unfortunately it is a "cold gas" (not heated), which means very small fluctuations in its temperature can affect the drift velocity. For this reason, heat shields and cooling are needed to keep the temperature stable to within 0.1 K.

The proportions of neon and CO_2 must be kept constant to within 0.1% because contamination from oxygen or water vapour can have a large effect on the gas' drift properties and degrade resolution.

Due to the requirement for a high signal to noise ratio from the electronics and gas, a high gain is needed, of up to 2×10^4. The electric field close to the pads is modified in a way which linearly amplifies the signal, known as a "gas gain" or "avalanche", so that the measured charge still represents the initial dE/dx.

Because there are also positive ions released in ionisation, which are slow moving and travel towards the central electrode, there is a danger of "space charge build up". During the time for the electrons in a given event to reach the readout pads, around 90 μs, positive ions are produced, and could distort the electric field. This is controlled by using gating wires, which counteract the electric field at the entrance to the amplification region, reducing drift by a factor of 10^5. This is only

released when the trigger detector sends an L1 trigger pulse to the TPC, indicating it should be read out. In this way, the charge can dissipate between events. However, if the overall event rate is too high then the charge may still build up. For this reason, the TPC readout rate is limited to around 1 kHz for p-p collisions.

Particle Identification

The momentum of charged particles in the TPC is found from the curvature of their tracks in the magnetic field. Specifically, the Sagitta (deviation from a straight line, as shown in figure 2.9) is:

$$s = \frac{L^2}{8r} \tag{2.4}$$

where L is the length of the straight line between two points on the track, and r is the radius of curvature. Because this radius is determined by the magnetic field B, the electric charge of the particle and its transverse momentum p_T, it can be shown that:

$$p_T = \frac{L^2 QB}{8s} \tag{2.5}$$

Particles can be identified using dE/dx information. The Bethe Bloch formula describes the energy a particle loses as it travels through a material;

$$-\frac{dE}{dx} \propto \left(\frac{Z^2}{\beta^2} ln\gamma\right) \tag{2.6}$$

where Z is the atomic (proton) number of the atoms in the material, β is $\frac{v}{c}$ and γ is $(1-\beta^2)^{-1/2}$.

Clearly it is dependent on the velocity at which the particle is traversing the medium. For a given momentum, each particle mass has a different speed. The measured dE/dx can be plotted against the measured momentum of each particle, separating particles of different masses for a given momentum range, as shown in Figure 2.10 [105].

The TPC can resolve dE/dx to within 5% for isolated tracks, and within 6.8% in the case of dN/dy of 8000 (saturation). It has a track efficiency of better than 90%.

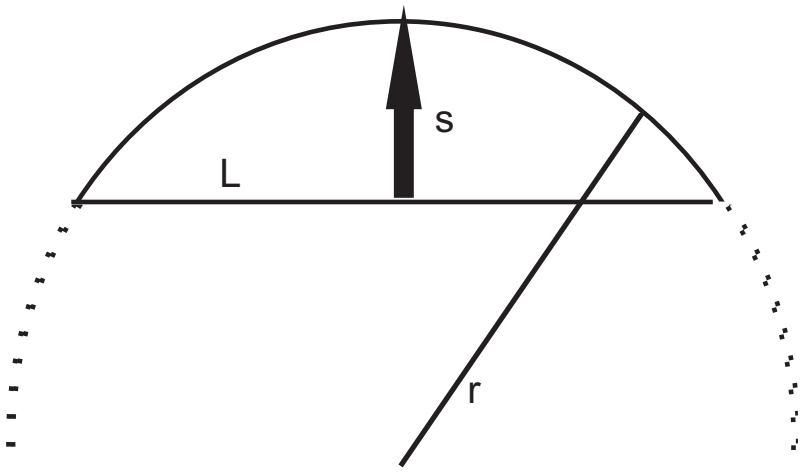

Figure 2.9: The Sagitta of a curve.

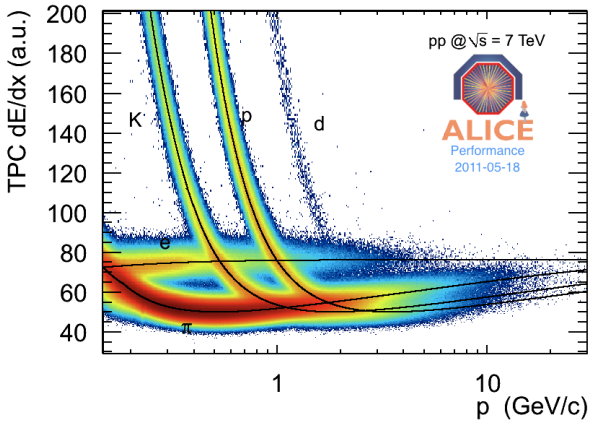

Figure 2.10: dE/dx of 7 TeV pp collisions as a function of momentum, as measured in the TPC.

2.2.3 Transition Radiation Detector (TRD)

The Transition Radiation Detector (TRD), just outside the TPC, is intended for higher momentum ($p_T > 1$ GeV/c) electron identification in the central region, where electrons cannot be identified using their energy loss in the TPC. The TRD uses transition radiation, given when an electron passes through a boundary between two materials of different refractive indices, as well as energy loss measured in a drift chamber with a gas containing heavy nuclei (xenon). The xenon atoms readily absorb transition radiation photons, releasing inner shell electrons (photo-electric effect). These electrons then drift in the usual way and are detected as a single pulse at the end of the drift time associated with the track. The TRD electronics dissipate a lot of power, so in order to keep temperature under control, it remains "asleep" until it receives a pre-trigger (before L0) created using very early signals from T0, V0 or TOF (at as early as 350 ns after the collision). Even with this procedure, it dissipates 76 kW for Pb-Pb collisions, and 105 kW for p-p collisions, where, even for ALICE, optimal luminosity is much higher than in Pb-Pb collisions, and interaction rates reach into the hundreds of kHz [106].

2.2.4 Time Of Flight (TOF)

The Time Of Flight (TOF) detector uses Multi-gap Resistive Plate Chambers (MRPCs) to identify charged particles of momentum range of up to 2.5 GeV/c for pions and kaons and 4 GeV/c for protons (those which cannot be identified using TPC dE/dx measurements). It measures the time taken for the particle to traverse the detector, t=L/β, where L is the path length, and uses this with the momentum information from the TPC to separate pions and kaons, or kaons and protons.

The MRPCs are 10 stacks of resistive glass plates, separated very evenly with nylon wire. A high voltage (around 12.5 kV [107]) is put across them, and the coatings of the plates act as electrodes. The gaps are filled with an ionizing gas, and the high electric field amplifies the signal (as in the TPC). As a track enters a gap, a pulse is seen. The resistive plates in each gap stop the avalanche

developing into the next gap, but allow the signal from the track to go through. The gaps are very small, so there is essentially no drift time. The delay in readout is timed so that each pulse is seen almost instantaneously. Multiple gaps therefore allow the average time to be measured, accounting for fluctuations caused by a varying pulse size. The result is that a precision of 50 ps is achieved.

The TOF stores the previous 1.6 μs of activity, and if an L0 is received, all of the information is available and recorded. This is done so that the pulse corresponding to a particular bunch crossing can be evaluated. The start time of the collision is obtained offline, by calibrating its shift with respect to the BC clock with the corresponding shift in the T0. Using the total time measurement together with the momentum information from the TPC, the particle may be identified by its mass. This allows particles with similar momenta to be distinguished from each other. Kaon identification is particularly useful for the reconstruction of hadronically decaying ϕ mesons.

The TOF is also required to provide a pre-trigger (before L0) "wake-up" signal to the TRD, which it does in around 200 ns [108].

2.2.5 V0

V0 detectors, V0A and V0C, are arrays of scintillator counters which cover the pseudorapidity regions $2.8 < \eta < 5.1$ and $-3.7 < \eta < -1.7$ respectively. Their asymmetric positions are due to spatial restrictions from the muon absorber on the C side. They are needed to provide minimum-bias triggers, and they can serve as indicators of the centrality of a collision by recording event multiplicity.

The V0 detectors each are made up of 32 counters (4 rings and 8 sectors) made of organic scintillator. The signals are extracted via wavelength-shifting (WLS) fibres. The designs for V0A and V0C differ slightly, as shown in Figure 2.11. V0A's fibres are embedded across both faces of each counter, separated by 1 mm. The V0C fibres, alternatively, are glued along the radial edges. Optical fibres then carry the signals to photomultipliers.

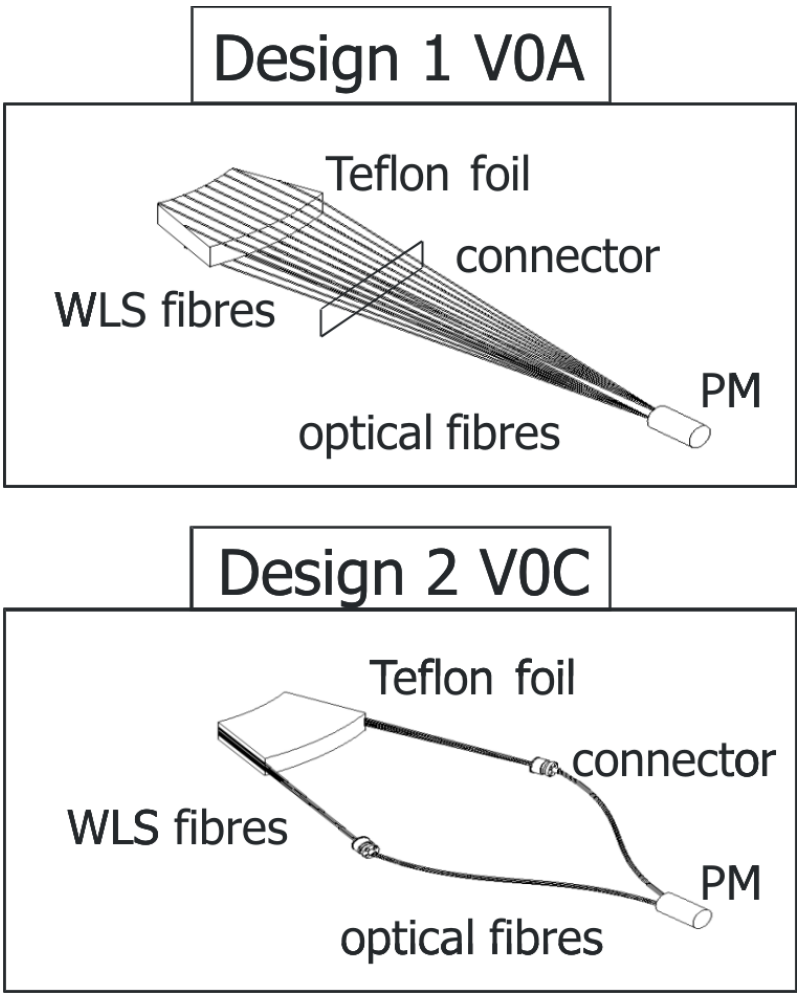

Figure 2.11: Design of V0A and V0C, showing the different light collection methods.

The V0 detectors are triggering detectors, and can send trigger signals in 16 combinations. In this way, it is possible to have V0**OR**, V0**AND**, and combinations of their rings, as inputs, as well as V0A and V0C. They are important for minimum-bias (MB) triggers, as well as others such as multiplicity, central and semi-central triggers.

The V0s can use timing information to identify beam-gas events occurring outside of their timing window, and send a signal to the CTP for use as a veto signal. This is shown in Figure 2.12. These events occur because the beam pipe does not have a perfect vacuum, so sometimes nucleons in the beam can interact with those in the residual gas. The beam-gas removal works by using timing measurements and comparing them to the BC clock. For example, in the case where there is a beam-gas interaction upstream of the V0C, the hits on the C side will have arrived at a negative time with respect to the expected collision time, and the hits on the A side will have arrived at a positive time. Because the V0A and V0C are positioned asymmetrically with respect to the collision point, in a normal beam-beam collision there is a known difference in time for hits in either direction to reach the respective V0s. Any hits with a negative time with respect to one bunch crossing are therefore not associated with the current event, nor attached mistakenly to the previous bunch crossing, because the time difference would not be correct in these cases.

2.2.6 T0

The T0 detectors are two arrays of 12 quartz Cherenkov counters with ranges $4.61 < \eta < 4.92$ (T0A) and $-3.28 < \eta < -2.97$ (T0C). T0A is 375 cm from the interaction point, whereas T0C is only 72.7 cm from it due to space constraints. The T0 detectors are placed as close to the beam pipe as possible to maximise efficiency. They use fast electronics of the same type as the TOF detector, in order to generate a precise "start time" (T0) for the collision, with 50 ps precision. This is then used offline in conjunction with the TOF detector for time-of-flight measurements. T0 measures the start time independently of the vertex position, by timing bunches leaving the detector. The timing signal can then be used to determine quickly the vertex position of the event

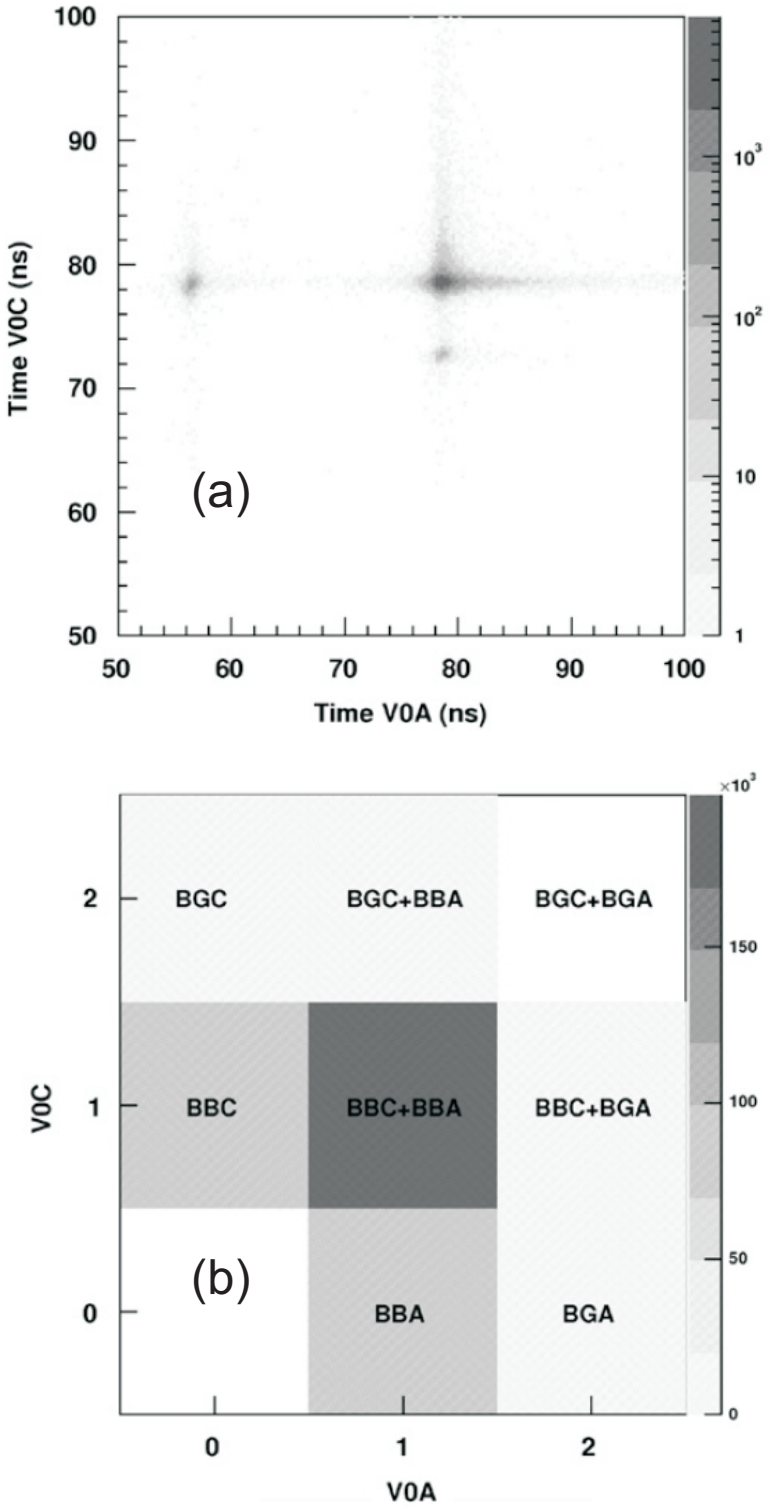

Figure 2.12: (a) Correlation between V0A and V0C particle arrival times. (b) Yield of events satisfying each trigger selection, where BB indicates the timing window for valid beam-beam events, and BG indicates the interaction falls outside that timing window. Both figures from [109].

to ± 1.5 cm precision, so that T0 can provide a L0 trigger input signal when the position is within allowed limits. This can exclude some of the beam gas events that V0 are unable to identify. It can also provide minimum bias or multiplicity triggers if needed. As mentioned earlier, the T0 can also quickly (∼ 350 ns) generate a signal that contributes to the "wake up" of the TRD.

2.2.7 Zero Degree Calorimeter (ZDC)

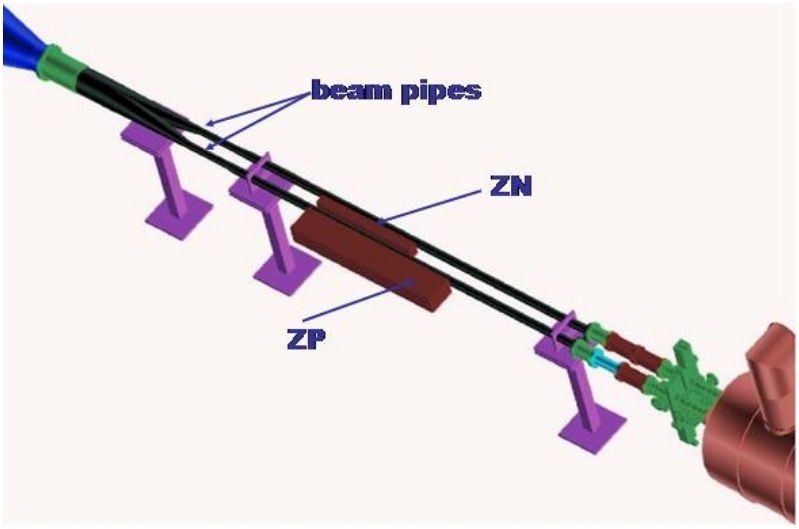

Figure 2.13: The ZDC proton and neutron detectors, ZP and ZN.

The Zero Degree Calorimeter (ZDC) consists of two sets of hadronic calorimeters, ZP and ZN, placed 116 m from the interaction point on both sides of the detector, and electromagnetic part (ZEM) placed 7 m from the interaction point only on the A side. The hadronic part uses a neutron calorimeter ZN, placed at 0 degrees between the beam pipes, and a proton calorimeter ZP which is positioned as shown in Figure 2.13 [110] where spectator protons are deflected by LHC's dipole magnets. The role of ZP and ZN is to measure the "spectator" nucleons in a heavy ion collision (the nucleons that were disturbed but were not broken up by the interaction). The more peripheral a collision, the more energy is deposited in these forward detectors by the spectators.

The ZP is a sampling calorimeter using a brass absorber. It requires a large area to cover the wide spatial distribution of the protons. The ZN is very restricted spatially because of its position

between the two beam pipes, and can be no larger than 7 cm, so a very dense tungsten alloy is used to maximize shower containment.

The ZEM is positioned above and below the beam pipe and helps to distinguish between head-on (central) collisions and very peripheral (glancing) events where few nucleons were disturbed in the collision, which look similar in ZP and ZN detectors. The ZEM measures energy in the medium-forward region event by event to distinguish between head-on and very peripheral events.

2.2.8 Muon Arm

The Muon Arm consists of the Muon Spectrometer and the Muon Trigger, preceded by absorbers and filters to reduce background from particles which are not muons. This detector combines the World's largest warm dipole magnet, which has a field up to 0.7 T and high bending power (magnetic field density) of 3 Tm, with high granularity tracking chambers. It is designed to detect high p_T muons coming from, for example, J/ψ decay. Absorber material is positioned in the forward region, 90 cm from the vertex, and is used to stop the high levels of background produced in the collision reaching the Muon Spectrometer. After the muon chambers there is a muon filter - an iron wall of thickness 1.2 m ($\sim$ 7.2 λ_{int}) intended to absorb any high energy particles that are not muons. High p_T dimuons from heavy flavour decays occur very infrequently, so a trigger is required to select those events in which they are produced. This is provided by two planes of muon trigger chambers, using Resistive Plate Chamber (RPC) technology placed beyond the muon filter where very few hadrons reach.

2.2.9 Other Subdetectors

Three Forward Multiplicity Detector (FMD) silicon sensor rings cover the regions $1.7 < \eta < 5.0$ (FMD1 and FMD2) and $-3.4 < \eta < -1.7$ (FMD3), overlapping with the ITS and V0s, to allow for cross-checks and uniform vertex distribution coverage. FMD2 and FMD3 are located either side

of the ITS and FMD1 is placed further out from the interaction point. Their aim is to provide charged particle multiplicity information in these regions.

PHOS (PHOton Spectrometer) is an electromagnetic spectrometer which uses lead tungstate crystals as homogeneous scintillator material. PHOS measures high p_T neutral pions and photon jet correlations for jet quenching studies, and low p_T direct photons for studies of the thermal and dynamical phase properties in the collision.

The High Momentum Particle IDentification (HMPID) detector is designed to improve identification of hadrons at momentum greater than 1 GeV/c, where dE/dx and time-of-flight measurements are less effective. It can separate pions from kaons of up to 3 GeV/c, or kaons from protons of up to 5 GeV/c, and also identify light nuclei at high p_T in the central region. It works using proximity-focussing, Ring Imaging CHerenkov (RICH) detectors, where Cherenkov photons released by fast charged particles are detected by photon counters.

A COsmic Ray DEtector, (ACORDE), an array of plastic scintillators placed above the L3 magnet, is used for triggering cosmic ray events for calibration and alignment.

The Photon Multiplicity Detector (PMD) is made up of arrays of gas filled proportional chambers in a honeycomb shape, which measure the photon multiplicity and spatial distribution in η and ϕ for the range $2.3 < \eta < 3.7$.

2.2.10 ALICE Trigger System: Central Trigger Processor (CTP)

Triggering detectors send signals to the ALICE Central Trigger Processor (CTP) [93], which can use this information to optimise event selections and send triggering information to detectors informing them to read out. It controls the rate of interactions to fit with detector capabilities, whilst still providing minimum-bias initial triggers. All detectors send "BUSY" signals to the CTP, indicating when they are not ready to take data. The CTP can then veto any possible trigger signals from being sent to them in this case.

Some tracking detectors require a very fast response from the CTP. This is done by providing three levels of trigger signal. An initial (L0) signal arrives at the detectors in 1.2 μs (most of this time is caused by travel through the cable), and after 6.5 μs, when more information is available, a second signal, L1, arrives confirming or rejecting the first. The slow drift time of the TPC means that TPC pile-up can occur in Pb-Pb collisions (where more than one interaction has occurred during the drift time of the TPC, either side of the triggered one - not the same as pile-up in a single bunch crossing). This cannot be reconstructed, so the CTP must identify these events and reject them. This is done using "past-future protection" (see below). Provided the event is accepted, the final level (L2) signal is sent after 106 μs.

The CTP is made up of 7 VME boards, and through each of these the signals are sent to the detectors using the Local Trigger Unit (LTU). The system allows for 24 L0 inputs, 24 L1 inputs, 12 L2 inputs and 50 trigger classes (see below). Inputs can be negated, asserted or set to irrelevant, and are linked in AND's. Negation is restricted to 6 of the 50 classes. Four L0 inputs are sent through a look-up table and are able to have any combination of logic applied to them. This allows for the use of, for example, the OR of GFO and V0, which is required for the minimum bias trigger. In addition to this, a programmable switch is available to change remotely which inputs are applied to the look up table.

Detectors do not need to read out together. A group of detectors which are set up to do so is said to form a cluster. Up to 6 clusters may be defined at one time, and a given detector can be in more than one cluster at the same time. Classes are defined based on certain inputs, and the clusters of detectors being triggered by those inputs. Each gives a different event rate, and the class can be set to downscale the overall rate.

The DAQ's temporary storage (see below) can become saturated with data from high rate triggers, or "common events", leaving it unable to read for several seconds. This causes the problem that rare events which occur during this time will be missed. To resolve this, after a certain upper limit on the temporary storage, the common event classes are disabled, allowing any rare events

to continue to be recorded until the temporary storage has reduced below a lower limit.

Past-future protection works, in the heavy-ion case, by applying limits on how many events can occur within the 106 μs before a final decision is made. This is done using counters which are incremented each time an interaction occurs, and decreased at a fixed (programmable) time later. The count at any given time fixes the protection status according to the requirements for the given run. The following is an example of how this can work:

If the initial event is semi-central, no more semi-central events are accepted, but up to 5 peripheral events are allowed. In the case where the triggered event is a peripheral one, up to 5 more peripheral events are allowed, but no semi-central ones. For proton-proton collisions, a different mode can be selected. For example, because distinguishing between central and peripheral events is not necessary, the system instead allows up to 10 interactions within the 106 μs, and applies the additional condition that only two interactions are allowed per 10 μs.

In addition to the triggering detector signals, the TRD sends an input signal to inform the CTP that it has received a pre-trigger and is awake. This is required before the CTP can send an L0 signal to any cluster which includes the TRD.

Information from each accepted event is recorded - it is tagged with the orbit and bunch-crossing number, and a list of which detectors read out. This information is sent to the DAQ before being sent to the detectors. The DAQ needs to be aware of which detectors are reading out in an event.

The CTP also has the ability to record signals for 32 ms using "Snapshot" memory. This can be viewed in the software to confirm information provided by counters.

2.2.11 ALICE Trigger System: Data AcQuisition (DAQ)

The Data Acquisition (DAQ) system takes the information from the CTP to determine which detectors will read out a triggered event [93]. These detectors then send their data through their

front-end electronics via Detector Data Links (DDLs) to buffering space in the DAQ Local Data Concentrators (LDCs). If a certain level is exceeded, the DAQ informs the CTP to disable "common event" classes. If, despite this, the occupancy of the LDCs continues to rise, at a certain level a general DAQ "BUSY" will be sent to the CTP, preventing any further triggers. This is known as "back-pressure".

Because the information relating to one triggered event comes from different places, the DAQ must combine the information in Global Data Collectors (GDCs) to form full events. In some cases, a further filtering of the selected events is appropriate. For this reason a copy of the raw data of these events from all detectors is sent to the High Level Trigger (HLT). The data from events can then be stored on the GRID and made available for use in the AliEn software [111].

2.2.12 ALICE Trigger System: High Level Trigger (HLT)

The High-Level Trigger (HLT) is sent full data readout from events and must make decisions to accept or reject them by quickly analysing this information online [93]. It is possible to select only interesting information from particular events by reading out from only the appropriate detectors. In addition to this, all accepted events can be compressed, to reduce the storage space they use.

2.3 TooBUSY Diagnostic Tool

This section describes a software tool developed by the author using firmware [112] that probes detector busy signals. At the start of the study, the firmware was untested. First the firmware will be described, then a short description of tests of the firmware that the author carried out. Finally, the actual diagnostic tool and its development is described, and examples of the tool in use during data-taking are shown.

When detectors are unable to read out they send a BUSY signal to the CTP, and this information

can be used to optimise the trigger configurations. Firmware for monitoring these signals was already available. The TooBUSY diagnostic tool was a software tool designed by the author, making use of this firmware, to provide information about the busy time distribution of a given detector, and the correlation of BUSY between detectors.

2.3.1 TooBUSY: The Firmware

The logic of the firmware available for use is shown in Figure 2.14 [112]. The busy signals can be monitored through various counters and timers, which provide information such as the average or largest busy of a detector, or the last detector to release a busy signal. Note in particular the probe, "BUSYlong". To use this probe, a minimum time-length of busy is set, and the probe will count how many times a selected detector or cluster exceeds this limit with a busy signal, within a set time interval.

Measuring probes used in the TooBUSY firmware

BUSY timer Counts every 25 ns while busy signal is being sent - measures busy time

BUSYmax accumulator Stores busy time if larger than last stored busy time - measures maximum busy time

BUSYmini accumulator Stores busy time if lower than last stored BUSY time - measures minimum busy time

BUSYlong generator Provides 25 ns "BUSYlong" pulse each time busy time exceeds a set busy time threshold - measures busy distribution

Access and control commands used in the TooBUSY firmware

BUSYmax_read_data Accesses busy time in BUSYmax accumulator at the end of each busy signal

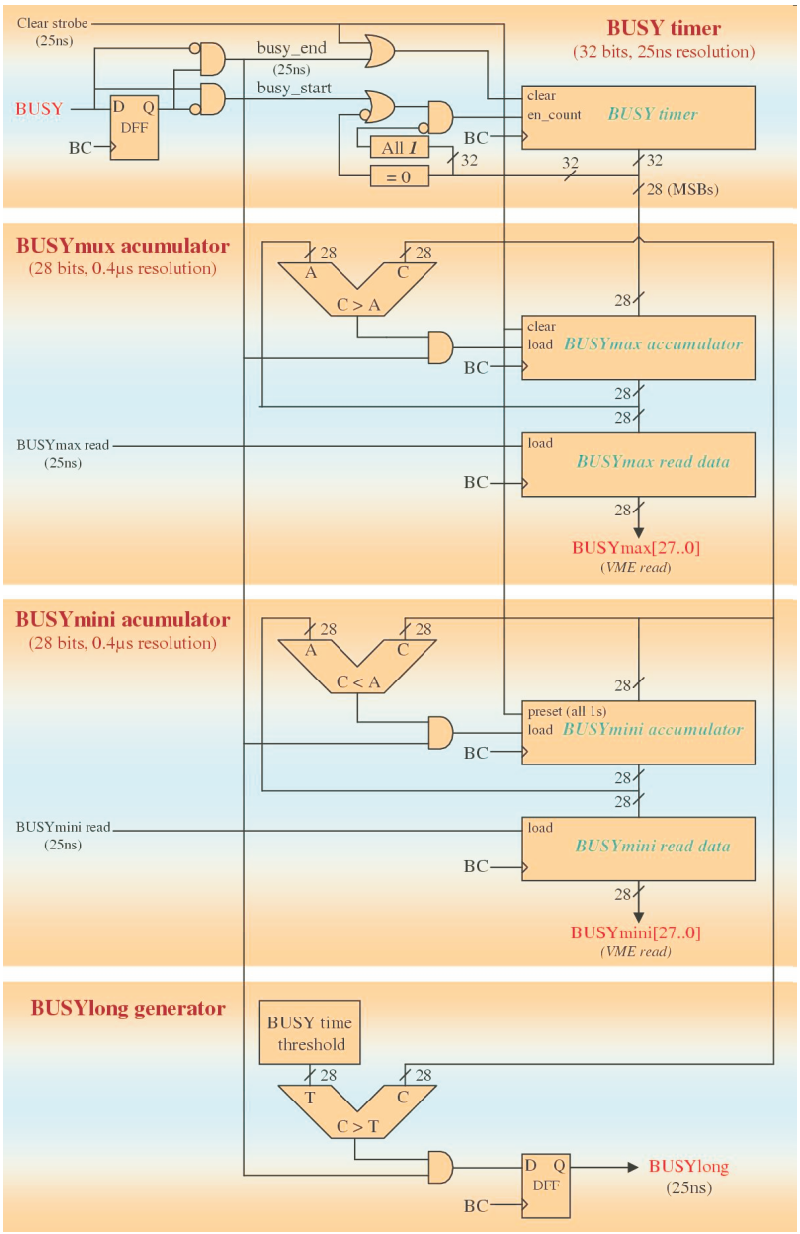

Figure 2.14: A logic diagram of the MINIMAX tools.

BUSYmini_read_data Accesses busy time in BUSYmini accumulator at the end of each busy signal

BUSYMAX_DATA VME command to read busy time in BUSYmax_read_data

BUSYMIN_DATA VME command to read busy time in BUSYmini_read_data

MINIMAX_LIMIT VME command to set the busy time threshold for the BUSYlong generator

MINIMAX_Select VME command to set the detector to be measured

INT_DISB_CTP_BUSY VME command to artificially generate a busy signal when no detector is available

BUSYlong Accesses the number of 25 ns 'counts' from the BUSYlong generator

This firmware works by first measuring the time of a detector's busy signal (busy time), using a "BUSY timer". "BUSYmax_read_data" and "BUSYmini_read_data" store the longest and shortest busy time, which can be read out at any time by using the VME commands "BUSYMAX_DATA" and "BUSYMIN_DATA". The busy time is also sent to the "BUSYlong generator", which forms the basis of the TooBUSY tool. It releases a 25ns pulse if the value is greater than a set limit, which can be set using "MINIMAX_LIMIT". This pulse is counted, giving the number of times a detector exceeds the given limit. By changing the limit progressively, it is possible to scan the busy spectrum, each time measuring the number of events in a sample within a fixed time period for which the detector's busy signal exceeds that limit.

2.3.2 TooBUSY: Testing

Initially, software was set up in order to make tests of the firmware using the CTP test installation at Birmingham. In addition to making each of the items selectable in the software, a testing function, demo(), was written. When run, it issues a set of instructions in order to generate a test busy and measure it, printing the results to the screen. First, the detector to be read (in this case

CTP) was set, using "MINIMAX_Select". For program development purposes, an artificial busy could be generated in the CTP, by setting the signal to 1 directly using "INT_DISB_CTP_BUSY", and returning it to 0 after a desired number of microseconds using the function mysleep(). The tools BUSYMAX_DATA and BUSYMIN_DATA, which output the length of the maximum and minimum busies, and the BUSYlong generator, which counts busy signals above MINIMAX_LIMIT, could then be tested. A sweep of busy times of varying length was performed in demo() and the results were printed to the screen. A 'snapshot' of the busy signal was measured using the snapshot memory on the busy board and each measured busy time was also printed to screen. Figure 2.15 shows an example of the firmware functioning normally, with the busy signals in the snapshot matching those measured by the firmware.

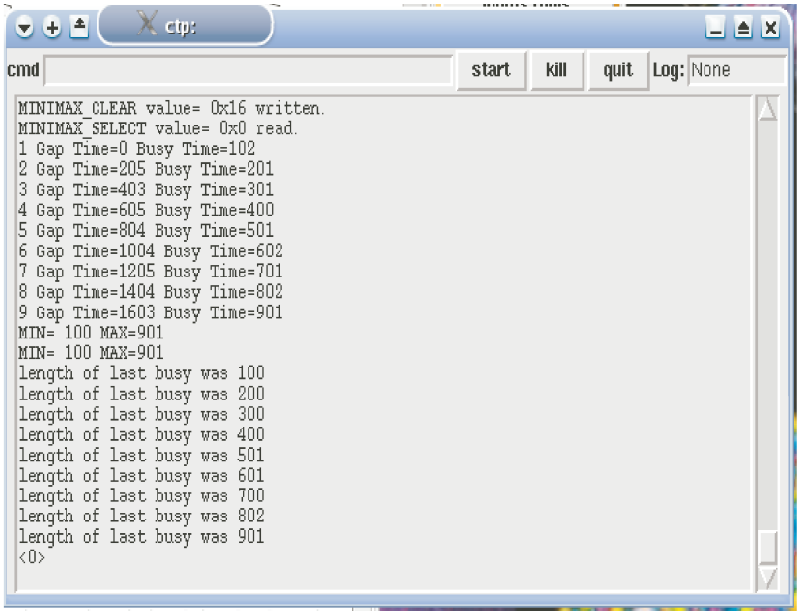

Figure 2.15: A demonstration of the test, demo(). Here, 'busy times' were set from 100 to 900 microseconds, separated by gaps from 100 to 1600 microseconds ('gap time'). BUSYMIN_DATA and BUSYMAX_DATA were then used to identify the measured minimum and maximum busy times, found to be 100 and 900 respectively ('MIN' and 'MAX'). This is followed by the busy times measured in the snapshot (indicated by 'length of last busy').

The measurements were checked again by reading the busy signals through an oscilloscope. The signals corresponding to a typical sequence are shown in Figure 2.16.

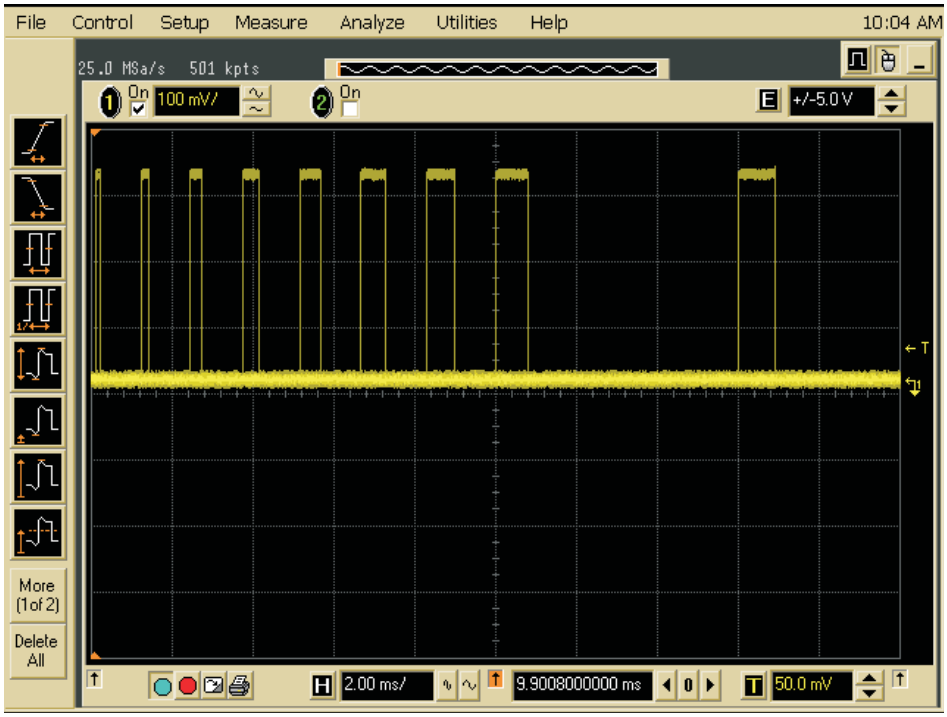

Figure 2.16: An example of the use of an oscilloscope to monitor the CTP busy independently.

Similar tests were carried out to establish that the BUSYlong generator was functioning correctly. MINIMAX_LIMIT was set in increments of 100 microseconds, and for each set limit a fixed number of busy signals were generated and measured, all of 900 microseconds in length and separated by 100 microseconds. This test showed that the number of counts remained constant up to 900 microseconds and was then zero, as expected.

2.3.3 TooBUSY: Developing The Software Tool

A TooBUSY tool was then created for use in the CTP software. As well as providing the ability to select functions by hand, a TooBUSY Sweep was developed, which made use of the BUSYlong generator to measure the busy time distribution. The detector or cluster, sweep range, step size, and time in seconds to spend on each point were requested as input. The MINIMAX_Limit was set, and BUSYlong counter was read at each interval. The result was recorded in a file which could be subsequently used to generate a graph. The method presumes that the distribution of busy

times does not change during a measurement (and if it does so dramatically this is symptomatic of other problems). In addition to producing the file, the tool has been designed to generate a warning when the maximum MINIMAX_Limit in the sweep range is exceeded.

An example of this tool being tested out on real busy signals is shown in Figure 2.17. During a cosmic data run in October 2008, a sweep was made over a range of 2000 μs on a cluster containing the ITS and TPC for 20 minutes. The average busy time was largest for the TPC, on average approximately 1600 μs. The results are shown both as an anti-cumulative data plot, simply showing the BUSYlong counts at each point, and as a differential data distribution, taking the ith point - the $i+1$th point from the first plot, so that steps in the anti-cumulative distribution are seen as peaks in the new distribution, corresponding to the most frequently generated busy time. Figure 2.17a. shows the busy time as a roughly flat distribution, dropping off at the TPC's characteristic value. This suggests that the deadtime of the TPC is stable. The next step would be to run the sweep on the individual detectors to evaluate the stability and length of their busy times.

The tool is more useful than simply the average busy time, because more information is given. It is a useful tool for identifying and diagnosing problems where one detector has occasional long periods of deadtime, and can identify when one detector is causing problems for a cluster.

Because in this case the data were obtained using a cosmic ray trigger, it took a long time to make a sweep with enough statistics. Because the measurements are independent of each other (they are made during different time intervals), the error on each data point is:

$$\sigma = \sqrt{(N_{(i)} + N_{(i+1)})} \tag{2.7}$$

This means many more statistics are required for a good measurement, and it also means that some values in the differential distribution can be negative, although they should not be less than zero within the larger errors.

In the case of simultaneous measurements (ie if the busy sweep could be measured all at once),

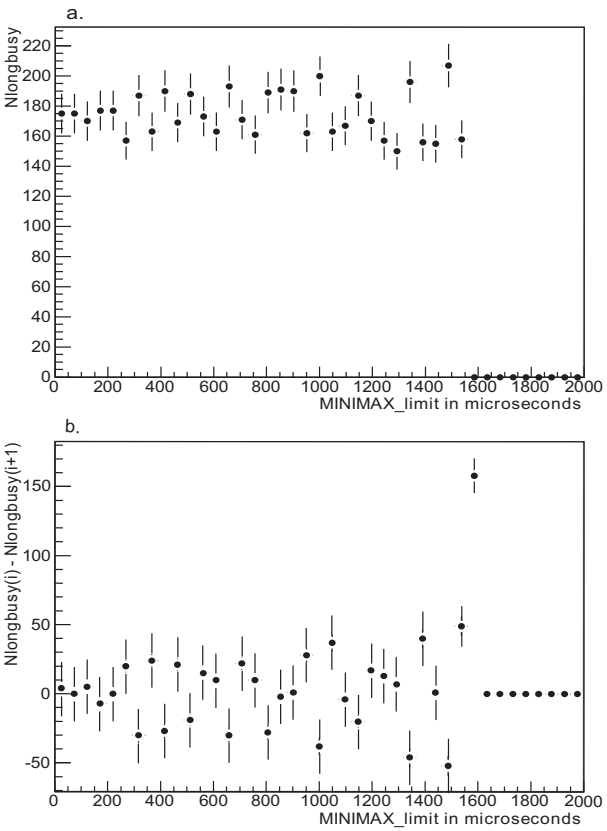

Figure 2.17: (a) The anti-cumulative graph resulting from a busy sweep of a cluster containing ITS and TPC over 2000 microseconds, using data from a cosmic run in October 2008. (b) The same graph represented as a differential plot, showing a sharp peak corresponding to the TPC's busy time value.

the statistical error on the entry in the ith bin in a differential data distribution would be:

$$\sigma = \sqrt{(N_{(i)} - N_{(i+1)})} \tag{2.8}$$

where i and i+1 the bin numbers of the anti-cumulative plot used to fill the ith bin of the differential distribution.

```
CINT/ROOT C/C++ Interpreter version 5.18.00, July 2, 2010
Type ? for help. Commands must be C++ statements.
Enclose multiple statements between { }.
Welcome to the Jan's ROOT session
root [0] .x busyplot.C
give 5 numbers with 1 space between each (in the following form):
a b c d e
where a is the end of your busysweep range (in microseconds)
b is the start of your busysweep range (in microseconds), or 0
c is the size of each step in the sweep (in microseconds)
d is the time spent measuring the busy PER STEP (in seconds)
and e is the detector number:
To find e, refer to below:
0 = CTP_BUSY
1-24: Detector BUSY (see table)
25-30 = Cluster 1 to 6 BUSY
31 = Test cluster BUSY
DETECTOR TABLE (BASED ON VALID.LTUs 03/10)
1=SDD    2=MUONTRK
3=MUONTRG    4=DAQ
5=SPD    6=TOF
7=VO    9=TRD
10=ZDC    11=EMCAL
13=TPC    14=PMD
15=ACORDE    17=SSD
18=FMD    19=TO
21=HMPID    22=PHOS
Please consider how long a full run will take with the options you provide
A sweep predicted to take longer than half an hour will abort.
EXAMPLE: to investigate busy distribution of the TPC when
its average busy is 4000 microseconds:
6000 2000 200 5 13
This run would last for approx. 100 seconds and observe
the range surrounding the TPCs average busy-length.
```

Figure 2.18: Helpful text instructing TooBUSY tool users on how to enter variables; busy sweep range end, busy sweep range start, sweep step size, time spent per step in the sweep and detector or cluster number.

Further development included an alternative running method through which the plots could be generated automatically when running the software. This was done by installing the ROOT framework [113] on to a different, remote Linux machine and allowing the two to communicate. This meant that the software could be run from the remote processor. Explanatory text was included to improve ease of use. An example is shown in Figure 2.18. Finally, the tool was installed as part of the CTP software.

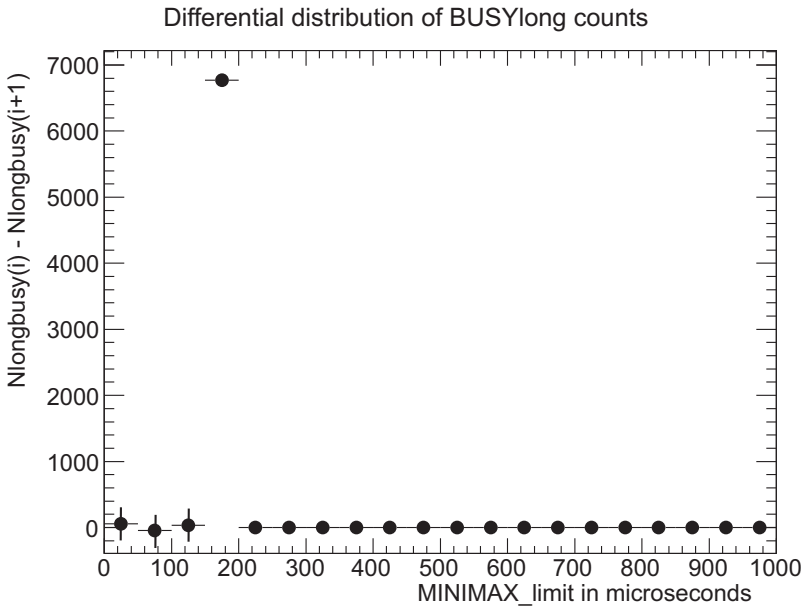

Figure 2.19: Typical TooBUSY differential distribution for the HMPID, showing the HMPID dead time of between 150 and 200 ms, taken from pp data taken in April 2011.

2.3.4 TooBUSY: Put into Use

Examples of the use of the tool during normal running to monitor individual detector busy distributions is shown in Figure 2.19 and 2.20, which show the differential plots produced during run 149881 on 24th April 2011. The L2 rate at this time was around 500 Hz. Figure 2.19 shows a sweep taken of the HMPID detector, whose average deadtime was 180 microseconds. Figure 2.20 shows the sweep for the TPC, which had a mean deadtime of around 400 microseconds. The distributions show, crucially, how much the busy signals fluctuate. The TPC's deadtime varies considerably from event to event, but the HMPID busy remains relatively fixed, illustrated by the sharp peak.

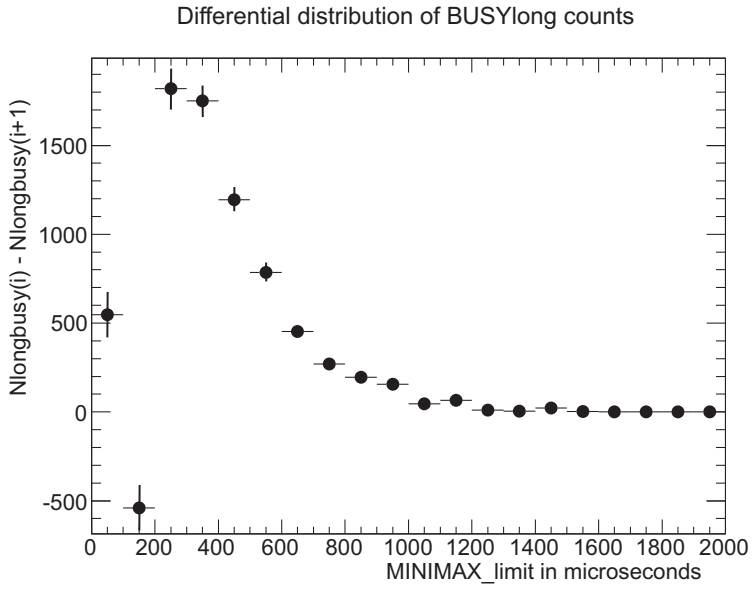

Figure 2.20: Typical TooBUSY differential distribution for the TPC, from pp data taken in April 2011. It is clear that the busy time fluctuates, because it is dependent on the event being read.

Chapter 3

Diffraction in pp Collisions at ALICE

3.1 Diffraction

One of the early measurements in proton-proton collisions made at ALICE at each energy is the pseudorapidity distribution of primary charged tracks [1]. Results are given for both inelastic and non-single-diffractive (NSD) events, in order to compare with other experimental measurements. For this reason, it is necessary to provide an estimate of the cross-sections of SD, DD and non-diffractive (ND) events, at each LHC energy, and estimate the uncertainty on this. The fractions and kinematics of diffractive events contributing to an event sample affect the shape of the distribution and are the largest source of error on the pseudorapidity density measurement.

The fractions and their uncertainty can be estimated using ALICE data and the result can be used to correct high-energy pseudorapidity distribution measurements, particularly at new energies where the fractions have not yet been measured.

This chapter first introduces the Monte Carlo (MC) models used throughout the analysis. Then various methods for measuring diffraction are described, focusing in particular on the UA5 approach, which has similarities with the author's method. The author's analysis method is introduced in a general way, and then explained in more detail specific to the ALICE detector. A MC study which tested the method's suitability is described. This MC study is outlined in an ALICE note, [2]. The implications and limitations of available data are considered, and corrections and systematic effects are evaluated. The results for 900 GeV and 7 TeV are presented, and are consistent with other measurements at these energies.

3.2 Introduction to MC Models: PYTHIA and PHOJET

In Section 3.4.3, PYTHIA 6.214 [67] (referred to as PYTHIA throughout the MC study) and PHOJET 1.12 [68] (subsequently referred to as PHOJET) are used to evaluate the suitability of a new method for extracting the diffractive fractions. In section 3.5, newer versions of PYTHIA are used; PYTHIA 6.421 ('Perugia 0' tuning [114], similar to PYTHIA 6.214 and referred to as PYTHIA 6 throughout this section) and PYTHIA 8.145 [115] (subsequently referred to as PYTHIA 8). The measurement of the diffractive fractions using real data, given in Section 3.5.5, uses all three MC models for estimating the kinematics of the diffractive processes. However, note that this final measurement is independent of the MC-predicted cross-sections.

PYTHIA and PHOJET are High Energy MC Event Generators - they can be used to generate, and describe, high energy physics collisions. They are used in combination with a description of the ALICE detector geometries and responses in order to produce simulated "data" samples for physics studies and comparison with real data. The diffractive cross-sections and the kinematics of the diffractive processes differ between the models, increasingly so with increasing collision energy.

PYTHIA 6, PYTHIA 8 and PHOJET pseudorapidity distributions are compared at 7 TeV in Figures 3.1 to 3.2, for the different processes.

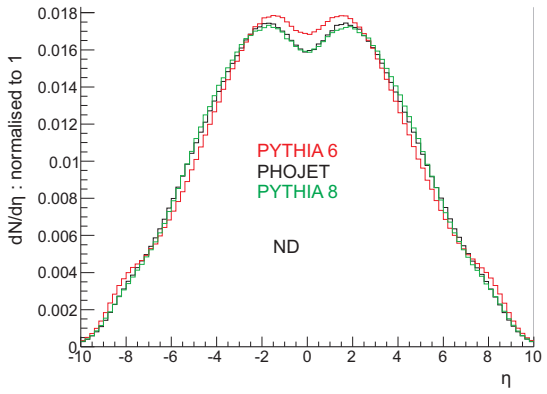

Figure 3.1: The normalised non-diffractive pseudorapidity distribution for PYTHIA, PYTHIA 8 and PHOJET at 7 TeV.

As can be seen from Figure 3.1, the non-diffractive distributions are in relatively good agreement.

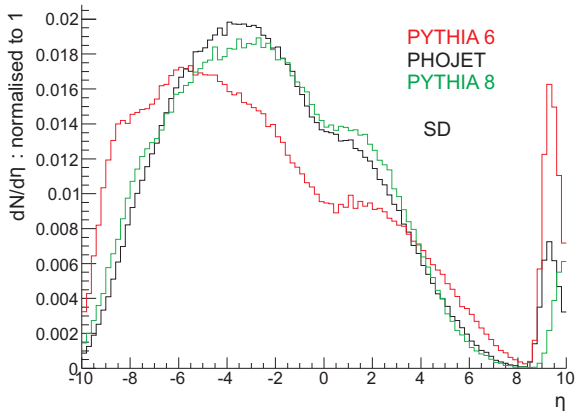

Figure 3.2: The normalised single-diffractive A-side pseudorapidity distribution for PYTHIA, PYTHIA 8 and PHOJET at 7 TeV.

The differences in kinematics are clear in Figures 3.2 and 3.4, which show the normalised pseudorapidity distributions of the diffractive processes.

Perturbative QCD is used to describe the hard processes in the simulations. For soft processes, different approaches are used, and this is one of the main reasons that the models differ in diffractive predictions. PYTHIA, based on the Lund model [116], uses the Schuler Sjostrand model [117] (based on Regge theory and pQCD) by default. PHOJET is based on QGSM (Quark Gluon String

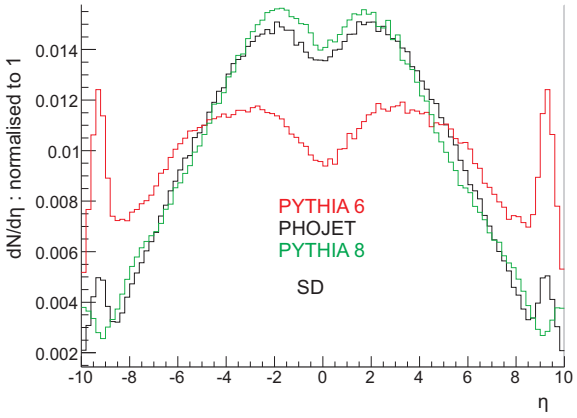

Figure 3.3: The normalised single-diffractive (both sides) pseudorapidity distribution for PYTHIA, PYTHIA 8 and PHOJET at 7 TeV.

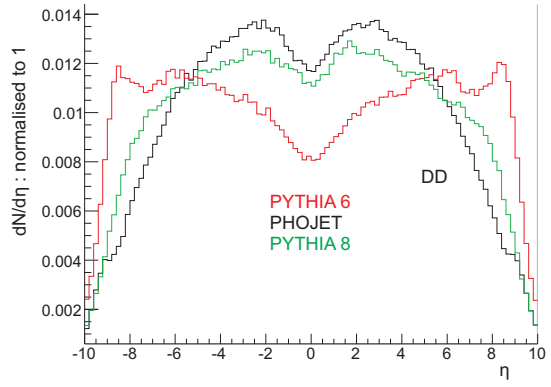

Figure 3.4: The normalised double-diffractive pseudorapidity distribution for PYTHIA, PYTHIA 8 and PHOJET at 7 TeV.

Model) [66] and the Dual Parton Model (DPM) [118]. In PHOJET, multiple Pomeron exchanges can occur at high diffractive mass, and DPE processes are included. For this study, DPE events have been classed as non-diffractive.

PYTHIA 6 contains no hard diffraction (Pomeron-proton) processes while PHOJET does. This is a large contribution to the difference in kinematics between PYTHIA and PHOJET that increases with energy, and for example, PYTHIA's steeply falling p_T distribution, as shown in 3.5 and 3.6.

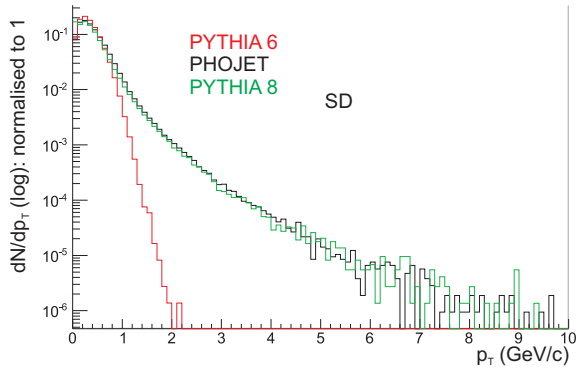

Figure 3.5: The normalised single-diffractive p_T distribution for PYTHIA, PYTHIA 8 and PHOJET at 7 TeV.

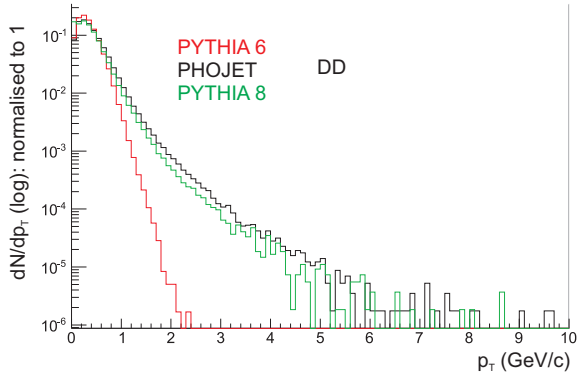

Figure 3.6: The normalised double-diffractive p_T distribution for PYTHIA, PYTHIA 8 and PHOJET at 7 TeV.

Again the difference in non-diffractive distributions is relatively small, as shown in figure 3.7.

To improve the PYTHIA model for the case where hard diffraction is appropriate, developments have been made to include these processes in a new release of PYTHIA, 8.217. Studies with this

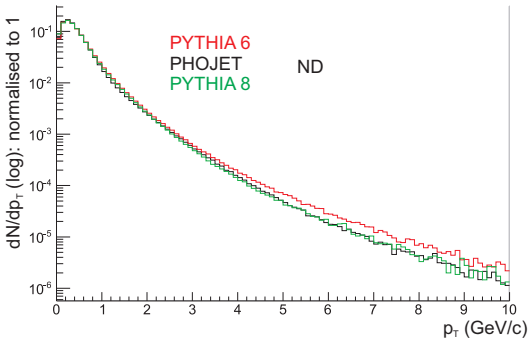

Figure 3.7: The normalised non-diffractive p_T distribution for PYTHIA, PYTHIA 8 and PHOJET at 7 TeV.

new model [115] have shown that the PHOJET and PYTHIA 8 p_T spectra are compatible with each other.

3.3 Methods for Measuring Diffraction

For detectors such as CDF [119], and soon, TOTEM [96], Roman Pots can be used to identify an intact proton in the beam pipe. This makes identification of Single Diffractive processes relatively straightforward, as well as providing sensitivity to elastic scattering. This is the ideal way to measure single diffraction.

One possible alternative method for measuring diffraction, adopted by, for example the ATLAS Collaboration [120], involves looking for the characteristic rapidity gap given by a diffractive process in the detector. Events can be selected based on whether they have a gap of a large enough size, and in principle events can be classified accordingly. There are several challenges to face with this method. Non-diffractive processes can leave gaps in rapidity, depending on the multiplicity, so a good understanding is needed of the efficiency of the rapidity gap selection. Not all diffractive processes have a measurable gap; it may be too small for the selection, or outside the acceptance of the detector. This clearly depends on the kinematics of the diffractive processes. It is also

important to ensure that the gaps are in the rapidity of primary particles - subsequent secondary interactions can cause initial gaps to change and this may be difficult to correct for. For this reason, when using the rapidity gap method, experimental definitions of diffraction are adopted, where (for example) rapidity gaps of a certain size are required in order to be classified as diffraction.

3.3.1 The UA5 Measurement

An alternative method for measuring diffraction, adopted by UA5, is to define triggers which select on different regions of pseudorapidity, and evaluate their efficiency to select on diffraction. This method is similar to the rapidity gap method, as (for example) an asymmetric trigger imposes a gap of a certain size based on the detector geometry. In this case, the definition of single and double diffraction comes from Monte Carlo. This makes the measurement more model dependent, but allows for comparison with theoretical predictions and other experiments.

UA5 was an experiment at the Super Proton anti-proton Synchrotron (Sp$\bar{\text{p}}$S) at CERN, which collided protons and anti-protons at 540 GeV [121]. In addition to this, some collisions with centre of mass energies of 200 and 900 GeV were also studied [70]. The UA5 experiment used information from upstream detectors at moderately forward rapidity to estimate the fraction of diffractive events. The detector consisted of two streamer chambers, placed above and below the beam pipe. The forward detectors were two arms on either side of the collision point, made up of trigger hodoscopes covering the pseudorapidity range $2 < |\eta| < 5.6$. Arm A1 was positioned on the side of the proton beam, and A2 was on the side of the anti-proton beam. To determine the fractions of single-diffractive and non-single-diffractive events for each energy, two different trigger combinations using the two arms were used; a two-arm trigger, A1 **AND**A2, which selected mostly non-single-diffractive events, and a one-arm trigger, A1 **AND NOT**A2, which selected mostly single-diffractive events. The alternative to this trigger, **NOT**A1 **AND**A2, was not used because it contained too much background. This is because the proton bunches were much more intense than the anti-proton bunches, leading to noise on the side of the intact proton A1 in the case of

SD events.

The two trigger types were used to determine the single-diffractive (SD) and non-single-diffractive (NSD) cross-sections in the following way. At each energy the total inelastic cross-section can be written as the sum of the single-diffractive and non-single-diffractive cross-sections,

$$\sigma_{inel} = \sigma_{SD} + \sigma_{NSD}. \tag{3.1}$$

Each trigger type yields a certain fraction of the events, which depends on the "efficiencies" of those triggers in triggering on each event type:

$$\sigma_1 = \sigma_{SD}\varepsilon^1_{SD} + \sigma_{NSD}\varepsilon^1_{NSD}; \tag{3.2}$$

$$\sigma_2 = \sigma_{SD}\varepsilon^2_{SD} + \sigma_{NSD}\varepsilon^2_{NSD}; \tag{3.3}$$

where these efficiencies ε are defined as

$$\varepsilon^{trig}_{proc} = \frac{N^{trig}_{proc}}{N^{gen}_{proc}} \tag{3.4}$$

for trigger types *trig* of 1 and 2, where process types *proc* are SD and NSD. If these efficiencies are known for both trigger types we can solve equations 3.2 and 3.3 to give

$$\sigma_{inel} = \chi_1\sigma_1 + \chi_2\sigma_2, \tag{3.5}$$

where each χ_i depends on the efficiencies $\varepsilon^{trig}_{proc}$. As the two trigger samples 1 and 2 were taken at the same time, they have the same luminosity. UA5 subsequently extended the method to take double diffraction into account, albeit with a large error [71].

Background contribution from beam-gas (BG) interactions was estimated using the primary vertex distribution. Beam-beam interactions are distributed around a central point as a Gaussian, whereas

beam-gas events may occur anywhere in the beam pipe and are observed as a flat background.

3.4 Diffraction at ALICE: The Extended UA5 Method

ALICE uses two approaches to measure diffraction. One of these uses rapidity gaps measured in the FMD and SPD. This thesis will describe the method developed by the author, which is similar to the approach taken by UA5.

The primary detectors used for the ALICE measurement, and for minimum-bias data selection, are the Silicon Pixel Detector (SPD) and V0 detectors. The SPD is a central ($|\eta| < 1.9$) detector used for vertex finding and fast triggering. The V0 detectors are arrays of scintillating counters covering -3.7 $< \eta <$ -1.7 (C side) and 2.8 $< \eta <$ 5.1 (A side).

The ALICE detector does not have full rapidity coverage, and, like UA5, is not sensitive to the intact protons of elastic or single-diffractive events. For a method involving rapidity gap selection, granularity in pseudorapidity would be needed, and this is not available in the triggering detectors. The FMD detector can do this, and covers a similar pseudorapidity range to the V0s. The FMD is used in ALICE's rapidity gap approach [79].

The FMD was not well tuned at the time of developing this method, and so a different approach was taken, using the kinematic distributions of models to provide an estimate of the efficiency of various triggers to select on diffractive events.

3.4.1 The Extended UA5 Method

One can consider the total number of inelastic events, N^{inel}, to be made up of a number of events of each process type. Fractions f_{proc}; (f_{SD} for the single-diffractive fraction, f_{DD} for the double-diffractive fraction, and f_{ND} for the non-diffractive fraction), are defined as N^{inel}_{proc}/N^{inel}, and sum to 1.

Now let us consider a sample of pp data that can be broken down into categories using several independent offline triggers. Ideally, the different triggers have a different sensitivity to each of the processes, such that each trigger provides additional information. For a given trigger type the number of triggered events N^{trig}, is defined as

$$N^{trig} = N^{inel}(\varepsilon^{trig}_{ND} f_{ND} + \varepsilon^{trig}_{SD} f_{SD} + \varepsilon^{trig}_{DD} f_{DD}), \tag{3.6}$$

where f_{proc} is the existing fraction of events of a given process type *proc* in the sample N^{inel} of inelastic events, and $\varepsilon^{trig}_{proc}$ is the efficiency $\frac{N^{trig}_{proc}}{N^{inel}_{proc}}$ of the trigger *trig* to select that process.

This assumes that the background, approximated to be principally from beam-gas events (BG), can be estimated, and so removed from the number of events triggered.

The efficiencies of each trigger to select on the different processes can be estimated using Monte Carlo simulated data. The events are simulated and reconstructed as if they have taken place in the detector, using GEANT [122]. Effects on the trigger efficiencies, such as dead detector zones, should be described as accurately as possible in the MC to match real data. Using these efficiencies, and the measured data, broken into several subsets *trig*, it should be possible to estimate the fractions using a χ^2 minimization. If the data sample can be broken down into a number of subsets, n, each of which is sensitive to a different region of pseudorapidity (for example), the minimization has n-3 degrees of freedom, because there are 4 free parameters to be evaluated (the three processes f_{proc} and N^{inel}), and one constraint that the process fractions sum to 1.

Now let us consider a variant of this approach. For a short time at each energy, parallel ALICE's minimum-bias trigger, a smaller fraction of beam-beam events were selected by each bunch-crossing (at a rate limited by the TPC dead-time, using signals from beam monitors to identify the filled bunches in the orbit). It was initially considered feasible to use these data to evaluate the counts for a zero-bias trigger.

A beam-beam trigger would provide a sample of events with a known normalisation - the number

of bunch-crossings N^{bc}, but would include an unknown fraction of events with no interaction, f_{NI} (which decreases with growing beam intensity). Clearly,

$$f_{NI} = 1 - f_{ND} - f_{SD} - f_{DD}. \tag{3.7}$$

The total number of triggered events N^{trig} can now be written as;

$$N^{trig} = N^{bc}(\varepsilon^{trig}_{ND} f_{ND} + \varepsilon^{trig}_{SD} f_{SD} + \varepsilon^{trig}_{DD} f_{DD} + \varepsilon^{trig}_{NI} f_{NI}), \tag{3.8}$$

where $\varepsilon^{trig}_{proc}$ is the efficiency for each trigger to select on events of a given process type. For a sample of events selected by bunch-crossing, the 'no interaction' process NI has a known efficiency. The trigger that fully negates all signals in the detector is 100% efficient in flagging these events, i.e. $\varepsilon^{0}_{NI} = 1$ and similarly $\varepsilon^{trig}_{NI} = 0$ for any other trigger, by definition. The number of degrees of freedom is still n-3, but n has increased by 1.

3.4.2 Using Extended UA5 Method at ALICE

In selecting a sample of 'minimum-bias' (MB) events, the Central Trigger Processor (CTP) uses as inputs the V0A, V0C and the SPD "Global Fast **OR**" (GFO). A beam gas trigger that uses timing information from the V0 detectors is also possible [123]. The minimum-bias trigger was designed to use a logical combination of the three detector inputs (see Table 3.1), and in practice usually uses MB1. The efficiencies for these triggers are shown in Table 3.2.

However, with these detectors there are many more possible combinations. There are 2^3 mathematically independent combinations (using only logical "**NOT**" and "**AND**"), if each input can be either negated or required. These trigger combinations can be seen in Table 3.3.

It can be seen from the Venn diagram in Figure 3.8 that these triggers do not overlap and are

Table 3.1: The minimum-bias trigger definitions. GFO is the Global Fast OR trigger of the SPD, while V0OR is defined as V0A **OR**V0C and V0AND is defined as V0A **AND**V0C.

Trigger	Definition
MB1	GFO **OR**V0OR
MB2	GFO **AND**V0OR
MB3	GFO **AND**V0AND
MB4	GFO **OR**V0AND

Table 3.2: The minimum-bias trigger efficiencies from a 100,000 event PYTHIA sample at 900 GeV.

Trigger	ε_{ND}	ε_{SD}	ε_{DD}
MB1	0.999	0.787	0.920
MB2	0.990	0.552	0.654
MB3	0.966	0.284	0.399
MB4	0.997	0.571	0.764

Table 3.3: 8 uncorrelated trigger definitions.

Trigger	Definition
Tr1	**NOT**GFO **AND NOT**V0A **AND NOT**V0C
Tr2	GFO **AND NOT**V0A **AND NOT**V0C
Tr3	**NOT**GFO **AND NOT**V0A **AND**V0C
Tr4	GFO **AND NOT**V0A **AND**V0C
Tr5	**NOT**GFO **AND**V0A **AND NOT**V0C
Tr6	GFO **AND**V0A **AND NOT**V0C
Tr7	**NOT**GFO **AND**V0A **AND**V0C
Tr8	GFO **AND**V0A **AND**V0C

therefore uncorrelated. It is possible to flag the events in a given sample to identify those that would have been triggered by a given combination, and find the resulting number of 'triggered' events N^{trig} offline. All of the events N^{inel} should be flagged by at least one of the triggers in Table 3.3 by definition, so that the sum of triggered events from all combinations should return the total number of events N^{inel}. However, Tr1 in this table is not measured by the minimum-bias trigger, and so cannot be evaluated. Therefore, if using minimum-bias data to evaluate the fractions, N^{inel} is unknown. For the purposes of describing the method, it is assumed that beam-beam triggered data can be used, using equation 3.8.

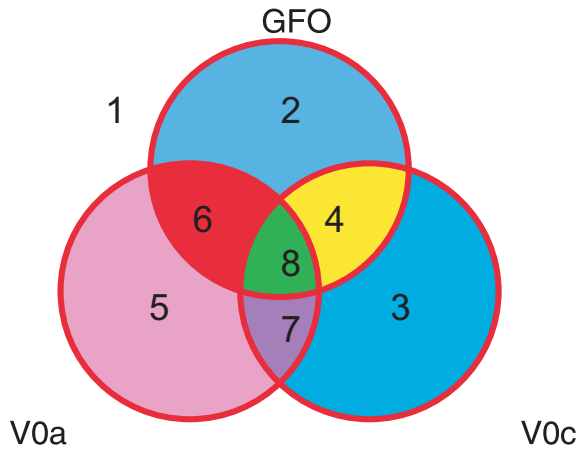

Figure 3.8: 8 uncorrelated triggers represented as sections of a Venn diagram.

χ^2 Minimization

A χ^2 minimization is carried out using MINUIT [124]. The χ^2 is defined as

$$\chi^2 = \sum \frac{(N_{fit}^{trig} - N_{measured}^{trig})^2}{(\sigma)^2}. \tag{3.9}$$

where σ is the uncertainty. This becomes

$$\chi^2 = \sum \frac{(N^{bc}(f_{ND}^{fit}\varepsilon_{ND}^{trig} + f_{SD}^{fit}\varepsilon_{SD}^{trig} + f_{DD}^{fit}\varepsilon_{DD}^{trig} + f_{NI}^{fit}\varepsilon_{NI}^{trig}) - N_{measured}^{trig})^2}{(\sigma_{stat})^2 + (\sigma_{model})^2} \tag{3.10}$$

where the statistical uncertainty σ_{stat} is $\sqrt{N^{trig}_{measured}}$. The model uncertainty is in the trigger efficiencies taken from one of the MC models and used in $\sqrt{N^{trig}_{fit}}$, and using error propagation this can be written as:

$$\sqrt{\left(\frac{\delta \mathrm{N}^{trig}_{fit}}{\delta \varepsilon_{ND}}\right)^2 (\sigma_{\varepsilon_{ND}})^2 + \left(\frac{\delta \mathrm{N}^{trig}_{fit}}{\delta \varepsilon_{SD}}\right)^2 (\sigma_{\varepsilon_{SD}})^2 + \left(\frac{\delta \mathrm{N}^{trig}_{fit}}{\delta \varepsilon_{DD}}\right)^2 (\sigma_{\varepsilon_{DD}})^2 + \left(\frac{\delta \mathrm{N}^{trig}_{fit}}{\delta \varepsilon_{NI}}\right)^2 (\sigma_{\varepsilon_{NI}})^2} \quad (3.11)$$

which becomes

$$\sqrt{(N^{bc})^2 \sum \left(f^2_{proc} \sigma^2_{\varepsilon_{proc}}\right)} \quad (3.12)$$

where f_{proc} of each process gives weight to each of the uncertainties. If one can assume that the diffractive kinematic distribution in the data is somewhere between the two MC distributions, the uncertainty on the efficiencies can be taken as half the difference between the two MC efficiencies (The real data should be compared with the models to be sure that this assumption is reasonable.) The resulting uncertainty for this study is:

$$\sqrt{(N^{bc})^2 \sum \left(f^2_{proc} (\frac{1}{2} \Delta \varepsilon_{proc})^2\right)} \quad (3.13)$$

Uncertainty due to noisy or dead zones not described perfectly in the MC, should also be estimated. This, as well as any underlying errors in the physics of the simulation, constitute the systematic uncertainty. This is taken as negligible for the MC study shown in Section 3.4.3 but estimated for the data analysis in Section 3.5.

The Inclusion of the Zero Degree Calorimeter (ZDC)

The pseudorapidity coverage of the V0s and SPD combined is approximately -3.7 $< \eta <$ 5.1. As can be seen from Figures 3.2 and 3.4, the largest differences between the double and single-diffractive pseudorapidity distributions lie further forward, in the region where most single-diffractive events are dramatically asymmetric. In fact, the picture is even more ambiguous than is clear in these

pictures, as here A-side only single-diffractive processes are shown, but individual double-diffractive processes are, to an extent, asymmetric as well. A double-diffractive event will typically have one large and one small diffracted side. In the acceptance of the SPD and V0s, these can be very difficult to distinguish from single-diffractive events.

In Section 3.4.3 it is explained that, whilst fit results using only the V0 and SPD detectors are satisfactory at 900 GeV (see Table 3.9 for the results of the MC study) at larger energies, where the difference in kinematics between models is more prominent, more information is needed to distinguish DD and SD.

The Zero Degree Calorimeter (ZDC) proton and neutron detectors are placed 117 m from the collision point. The ZN, positioned at zero degrees with respect to the LHC, has a pseudorapidity coverage of $\eta > 8.7$ for neutral particles, and the ZP will detect positive charged particles that are transported externally to the outgoing beam-pipe by the magnetic field (at high η but with coverage that depends on beam energy). Coverage at high η makes the ZDC ideal for distinguishing between diffractive processes. To use the ZDC for this purpose, an offline flag has been developed choosing a minimum threshold of energy deposited to indicate when at least one particle hits the detector [125]. Using the logical "**OR**" of the neutron and proton detectors for each side, we can introduce two more triggers (ZORA and ZORC) to the fit, and be sensitive to a more forward region of the events. This provides 2^5 trigger combinations, giving 28 degrees of freedom. The definition of the 32 trigger types is shown in Tables 3.4 and 3.5.

3.4.3 Effectiveness of the Model: MC Test

A study was carried out demonstrating the effect of changing both kinematics and diffractive process fractions on the effectiveness of the χ^2 minimization. Artificial 'data' samples are created with weighted diffractive fractions and trigger efficiencies.

It was found that changing the fractions in the data sample did not influence effectiveness of the

Table 3.4: The uncorrelated trigger definitions for the 32 trigger case. Triggers 1 - 16.

Trigger	Definition
Tr1	**NOT**GFO **AND NOT**V0A **AND NOT**V0C **AND NOT**ZORA **AND NOT**ZORC
Tr2	GFO **AND NOT**V0A **AND NOT**V0C **AND NOT**ZORA **AND NOT**ZORC
Tr3	**NOT**GFO **AND NOT**V0A **AND**V0C **AND NOT**ZORA **AND NOT**ZORC
Tr4	GFO **AND NOT**V0A **AND**V0C **AND NOT**ZORA **AND NOT**ZORC
Tr5	**NOT**GFO **AND**V0A **AND NOT**V0C **AND NOT**ZORA **AND NOT**ZORC
Tr6	GFO **AND**V0A **AND NOT**V0C **AND NOT**ZORA **AND NOT**ZORC
Tr7	**NOT**GFO **AND**V0A **AND**V0C **AND NOT**ZORA **AND NOT**ZORC
Tr8	GFO **AND**V0A **AND**V0C **AND NOT**ZORA **AND NOT**ZORC
Tr9	**NOT**GFO **AND NOT**V0A **AND NOT**V0C **AND**ZORA **AND NOT**ZORC
Tr10	GFO **AND NOT**V0A **AND NOT**V0C **AND**ZORA **AND NOT**ZORC
Tr11	**NOT**GFO **AND NOT**V0A **AND**V0C **AND**ZORA **AND NOT**ZORC
Tr12	GFO **AND NOT**V0A **AND**V0C **AND**ZORA **AND NOT**ZORC
Tr13	**NOT**GFO **AND**V0A **AND NOT**V0C **AND**ZORA **AND NOT**ZORC
Tr14	GFO **AND**V0A **AND NOT**V0C **AND**ZORA **AND NOT**ZORC
Tr15	**NOT**GFO **AND**V0A **AND**V0C **AND**ZORA **AND NOT**ZORC
Tr16	GFO **AND**V0A **AND**V0C **AND**ZORA **AND NOT**ZORC

Table 3.5: The uncorrelated trigger definitions for the 32 trigger case. Triggers 17 - 32.

Trigger	Definition
Tr17	**NOT**GFO **AND NOT**V0A **AND NOT**V0C **AND NOT**ZORA **AND**ZORC
Tr18	GFO **AND NOT**V0A **AND NOT**V0C **AND NOT**ZORA **AND**ZORC
Tr19	**NOT**GFO **AND NOT**V0A **AND**V0C **AND NOT**ZORA **AND**ZORC
Tr20	GFO **AND NOT**V0A **AND**V0C **AND NOT**ZORA **AND**ZORC
Tr21	**NOT**GFO **AND**V0A **AND NOT**V0C **AND NOT**ZORA **AND**ZORC
Tr22	GFO **AND**V0A **AND NOT**V0C **AND NOT**ZORA **AND**ZORC
Tr23	**NOT**GFO **AND**V0A **AND**V0C **AND NOT**ZORA **AND**ZORC
Tr24	GFO **AND**V0A **AND**V0C **AND NOT**ZORA **AND**ZORC
Tr25	**NOT**GFO **AND NOT**V0A **AND NOT**V0C **AND**ZORA **AND**ZORC
Tr26	GFO **AND NOT**V0A **AND NOT**V0C **AND**ZORA **AND**ZORC
Tr27	**NOT**GFO **AND NOT**V0A **AND**V0C **AND**ZORA **AND**ZORC
Tr28	GFO **AND NOT**V0A **AND**V0C **AND**ZORA **AND**ZORC
Tr29	**NOT**GFO **AND**V0A **AND NOT**V0C **AND**ZORA **AND**ZORC
Tr30	GFO **AND**V0A **AND NOT**V0C **AND**ZORA **AND**ZORC
Tr31	**NOT**GFO **AND**V0A **AND**V0C **AND**ZORA **AND**ZORC
Tr32	GFO **AND**V0A **AND**V0C **AND**ZORA **AND**ZORC

method, so the results are shown only for three data-samples, all with identical fractions, which are half-way between the two MC predictions (as indicated in Table 3.6).

Table 3.6: The fractions of single, double and non-diffractive events in each MC sample.

Sample	f_{ND}	f_{SD}	f_{DD}
TRUE PHOJET	0.724	0.192	0.084
TRUE PYTHIA	0.655	0.220	0.124
FRACTIONS USED FOR STUDY	0.690	0.206	0.104

The data samples are defined as follows:

"100% PHOJET" $N^{trig}_{measured}$ are weighted to PHOJET efficiencies

"50% PH 50 % PY" $N^{trig}_{measured}$ are weighted to $\frac{1}{2}\left(\varepsilon^{PHOJET}_{proc} + \varepsilon^{PYTHIA}_{proc}\right)$

"100% PYTHIA" $N^{trig}_{measured}$ are weighted to PYTHIA efficiencies

The χ^2 minimization was then carried out using efficiencies from each MC model as estimates.

Results Using 32 Triggers

The test described above was carried out at 900 GeV using all five detectors, giving 32 "uncorrelated" triggers. The results, using both PHOJET and PYTHIA coefficients, are shown in Tables 3.7 and 3.8. The sets of efficiencies for the two MC models are in Tables B.1, B.2, B.3 and B.4. The number of triggered events for each MC mix sample can be found in Tables B.5 and B.6.

The results for less triggers are given in Tables 3.9 and 3.10, for completeness. It is worth noting that without the ZDC, SD and DD separation was poor.

The fitted fractions and calculated MINOS [124] error contributions for the 50 % PYTHIA-PHOJET mix sample using 32 triggers are shown in the contour plot in Figure 3.9. The true

Table 3.7: The 900 GeV 32 trigger fit results for fractions of single, double and non-diffractive events in each N^{trig} sample, using the efficiencies from PHOJET.

Sample	f_{ND}	f_{SD}	f_{DD}	f_{NI}	χ^2
100 % PHOJET	0.692±0.004	0.209±0.005	0.100±0.003	0±0.007	0.2
50 % PH 50 % PY	0.657±0.015	0.212±0.017	0.115±0.02	0.02±0.03	19
100 % PYTHIA	0.615±0.016	0.205±0.018	0.146±0.021	0.03±0.03	56

Table 3.8: The 900 GeV 32 trigger fit results for fractions of single, double and non-diffractive events in each N^{trig} sample, using the efficiencies from PYTHIA.

Sample	f_{ND}	f_{SD}	f_{DD}	f_{NI}	χ^2
100 % PHOJET	0.745±0.008	0.211±0.013	0.044±0.011	0±0.018	80
50 % PH 50 % PY	0.717±0.009	0.212±0.015	0.071±0.013	0±0.0216	21
100 % PYTHIA	0.69±0.01	0.218±0.017	0.091±0.014	0±0.02	5

fractions of the sample and the fractions in the MC are also shown. It is clear that the uncertainty estimation is appropriate for this 'data' sample.

An interesting point to note from this figure is the anti-correlation between the SD and DD. It seems that even using the ZDC in the trigger logic, there is some ambiguity in the SD and DD events. It is suggested at this point that separating SD and DD may not be in the scope of this measurement, particularly in the case of only 8 triggers, where the acceptance is worse.

Table 3.9: The 900 GeV 8 trigger fit results for fractions of single, double and non-diffractive events for the 50 % PH 50 % PY sample, using the efficiencies from PHOJET and PYTHIA. In this case, there are 5 degrees of freedom.

Sample	Efficiencies	f_{ND}	f_{SD}	f_{DD}	f_{NI}	χ^2
50 % PH 50 % PY	PHOJET	0.648±0.018	0.182±0.022	0.149±0.028	0.02±0.04	1
50 % PH 50 % PY	PYTHIA	0.710±0.010	0.205±0.028	0.084±0.027	0±0.040	5

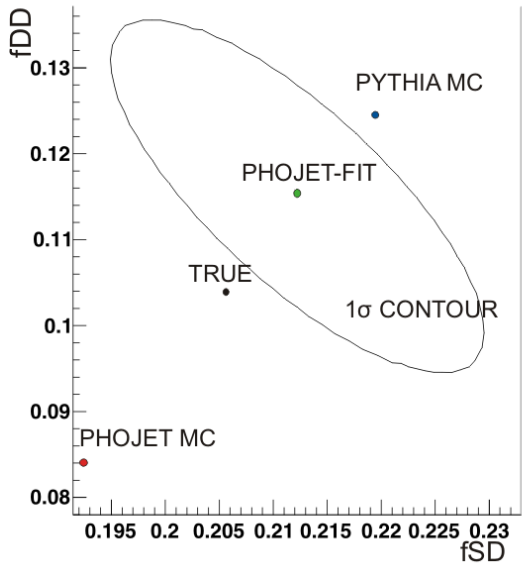

Figure 3.9: Contour plot showing the PHOJET-fitted (green) and true (black) fractions f_{SD} and f_{DD} for the 50 % PYTHIA-PHOJET mix sample, with the 1 σ error range. The contour demonstrates that the uncertainty estimation is reasonable for this sample. The PHOJET (red) and PYTHIA (blue) fractions are also shown.

Table 3.10: The 900 GeV 28 (minimum bias) trigger fit results for fractions of single, double and non-diffractive events in the 50 % PH 50 % PY sample, using the efficiencies from PHOJET and PYTHIA. In this case, there are 25 degrees of freedom.

Sample	Efficiencies	f_{ND}	f_{SD}	f_{DD}	N^{inel}	χ^2
50 % PH 50 % PY	PHOJET	0.670±0.013	0.213±0.017	0.117±0.021	100000±740	16
50 % PH 50 % PY	PYTHIA	0.710±0.010	0.229±0.016	0.061±0.012	101600±1400	14

Summary

As expected, the χ^2 is small when the MC efficiencies used match the sample. As the efficiencies of the sample deviate further from the estimates, the results are poorer, and in the case where they deviate further than the model uncertainty allows for, the errors are underestimated and the χ^2 is large.

For the data sample used, statistics were limited and some triggers were not well populated. This was taken into account in the statistical uncertainty but not in the model uncertainty.

The conclusions from the study are that efficiencies from several models should be used, and should be calculated with as large a data sample as possible. A large deviation in kinematics from the efficiencies used will lead to a large χ^2. Error estimation is adequate provided this is avoided.

3.5 Measuring Diffraction: Diffractive Fractions for 900 GeV and 7 TeV Data

Small samples (around 150,000 events) of PYTHIA 8 were made available for use, in addition to PYTHIA 6 and PHOJET. Sample sizes of between 150,000 and 350,000 events were used from simulations and data, ensuring enough statistics in calculating trigger efficiencies and consistency between model and data statistical fluctuation.

3.5.1 Minimum-bias vs beam-beam trigger

Whilst beam-beam data were taken, as the interaction rates were low in the collisions, most beam-beam events could be characterised as 'non-interacting'. Unfortunately this meant that f_{NI} dominated Tr1, and this trigger counted much more than any other, and the sample did not provide suitable sensitivity to the diffractive fractions. For this reason, the final results use minimum-bias

data taken with MB1 (See Table 3.1), and only "uncorrelated" triggers that are subsets of this can be used. This equates to 7 triggers using V0 and SPD (excluding Tr1), or 28 triggers if including the ZDC (excluding Tr1, Tr9, Tr17 and Tr25). The unknown value N^{inel} must be evaluated in the minimization along with the fractions. Sensitivity to the number of missed events comes from the efficiencies (estimated from MC models), which do not sum to 1 for all measured triggers. The fraction f_{NI} no longer needs to be evaluated. A short study using the same MC as the previous section has been conducted to show this is possible, and the fit result is satisfactory, as shown in Table 3.10.

3.5.2 Three MC's for Model Uncertainty Estimation

With the introduction of PYTHIA 8, the fit results could be evaluated for 3 different sets of efficiencies, and the range of uncertainty on each of these efficiencies was taken to be the largest difference between the three MC estimates. This is not necessarily a thorough overview of the model uncertainty, but instead reflects the range of available simulated ALICE data at the time of writing this thesis. Clearly, if (for example) hard diffraction as described by PHOJET and PYTHIA 8 is appropriate, the model uncertainty could be much smaller than implied by this. Equally, it is not completely clear that these three MCs fully describe the uncertainty in the kinematics.

3.5.3 Data availability and Quality Checks

As can be seen in Tables B.1 to B.4, the ZDC is not expected to be very efficient at 900 GeV. In fact, the magnetic field from the ALICE dipole creates an internal crossing angle of the beams that changes with energy [126]. At 7 TeV, this crossing angle was enough to require raising the ZN detector. At 900 GeV, the effect was much larger. This meant that data at 900 GeV could not be trusted. In addition to this, the ZDC's energy distributions were not tuned in the MC for 900 GeV at the time of writing this thesis. For these reasons, only 7 triggers could be used to evaluate the fractions at 900 GeV. As was explained in the MC study, distinguishing between DD and SD is

more difficult when only using the V0 and SPD acceptance. However, results for all three fractions are shown for completeness.

During 7 TeV data-taking, a problem involving machine induced background was found to affect the ZDC, illustrated in Figure 3.10. In the incoming beam pipes there are collimators designed to reduce beam-halo. However, the jaws of the collimators (above and below the beam pipe) are encroaching on the space between the beam pipes, and so interfere with the spectator neutrons upstream of the ZN detector.

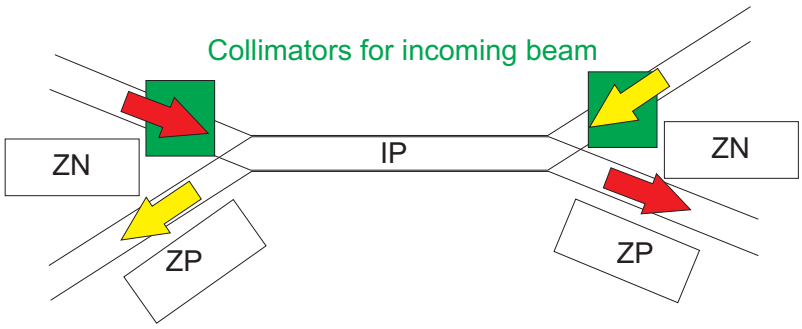

Figure 3.10: Schematic representation of the incoming and outgoing beams, the collimator positions for the incoming beams and their interference with the ZDC.

The effect this would have on the data is not very clear, and it is not included in the GEANT simulation. Both the 28 ZDC-dependent triggers and the 7 ZDC-independent triggers were used to evaluate the fractions, for completeness, but the 28 trigger data were thought not to be trusted, and the 7 trigger fit was more successful.

To evaluate the suitability of the data, various quality checks were carried out. Looking at the normalised hit distributions in ϕ of the SPD and V0 in data compared to simulation demonstrates how well detector effects were evaluated. For example, the SPD "good" chips fluctuate a little from one run to another, so it is important that they match in the samples used. These plots are shown in Figures 3.11 and 3.12.

For the SPD, the plot shows hits in the chips along one stave at a time, going around in ϕ (first

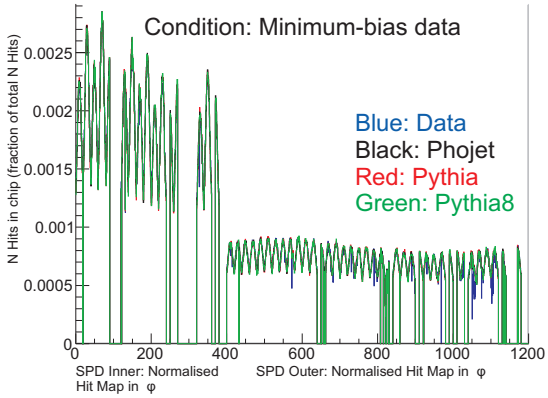

Figure 3.11: Normalised hit distribution in ϕ for SPD in 7 TeV data given the condition Tr8: Inner layer (left) and Outer layer (right), for data (blue), PHOJET, PYTHIA 6 and PYTHIA 8.

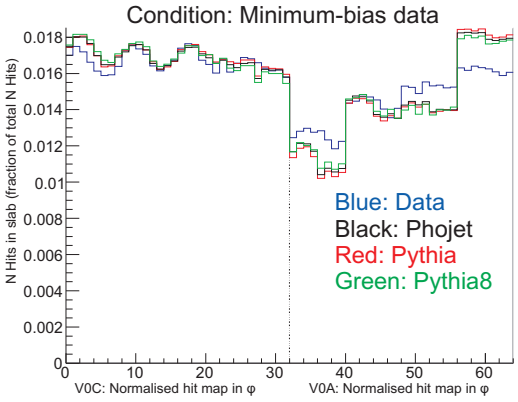

Figure 3.12: Normalised hit distribution in ϕ for V0 in 7 TeV data: C side (left) and A side (right), for data (blue), PHOJET, PYTHIA 6 and PYTHIA 8.

for the Inner then the Outer layer). The hits across each stave fluctuate (over the two units of pseudorapidity) but the hits in ϕ remain fairly flat. For the V0, the hit distribution in ϕ is plotted (sector by sector) for each ring separately (first for the C side, then for the A side). For this reason, there are steps in the distribution - each ring is measuring different slices in the pseudorapidity density. This is most clearly seen on the A side, which covers a more forward (steeply falling) region of pseudorapidity.

In addition to these plots, the hit distributions given different trigger conditions were also investigated, as shown in Figures 3.13 to 3.20.

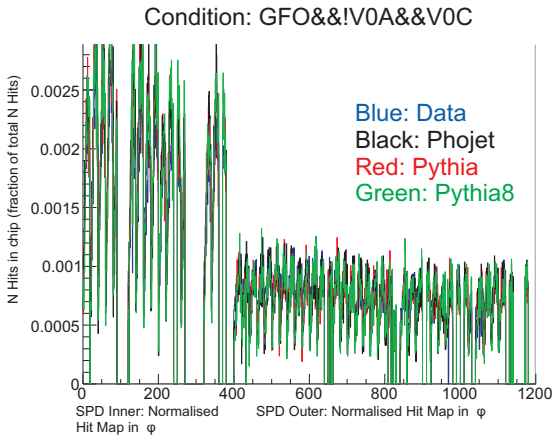

Figure 3.13: Normalised hit distribution in ϕ for SPD in 7 TeV data, given the condition Tr4 (see Table 3.4): Inner layer (left) and Outer layer (right), for data (blue), PHOJET, PYTHIA 6 and PYTHIA 8.

For SPD, the agreement is very good.

For the V0, one can see discrepancy in the MC, particularly in V0A.

The dependence on rapidity plays a role in this, but there are also detector effects that may not be well described in the MC, such as incorrectly described material budget in individual rings or sectors, and scintillation in the optical fibres.

The pulse height (mV) of an analogue signal in the V0 determines whether a digital hit is accepted - it must exceed a set threshold (to cut out noise). The height of each pulse can be plotted in an

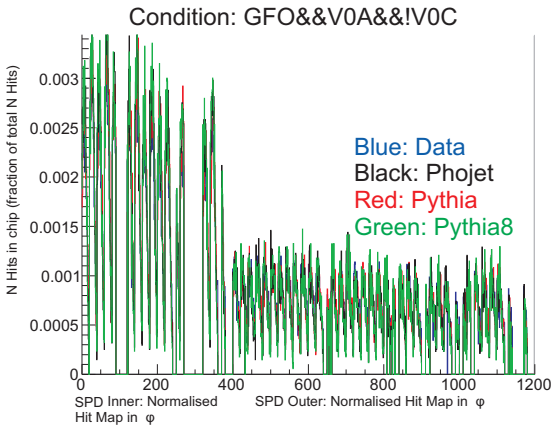

Figure 3.14: Normalised hit distribution in ϕ for SPD in 7 TeV data, given the condition Tr6 (see Table 3.4): Inner layer (left) and Outer layer (right), for data (blue), PHOJET, PYTHIA 6 and PYTHIA 8.

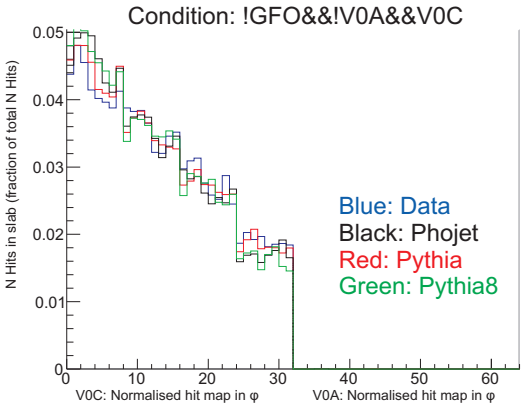

Figure 3.15: Normalised hit distribution in ϕ for V0 in 7 TeV data, given the condition Tr3 (see Table 3.4): C side (left) and A side (right), for data (blue), PHOJET, PYTHIA 6 and PYTHIA 8.

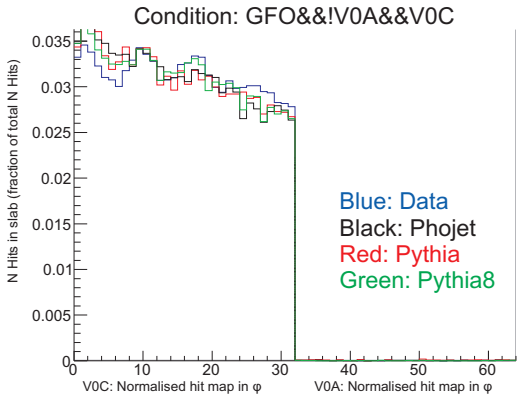

Figure 3.16: Normalised hit distribution in ϕ for V0 in 7 TeV data, given the condition Tr4 (see Table 3.4): C side (left) and A side (right), for data (blue), PHOJET, PYTHIA 6 and PYTHIA 8.

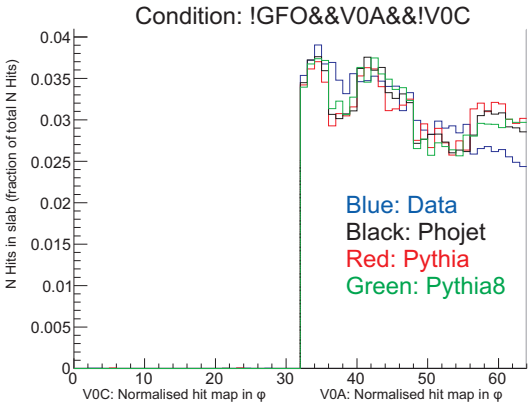

Figure 3.17: Normalised hit distribution in ϕ for V0 in 7 TeV data, given the condition Tr5 (see Table 3.4): C side (left) and A side (right), for data (blue), PHOJET, PYTHIA 6 and PYTHIA 8.

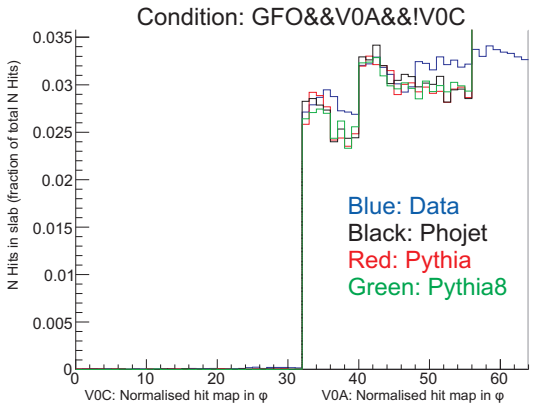

Figure 3.18: Normalised hit distribution in ϕ for V0 in 7 TeV data, given the condition Tr6 (see Table 3.4): C side (left) and A side (right), for data (blue), PHOJET, PYTHIA 6 and PYTHIA 8.

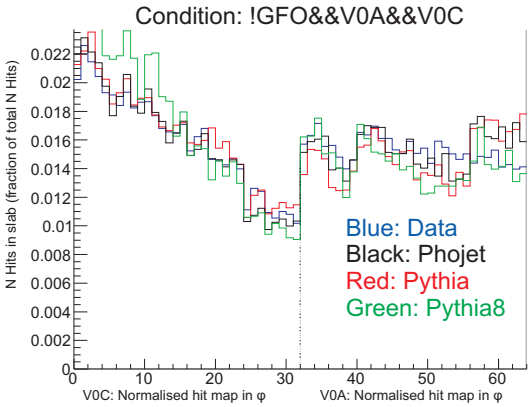

Figure 3.19: Normalised hit distribution in ϕ for V0 in 7 TeV data, given the condition Tr7 (see Table 3.4): C side (left) and A side (right), for data (blue), PHOJET, PYTHIA 6 and PYTHIA 8.

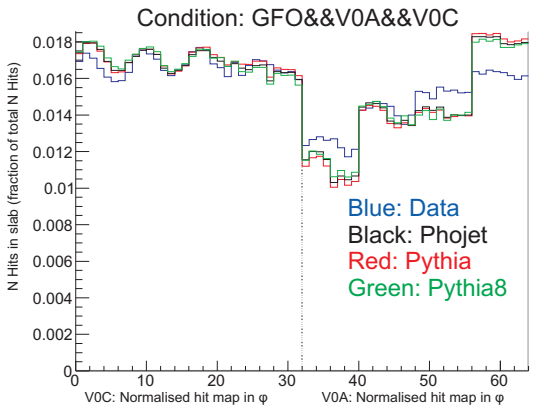

Figure 3.20: Normalised hit distribution in ϕ for V0 in 7 TeV data, given the condition Tr8 (see Table 3.4): Inner layer (left) and Outer layer (right), for data (blue), PHOJET, PYTHIA 6 and PYTHIA 8.

Analogue Digital Converter (ADC) spectrum. Examples of this are shown in Figures 3.21 to 3.22. They are normalised to 1 to compare the shapes.

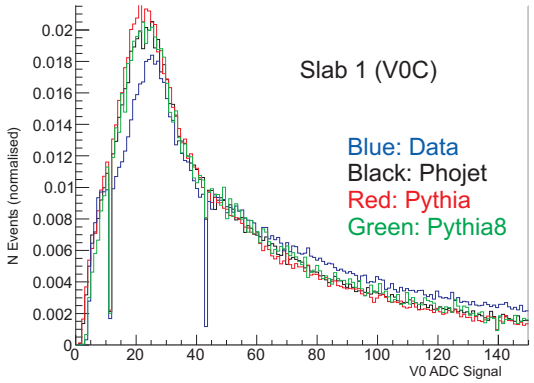

Figure 3.21: ADC Spectra for V0C Slab 1: 7 TeV data (blue), PHOJET, PYTHIA 6 and PYTHIA 8. Note that the dips are artefacts of the way in which the ADC counts are incremented.

The threshold was set to a value corresponding to one ADC count, for all slabs during data-taking. In some sectors small discrepancies were seen in data compared to MC. In particular, a characteristic shoulder was found in many of them, (see Figures 3.21 and 3.22).

Also, in a few sectors the MC predicted a very different shape to what was seen (see Figure 3.23). Only 9 slabs were found with this effect, the effect is present at both 900 GeV and 7 TeV, and in

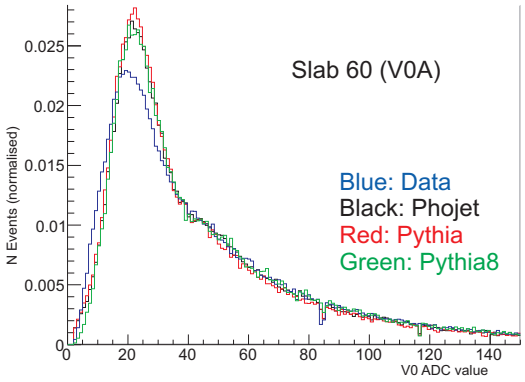

Figure 3.22: ADC Spectra for V0C Slab 60: 7 TeV data (blue), PHOJET, PYTHIA 6 and PYTHIA 8.

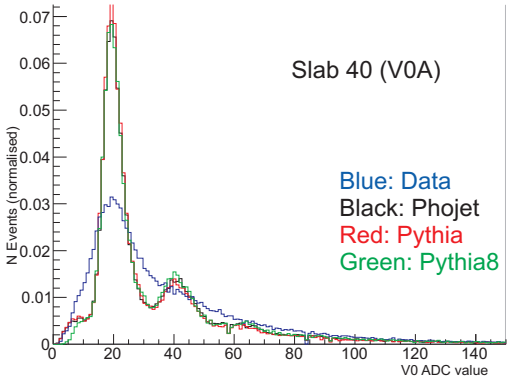

Figure 3.23: ADC Spectra for V0C Slab 40: 7 TeV data (blue), PHOJET, PYTHIA 6 and PYTHIA 8.

all cases the effect is visibly dramatic, so these slabs were removed by eye to see the effect on the fit.

The effect of these anomalies is estimated and added to the systematic error in Section 3.5.6.

3.5.4 Corrections

During data-taking a number of bunch crossing "slots" in the LHC's orbits were filled with one-sided beam events (one bunch only) and empty events (no bunches). These events were selected with minimum bias and used to evaluate the offline triggers' selection of beam gas (N_A^{BG} for A side beam counts and N_C^{BG} for C side beam counts) and noise, (N^E for empty bunch counts) respectively. The correction to the data is then, in principle, N^{trig}-(N_A^{BG}+N_C^{BG})+N^E, or N^{trig}-N^{BG}+N^E. The additional E term is because each of the one-sided beam-gas samples also contain noise. Note that each element of the correction had to be normalised relative to the filling schemes. An example of their contribution is shown in Table 3.11.

In fact, in the reconstruction of the data (not done by the author), V0 timing information was used to remove the majority of background events, as described in Section 2.2.5. Table 3.11 also shows the number of triggers remaining after this timing correction, labelled as $N_{corrected}^{trig}$, $N_{corrected}^{BG}$ and $N_{corrected}^{E}$. The remaining correction (completed by the author) is quite small.

The statistical uncertainty was taken as the sum $\sqrt{N_{corrected}^{trig} + N_{corrected}^{BG} + N_{corrected}^{E}}$. The final number of triggers in the data samples used are shown in Tables B.13 and B.14.

3.5.5 Diffractive Fractions: Results for 900 GeV and 7 TeV Data

The results for the Diffractive fractions at 7 TeV using 28 triggers are shown in Table 3.12. The result was very poor, indicating an effect not described by the MC. This was discovered to be caused by collimator noise in the ZDC.

Table 3.11: The number of triggers, N^{trig}, and number of beam gas and empty triggers contaminating the sample, as estimated using A side only and C side only (N^{BG}) and empty (N^{E}) bunch slots respectively. $N_{corrected}$ show the remaining number of triggers in each category after using V0 timing information to eliminate background. Note that the number of beam gas and empty events have been normalised based on the filling schemes such that they are the 'true' contributions to the correction. Taken from 7 TeV MB data.

Trigger	N^{trig}	N^{BG}	N^{E}	$N^{trig}_{corrected}$	$N^{BG}_{corrected}$	$N^{E}_{corrected}$
Tr2	2384	162	1908	280	32	5
Tr3	2272	76	28	1466	98	2
Tr4	3712	97	0	1847	167	0
Tr5	4468	95	397	2074	76	71
Tr6	3033	29	0	1524	112	0
Tr7	1370	47	0	527	2	0
Tr8	87989	394	0	43443	74	0

Table 3.12: The 28 trigger fit results for 7 TeV data: fractions of single, double and non-diffractive events (f_{SD}, f_{DD} and f_{ND} respectively), and the total number of inelastic events N^{inel} using the efficiencies from PHOJET, PYTHIA 6 and PYTHIA 8 respectively. The number of degrees of freedom in this case is 25.

Efficiencies	f_{ND}	f_{SD}	f_{DD}	N^{inel}	χ^2
PHOJET	0.644±0.019	0.154±0.021	0.201±0.027	295900±4600	38
PYTHIA 6	n/a	n/a	n/a	n/a	154 (FAILED)
PYTHIA 8	n/a	n/a	n/a	n/a	83 (FAILED)

The results for 7 triggers at 900 GeV and 7 TeV are given in Tables 3.13 and 3.14 respectively.

Table 3.13: The 7 trigger fit results for 900 GeV data: fractions of single, double and non-diffractive events (f_{SD}, f_{DD} and f_{ND} respectively), and the total number of inelastic events N^{inel} using the efficiencies from PHOJET, PYTHIA 6 and PYTHIA 8 respectively. The number of degrees of freedom in this case is 4.

Efficiencies	f_{ND}	f_{SD}	f_{DD}	N^{inel}	χ^2
PHOJET	0.68±0.032	0.141±0.044	0.181±0.061	339300±7200	6
PYTHIA 6	0.722±0.016	0.201±0.039	0.077±0.043	351800±6400	4
PYTHIA 8	0.735±0.015	0.154±0.034	0.111±0.03	334000±19000	14

Table 3.14: The 7 trigger fit results for 7 TeV data: fractions of single, double and non-diffractive events (f_{SD}, f_{DD} and f_{ND} respectively), and the total number of inelastic events N^{inel} using the efficiencies from PHOJET, PYTHIA 6 and PYTHIA 8 respectively. The number of degrees of freedom in this case is 4.

Efficiencies	f_{ND}	f_{SD}	f_{DD}	N^{inel}	χ^2
PHOJET	0.695±0.014	0.13±0.045	0.17±0.052	295000±5200	19
PYTHIA 6	0.72±0.011	0.229±0.056	0.051±0.052	306200±4300	16
PYTHIA 8	0.71±0.013	0.09±0.063	0.2±0.058	299600±5700	29

3.5.6 Evaluation of Systematic Uncertainty

Table 3.15 shows the results for 7 TeV after setting a higher ADC threshold on the V0s. This was to estimate the impact of the "shoulder" seen in the spectra, not reproduced by MC ADC spectra.

Table 3.16 shows the results for 7 TeV after removing the V0 slabs for which the ADC spectra was very different to that predicted by MC.

It appears that the dominant source of uncertainty on the MC comes from the model uncertainty itself. However, the behaviour of an event as it travels through the detector is a very important part of the MC simulation. In order to estimate the effect of getting this wrong, Tables 3.17 and 3.18 show the results for 900 GeV with 10% less and 10% greater material budget respectively.

Table 3.15: The 7 trigger fit results for 7 TeV data after modifying V0 ADC threshold to >10: fractions of single, double and non-diffractive events (f_{SD}, f_{DD} and f_{ND} respectively), and the total number of inelastic events N^{inel} using the efficiencies from PHOJET, PYTHIA 6 and PYTHIA 8 respectively.

Efficiencies	f_{ND}	f_{SD}	f_{DD}	N^{inel}	χ^2
PHOJET	0.74±0.017	0.171±0.038	0.089±0.052	284800±3100	19
PYTHIA 6	0.766±0.008	0.172±0.039	0.062±0.042	285800±3400	17
PYTHIA 8	0.742±0.013	0.041±0.06	0.216±0.066	289000±6900	13

Table 3.16: The 7 trigger fit results for 7 TeV data after removing V0 slabs with poorly reproduced MC ADC Spectra: fractions of single, double and non-diffractive events (f_{SD}, f_{DD} and f_{ND} respectively), and the total number of inelastic events N^{inel} using the efficiencies from PHOJET, PYTHIA 6 and PYTHIA 8 respectively.

Efficiencies	f_{ND}	f_{SD}	f_{DD}	N^{inel}	χ^2
PHOJET	0.695±0.013	0.131±0.044	0.175±0.051	295000±5100	21
PYTHIA 6	0.721±0.011	0.223±0.059	0.057±0.054	305200±4400	16
PYTHIA 8	0.709±0.013	0.091±0.067	0.2±0.062	300500±6400	26

Note that this is applied globally, so it may not completely cover material budget errors that are asymmetric in η.

Table 3.17: The 7 trigger fit results for 900 GeV data after reducing material budget in MC by 10%: fractions of single, double and non-diffractive events (f_{SD}, f_{DD} and f_{ND} respectively), and the total number of inelastic events N^{inel} using the efficiencies from PYTHIA 6.

Efficiencies	f_{ND}	f_{SD}	f_{DD}	N^{inel}	χ^2
PYTHIA 6	0.723±0.016	0.199±0.038	0.078±0.042	351200±6300	5

Table 3.18: The 7 trigger fit results for 900 GeV data after increasing material budget in MC by 10%: fractions of single, double and non-diffractive events (f_{SD}, f_{DD} and f_{ND} respectively), and the total number of inelastic events N^{inel} using the efficiencies from PYTHIA 6.

Efficiencies	f_{ND}	f_{SD}	f_{DD}	N^{inel}	χ^2
PYTHIA 6	0.728±0.017	0.184±0.043	0.088±0.047	350500±6800	4

An extension to simply looking at the difference between available generators is to investigate the effect that a change in diffractive mass has on the kinematics, and to determine to which part of the diffractive mass spectrum the triggers are sensitive.

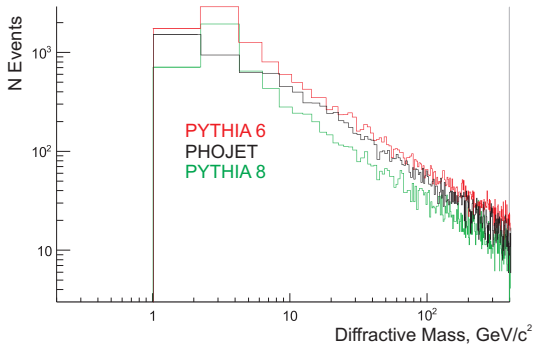

Figure 3.24: The diffractive mass distribution of PHOJET, PYTHIA 6 and PYTHIA 8 SD events in 7 TeV pp collisions.

Figure 3.24 shows the diffractive mass distribution predicted in each of the MC models. It is clear that the low mass part dominates. The diffractive mass is obtained by locating the intact proton

and using:

$$M^2_{diff} = (P_a + P_b - P'_a) = P^2_X \tag{3.14}$$

where P_a and P_b are the four-momenta of the incoming protons and P'_a is the four momentum of the outgoing intact proton.

Figures 3.25 to 3.32 show the sensitivity of the 8 uncorrelated triggers to diffractive mass.

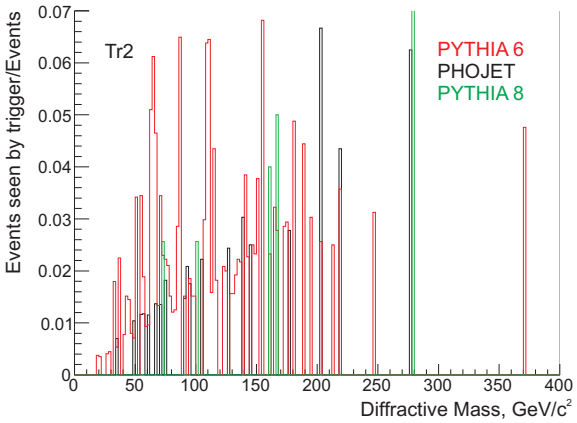

Figure 3.25: The diffractive mass acceptance of Tr2 at 7 TeV: measured / true diffractive mass distribution.

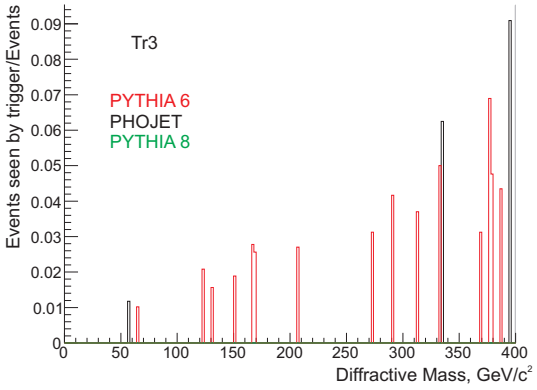

Figure 3.26: The diffractive mass acceptance of Tr3 at 7 TeV: measured / true diffractive mass distribution.

It is clear that the presence of a hit in the SPD alongside the V0 detector on the side of the diffracted mass influences the triggers by making them more sensitive to higher diffractive masses - for example in Figures 3.29 and 3.31.

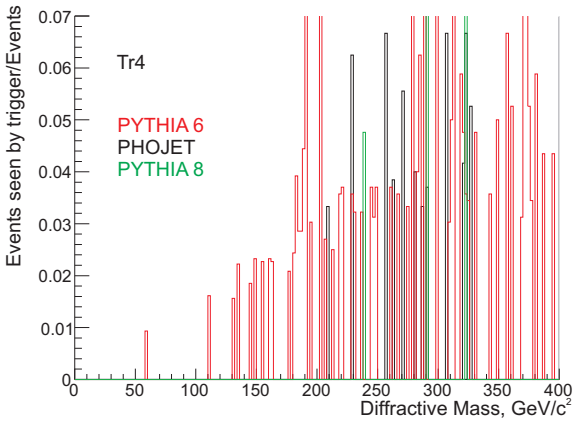

Figure 3.27: The diffractive mass acceptance of Tr4 at 7 TeV: measured / true diffractive mass distribution.

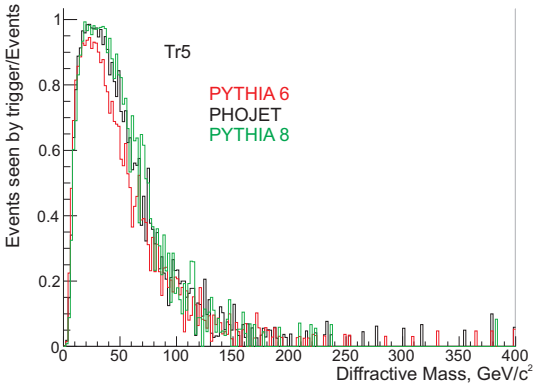

Figure 3.28: The diffractive mass acceptance of Tr5 at 7 TeV: measured / true diffractive mass distribution.

In addition to this, the trigger selecting only the V0 detector on the side of the diffracted mass and no hits anywhere else is most sensitive to the low mass diffraction, as shown in Figure 3.28.

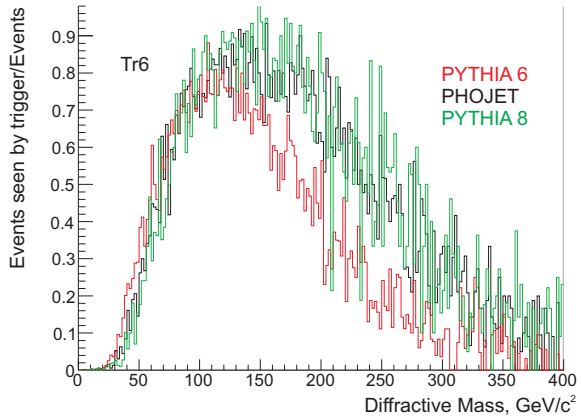

Figure 3.29: The diffractive mass acceptance of Tr6 at 7 TeV: measured / true diffractive mass distribution.

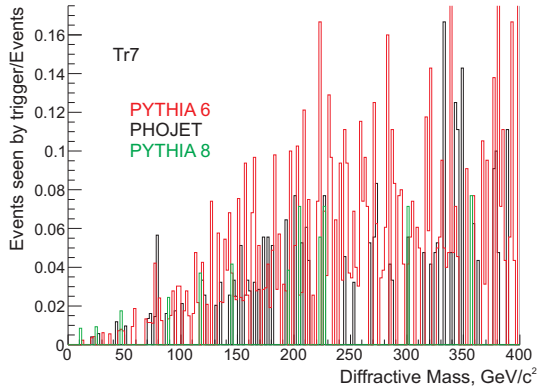

Figure 3.30: The diffractive mass acceptance of Tr7 at 7 TeV: measured / true diffractive mass distribution.

Figure 3.32 shows the Tr1 acceptance, which indicates the region of diffractive mass that is not seen by the minimum bias trigger. This shows that in the very low mass region (< 5 GeV), the V0 and SPD are not sensitive, meaning that there is very little constraint from data on this very soft diffraction.

MC provides an estimate of the efficiency of Tr1 as well as the other triggers - this inefficiency contributes to the measurement of the total number of events. The MC prediction of low mass diffraction therefore impacts on the final fit.

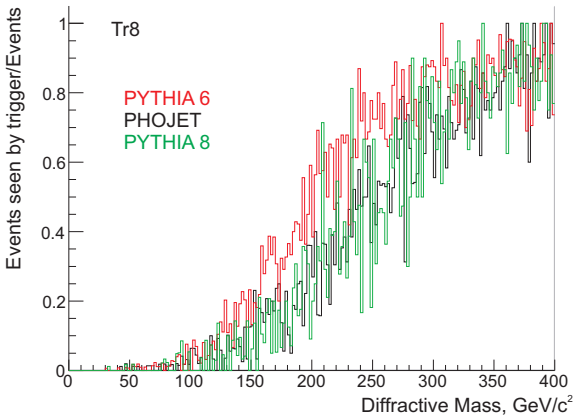

Figure 3.31: The diffractive mass acceptance of Tr8 at 7 TeV: measured / true diffractive mass distribution.

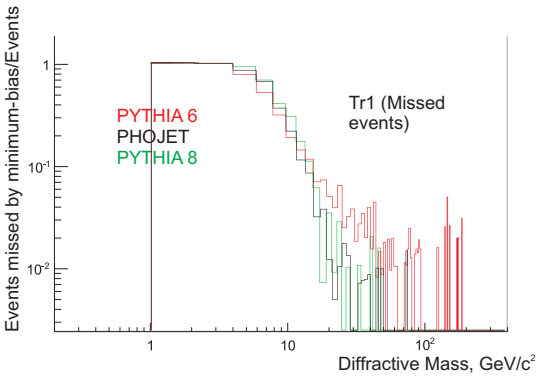

Figure 3.32: The diffractive mass acceptance of Tr1 at 7 TeV: missed / true diffractive mass distribution.

As shown in Table 3.19, by increasing the lower limit for the diffractive mass, in this case to 5 GeV, one can see how an uncertainty in this data-insensitive region affects the results.

Table 3.19: The 7 trigger fit results for 7 TeV data after setting the lower limit of diffractive mass in MC to 5 GeV: fractions of single, double and non-diffractive events (f_{SD}, f_{DD} and f_{ND} respectively), and the total number of inelastic events N^{inel} using the efficiencies from PHOJET, PYTHIA 6 and PYTHIA 8 respectively.

Efficiencies	f_{ND}	f_{SD}	f_{DD}	N^{inel}	χ^2
PHOJET	0.708±0.016	0.128±0.039	0.165±0.051	290000±5000	21
PYTHIA 6	0.745±0.009	0.18±0.04	0.076±0.045	294200±4000	22
PYTHIA 8	0.719±0.01	0.079±0.049	0.202±0.053	295500±5600	34

The breakdown of the systematic uncertainty for the fractions is shown in Table 3.20. The efficiencies that provided the best fit results (PYTHIA 6) were used for the final measurement.

Table 3.20: The estimated fractional contributions to systematic uncertainty on fractions for 7 TeV using PYTHIA 6 efficiencies (material budget uncertainty estimate was done using 900 GeV simulation as this was the only sample available).

Measurement	f_{ND}	f_{SD}	f_{DD}	N^{inel}
V0 Thresholds	0.064	0.249	0.216	0.056
Poorly reproduced ADC spectra	negl	negl	negl	0.018
Material Budget	0.008	0.085	0.143	0.004
Diffractive mass lower limit	0.035	0.214	0.49	0.04
Total systematic uncertainty	0.073	0.339	0.554	0.071

3.5.7 Evaluation of Results

The results are described for 7 triggers. Looking only at diffractive and non-diffractive event fractions, the results using different efficiencies are comparable at both energies - all favour a high

ND fraction. However, SD and DD were not distinguished well, as was already found in the MC study. The best fit came from PYTHIA 6 in both cases, and the final fractions with full errors are estimated to be, for 900 GeV:

- f_{SD} =0.201±0.086
- f_{DD} =0.077±0.052
- f_{ND} =0.722± 0.055
- N^{inel} = 351800±22800

and for 7 TeV:

- f_{SD} =0.229±0.095
- f_{DD} =0.051±0.06
- f_{ND} = 0.72±0.054
- N^{inel}=306300±22300

The main contribution to the uncertainty in N^{inel} comes from varying the low diffractive mass region. This is because our sensitivity to N^{inel} (as opposed to $N^{measured}$) comes from the model estimate of the minimum bias efficiency (ie this depends on how much data we believe we have missed). In addition, a large uncertainty on the single and double diffraction comes about in the fit as a consequence of the fact that SD and DD are poorly distinguished.

At both energies, PHOJET and PYTHIA efficiencies gave similar quality fit results, with the best fit given by the PYTHIA 6 efficiencies. Table 3.21 shows each trigger's contribution to the χ^2 at both energies. One can see that in both cases Tr2 and Tr5 contribute to quite a large extent, which may indicate a systematic effect.

Table 3.21: Contributions to the χ^2 at 900 GeV and 7 TeV for the best fits (PYTHIA 6)

Tr	χ^2: 900 GeV	χ^2: 7 TeV
2	0.96	6.05
3	0.01	0.34
4	0.13	5.3
5	1.74	4.07
6	0.48	0.32
7	0.0001	0.03
8	0.03	0.05

In the 900 GeV case the overall χ^2 is much smaller than for 7 TeV. At 900 GeV, Tr7 contributes very little to the χ^2, meaning the error on this trigger is much larger than the actual deviation of N^{Calc} from N^{Trig}.

To investigate this further, Figures 3.33 to 3.36 attempt to investigate the appropriateness of the errors in both 900 GeV and 7 TeV fits.

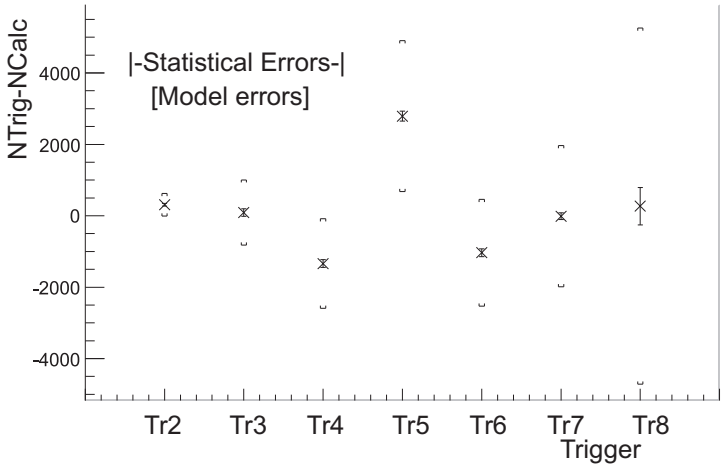

Figure 3.33: N^{Trig}-N^{Calc} from each of the 7 triggers at 900 GeV, with model and statistical errors given by square brackets and solid lines respectively.

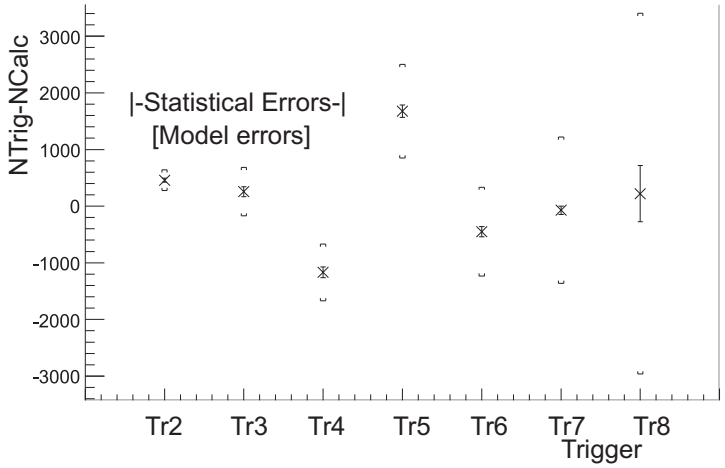

Figure 3.34: N^{Trig}-N^{Calc} from each of the 7 triggers at 7 TeV, with model and statistical errors given by square brackets and solid lines respectively.

Figure 3.33 and 3.34 show the difference N^{trig}-N^{calc} of each of the 7 triggers compared with the errors used in the χ^2 minimization - a statistical error on N^{trig} and a model error on N^{calc}.

Figures 3.35 and 3.36 show the ratio N^{Trig}/N^{Calc}, again compared with the statistical and model error on the ratio.

One can see that the errors vary with the triggers because of statistics, and because of the difference in MC efficiencies. The model uncertainty is large compared with the statistical error. It is particularly large in Tr8, where the statistics are very large, but the error on the ratio (shown in Figures 3.35 and 3.36, which account for the statistics) shows that the fractional error on this trigger is small.

It seems that the errors on some of the triggers, in the 7 TeV case, are a little small compared with the deviation. At 900 GeV they seem more appropriate.

It is likely that some of the detector effects described in the systematic uncertainty estimation are responsible. In particular, inappropriate placement of the V0 thresholds had a dramatic effect on the fit results that influenced each trigger in a different way. Also, if the material budget was

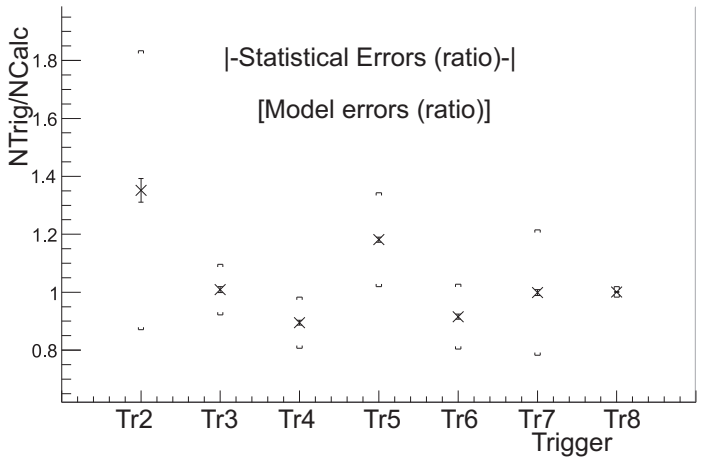

Figure 3.35: N^{Trig}/N^{Calc} from each of the 7 triggers at 900 GeV, with model and statistical errors on the ratio given by square brackets and solid lines respectively.

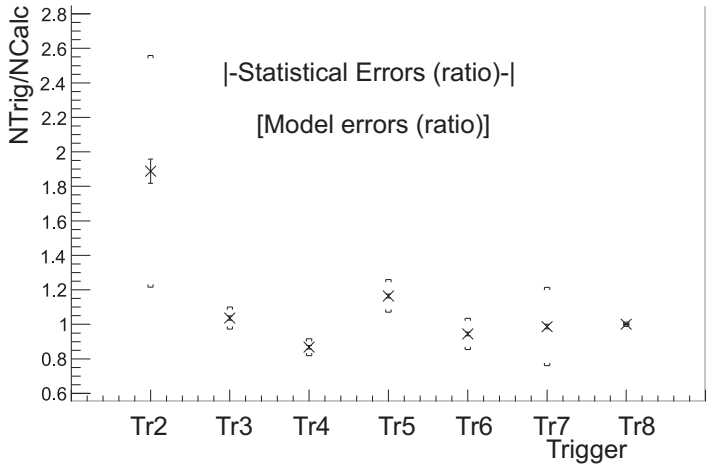

Figure 3.36: N^{Trig}/N^{Calc} from each of the 7 triggers at 7 TeV, with model and statistical errors on the ratio given by square brackets and solid lines respectively.

incorrectly described in the MC this could have a large effect on the fit. However, overall, the picture looks satisfactory.

3.6 Comparison with Other Measurements

Using the ALICE measurement for the inelastic cross-section at 7 TeV [80], we may consider the final results in terms of cross-section:

- σ_{SD} =17 ±7 mb
- σ_{DD} =3 ±4 mb
- σ_{ND} =52 ±5 mb

where here the errors from the ALICE inelastic cross-section measurement are added in quadrature, and the measured fractions are assumed independent of the inelastic cross-section for error propagation. The cross-sections can be approximately compared with the predictions in Table 1.1. However, it is worth noting that the contribution to this cross-section from events missed by minimum bias was not well constrained by the measurement - it was estimated only through MC, and influenced by uncertainty in the low-mass diffraction region. The measured N^{inel} is defined as N^{Trig}_{sum}+N^{Missed}. However, the only sensitivity to N^{Missed} comes from the model efficiencies of Tr1. It was clear from the systematic study that this trigger is sensitive to low-mass diffraction, and so the final cross-sections are model dependent and should be considered with care.

For completeness, the measured fractions have been corrected for minimum bias efficiency to obtain the fraction of ALICE-measured data. This can be found in Appendix C.

Another approach has been taken in estimating the ALICE diffractive fractions, by M. Pogoshyan [79]. This approach involves using minimum-bias data taken with the V0 and SPD, but using the tracks in the SPD and FMD to identify rapidity gaps of a certain size and region. A right arm

trigger is created, requiring no tracks in the η< -1 range, and a left arm trigger similarly requires a track-free η> 1 range. A two arm trigger can then be created requiring a rapidity gap of a certain size in the central region, which is expected to be sensitive to double-diffractive events.

The results obtained in this approach, (corrected to be fractions of the inelastic cross-section) were f_{SD}=0.202±0.034 and f_{DD}=0.113±0.029 for 900 GeV and f_{SD}=0.201±0.039 and f_{DD}=0.122±0.036 for 7 TeV, where the SD fraction is defined as being in the diffractive mass range $M_X < 200$ GeV/c^2 and the DD fraction is defined as having a gap of $\Delta\eta > 3$. These fractions are compatible with the results obtained by the author in this chapter.

However, as predicted by the MC study, it is clear that DD and SD cannot be well separated using the author's method, according to the uncertainty in the kinematics of the generators used and ambiguity of DD and SD in the measured range. The SD and DD fractions were not well distinguished in the fits, whilst the ND fraction remained fairly constant. For this reason, the results are presented as follows:

- f_D = 0.278±0.055
- f_{ND} = 0.722± 0.055

for 900 GeV, and:

- f_D = 0.28±0.054
- f_{ND} = 0.72±0.054

for 7 TeV.

ATLAS is a general, all-purpose detector designed to investigate a wide range of physics. This experiment also requires an early estimate of diffractive fractions so that systematic uncertainty can be evaluated for minimum bias distributions such as pseudorapidity density (as with ALICE).

The approach taken in [120] was to create rapidity gap triggers and establish their efficiency to select on diffractive events using MC simulation. They too were unable to distinguish SD and DD, seeing little sensitivity in the models to a change in the ratio, but obtain a diffractive fraction of the inelastic cross-section at 7 TeV of f_D=0.302±0.003±0.038 (using PYTHIA 8). The results are compatible with the ones obtained by the author.

The main goal of TOTEM is to measure the total pp cross-section at the LHC, and also to study the structure of the proton by measuring elastic events at a range of transverse momenta p_T. The detector consists of Roman pots, GEM (Gas Electron Multiplier) detectors and cathode strip chambers, placed inside the beam-pipe. It is able to identify single-diffractive and elastic events by locating intact, deflected protons in an interaction. It can also measure the luminosity of the beam. TOTEM have already measured the elastic differential cross-section in the $\mid t \mid$ range from 0.36 to 2.5 GeV^2 [127]. Diffractive measurements and results for the total cross-section are expected soon.

Chapter 4

High Multiplicity pp Collisions at LHC Energies

4.1 High Multiplicity Data

4.1.1 Interest in High Multiplicity pp Collisions

The multiplicity reach in pp collisions increases with $\sqrt{s}$, and at 14 TeV the LHC could produce up to $\mathrm{d}N/\mathrm{d}\eta \approx 60$ [128]. Bjorken's energy density relation [55] shows that a high multiplicity event can indicate that the system had high energy density;

$$\langle \varepsilon_B \rangle = \frac{1}{\tau A}\frac{\mathrm{d}E_T}{\mathrm{d}y} = \frac{1}{\tau A}\frac{\mathrm{d}N}{\mathrm{d}y}\langle m_T \rangle \tag{4.1}$$

where τ is the formation time, E_T is the total transverse energy, $\mathrm{d}N/\mathrm{d}y$ is the multiplicity per unit of rapidity, $< m_T >$ is the average transverse mass of the particles, $\sqrt{m^2 + p_T^2}$, and A is the cross-sectional area of the colliding ions. LHC pp collisions could reach energy densities of 5-10 GeV/fm^3 - comparable to Cu-Cu collisions at RHIC [129]. However, this comparison should be made with caution, as the pp systems have much smaller volume. High multiplicity can also be

caused by mini-jet formation (from semi-hard interactions), which already affects 50% of events at the Tevatron and is expected to increase with energy [130].

It is likely that minimum bias pp collisions do not produce a system in full chemical equilibrium. If a QGP was formed in the collisions, reaching full equilibrium would be more likely. However, in order for a phase transition to be possible, it is necessary that the system has (i) adequate energy density and (ii) a sufficient number of particles participating in the collision, in order to make a statistical ensemble. For example, one would not expect the collision of two fundamental particles to behave like a thermodynamic system. However, the increasing density of gluons with decreasing x in deep inelastic e-p collisions (where x is fraction of the proton's momentum that the parton carries away) at HERA [131] suggest that, at the LHC, pp collisions could involve collisions of up to ~ 15 parton pairs. This may be sufficient, in combination with large energy density, to reach the minimum requirements for a phase transition to be possible. Bjorken first suggested the idea of deconfinement in pp collisions in 1982 [37]. More recently EPOS, a multiple interaction model based on Pomeron exchanges that has a core-corona approach to A-A collisions [132], also predicts the production of 'mini-plasma' in high energy density pp collisions.

4.1.2 Measurements at High Multiplicity

Observables that are typically compared in p-p and A-A collisions may prove to be interesting in a high multiplicity sample [133]. Examples of this include:

Jet Quenching Could the presence of QGP in pp collisions result in suppression of high p_T hadrons, as Bjorken proposed [37]?

Elliptic Flow Could QGP lead to measurable collective flow in pp collisions?

Strangeness Would strangeness be enhanced in a QGP in pp collisions? Could it be enhanced in a HM hadron gas in pp collisions?

Resonance Production If chiral symmetry was partially restored in HM pp collisions, could

resonances form and decay before the system cooled and the symmetry was broken?

However, when considering these observables in pp collisions several questions arise, even when assuming the phase transitions can be produced. For example, the meaning of centrality, "number of participants" and impact parameter are no longer defined in the same way; the number of participating partons should instead be considered, and as x becomes very small this number increases. This is a difficult effect to separate from the final state multiplicity, unlike for the centrality of heavy ion collisions. For jet quenching measurements, some of the variables need to be redefined. For example, something could be constructed to replace the nuclear modification factor R_{AA} to instead consider participating partons. As described in Chapter 1, it is possible, and, in the case of pp collisions, necessary, to measure flow without defining a reaction plane. Strangeness production in A-A vs pp is thought to be governed by volume (which is limited in pp collisions [134]), and the ability of the system to reach chemical equilibrium [135]. At low x, it has recently been suggested that the volume may be effectively increased by the increased number of collisions in the system [133].

4.1.3 Obtaining a High Multiplicity Data Sample at ALICE

The ALICE experiment is well equipped to obtain and analyse high multiplicity data. This study will describe the development and implementation of a method to evaluate a suitable multiplicity trigger threshold for data-taking during early 7 TeV p-p collisions. The reach of multiplicity in pp collisions at the LHC was not known when this study began, and different Monte Carlo (MC) models (e.g. PYTHIA [67] and PHOJET [68]) showed quite different expected reach for samples of the same size. A reasonable description of the multiplicity distribution can be made using a negative binomial distribution[98], in which case the high multiplicity tail becomes exponential. An early look at LHC data with fixed running conditions gave a clearer picture, and using suitable pixel chip multiplicity thresholds could provide an exponential "projection" into the high tail of multiplicity. This led to an estimate of the potential reach over the period of a few months of

data-taking.

The SPD is capable of providing a tuneable multiplicity trigger, selecting on pixel chip multiplicity, either in the Inner and Outer layers (I+O), Inner only (I) or Outer only (O). It was possible to use this alongside minimum bias data-taking in order to provide an enhanced high-multiplicity data sample. However, choosing where to set the threshold of the trigger depended on various factors, including data-taking rate, purity of the data taken, and the enhancement of sample (how many times greater than the average multiplicity would it reach). Using multiplicity distributions from data and MC, a study was carried out in order to determine the optimal threshold for this trigger based on all of these factors.

4.1.4 Multiple Events per Bunch-Crossing: Contamination vs Rate

For μ (interactions per bunch crossing) above about 0.1, there is an important contribution to minimum bias data from more than one interaction in the same bunch crossing, known as 'pile-up'. These events cannot easily be analysed in ALICE, and have to be identified and removed from the sample. For this reason, ALICE requires a large number of bunch crossings per orbit and a small μ. The probability for n interactions follows a Poisson distribution, increasing with μ:

$$P(n;\mu) = \frac{\mu^n \exp(-\mu)}{n!} \tag{4.2}$$

Therefore by reducing μ to less than 0.1, pile-up in minimum bias events becomes manageable.

With increasing multiplicity, it becomes more likely that an event contains pile-up. The effect of pile-up events on the multiplicity distribution can be reproduced if the interaction rate is known. As seen in Figure 4.1(i), using Poisson probabilities and a MC single interaction multiplicity spectrum (b), a distribution for double (c) and triple (d) interactions can be produced, where each pile-up contribution is made up of the sum of multiple single-interaction multiplicities. The effective multiplicity distribution as seen before pile-up removal is the sum of these contributions (a). It is clear that even for reduced interaction rates, if too high a multiplicity threshold is chosen, the

sample will contain a large background, and could even contain only pile-up events. Against this, if too low a threshold is chosen, the interaction rate will be too high for a rare trigger, and may have to be downscaled, like minimum bias data. It is important to make sure the sample taken is enhanced compared with selecting high multiplicity from minimum bias events.

The creation of the pile-up distributions was carried out by first making two cumulative distributions: one for the cumulative probabilities for multiple interactions, and another for the single-interaction multiplicity shape. Random numbers were used to select each event and each multiplicity one-by-one, recreating the statistical fluctuation one would expect from real data.

In order to optimise event selection using the high multiplicity trigger, the purity (fraction of remaining single interaction events) as a function of multiplicity threshold needed to be estimated for the real multiplicity distribution. An example of such a plot for MC is shown in Figure 4.1(ii).

An iterative method, based on the interaction rate, was developed, which extracted the single interaction multiplicity shape from the full (raw) pixel chip multiplicity distribution. The method is outlined in section 4.1.5. With a few million minimum bias events, aided by an exponential fit to the high tail, an estimate of the purity as a function of multiplicity threshold could be produced quickly, indicating the real enhancement in multiplicity a trigger would provide.

Another consideration is the reduction in rate with increasing multiplicity threshold. Figure 4.13 shows the exponential drop-off in statistics with increasing multiplicity threshold (normalised to 1). This is indicated by the black curve, which can be normalised to the event rate to obtain the trigger rate for a given threshold. The red curve shows the drop-off in single-interaction statistics (through loss of purity and rate). Clearly, if the rate of a trigger is limited (which is true for rare triggers to reduce dead time) it is sensible to set the threshold to the point at which the maximum allowed data-taking rate matches the raw interaction rate (from now on referred to as 'natural rate'). This means that, provided dead time is small, all events at higher multiplicities than that threshold would be obtained. Set any higher, the acquired data sample would simply be a subset of that sample. Set any lower, the events would need to be downscaled, biasing the trigger to lower

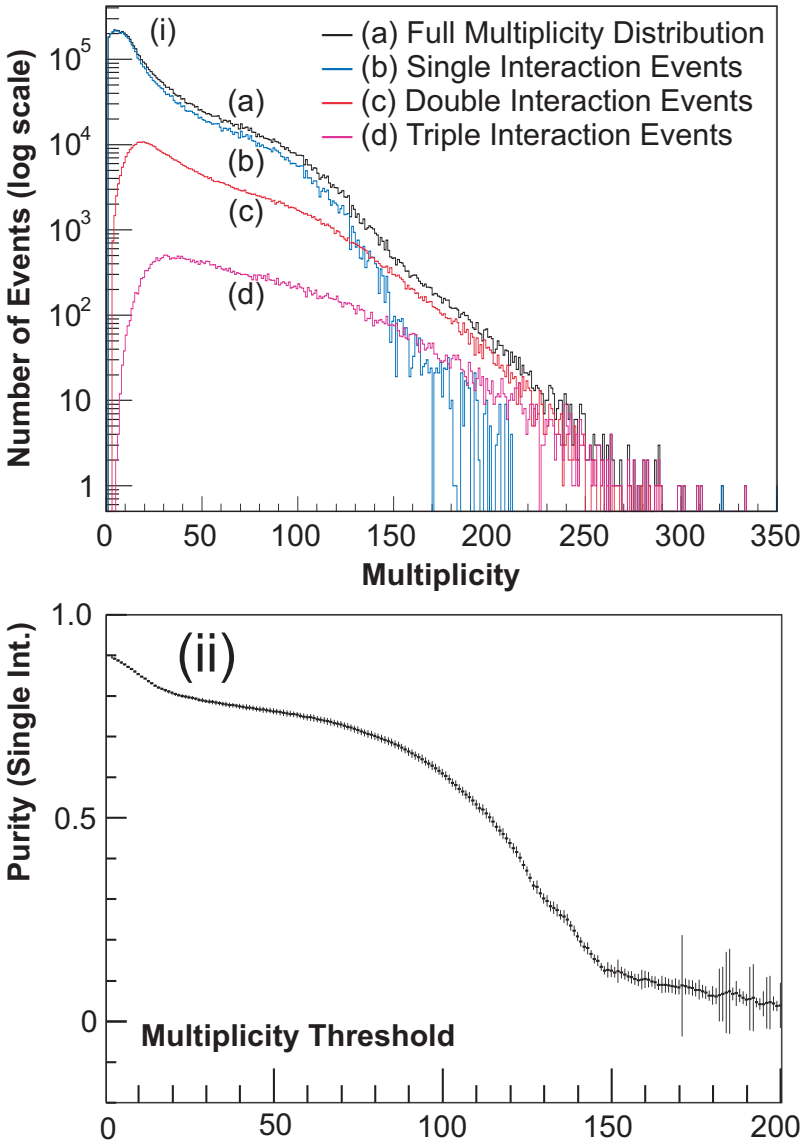

Figure 4.1: (i).Full (a) and pile-up ((c) and (d)) pixel-chip multiplicity distributions produced from single-interaction only sample (b), using PYTHIA MC with an extended exponential tail, assuming interaction rate of 0.06 ints/bc. (ii). Purity (fraction of single interactions remaining to total events remaining) as a function of the pixel-chip trigger threshold used.

multiplicities.

With both the purity information and the total event rate as a function of threshold, a suitable threshold can be chosen. Purity and threshold must remain high enough to improve upon a minimum bias sample ($<\mathrm{d}N/\mathrm{d}\eta>$ 7.5 for a minimum bias sample). A study showing these considerations for different values of μ and number of bunches/orbit N_{bc} is summarised in Figure 4.2. It was clear very early on that too high a threshold would swamp a high multiplicity trigger with pile-up events. Whilst one must make sure the purity of a sample does not dip too low, the most sensible place to set a trigger threshold is where the natural rate would be appropriate for data-taking (e.g. 10-100 Hz). With too low a μ, the natural HM rate is not high enough to make a rare trigger truly enhanced in multiplicity compared with minimum bias. However, the number of bunch crossings increases natural data-taking rate without impacting on the pile-up, so ideal conditions would be a high N_{bc} and a low μ. One can see from this picture that at μ of 0.2, the pile-up dominates the sample in a way that starts to become problematic. The ideal case would balance a high N_{bc} with a low μ to maximise purity and allow for a reasonably high multiplicity threshold with a suitable natural rate.

4.1.5 Method for Obtaining Purity as a Function of Multiplicity

The method for extracting the true purity uses only the total pixel-chip multiplicity distribution and the estimated interaction rate. The idea is to take the shape of the total multiplicity and use it as an approximation to the shape of the single multiplicity shape. Normalising the distribution appropriately, Poisson statistics can then be used to extract a "first guess" of the contributing pile-up distributions, in the same way as was carried out in the MC study. Of course these "first guesses" are incorrect - their tails are too high in reach. An example of this is shown in Figure 4.3.

However, by removing the estimated pile-up contributions from the measured full multiplicity, we get a "second guess" at the single-interaction distribution. This shape can be used to again estimate pile-up contributions, and over several iterations this eventually results in the reconstruction of the

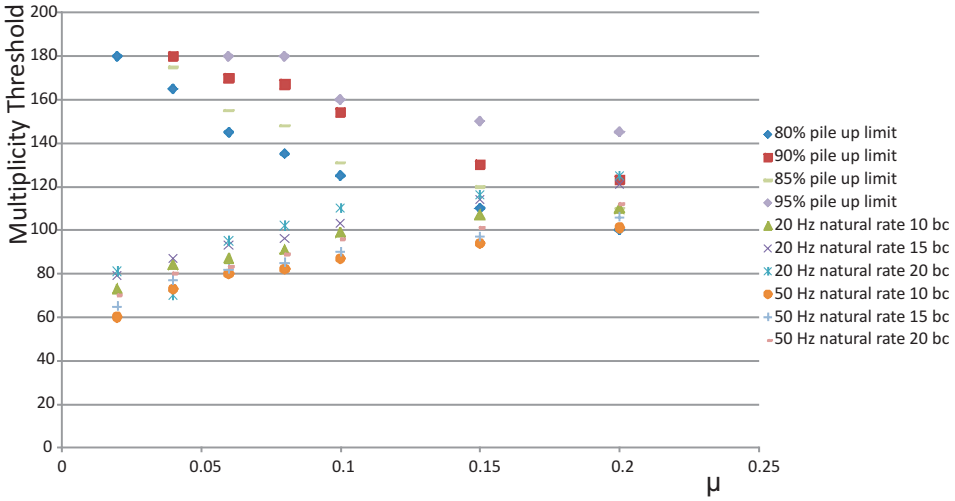

Figure 4.2: Study comparing threshold limitations for different scenarios. This uses outer pixel chip multiplicity. The first set of plotted points show the upper limit of the threshold given different limits on pile-up: to be no more than 80, 85, 90 or 95 % of the sample, given the limited number of remaining good events if this is too high. The next set of plotted points show the multiplicity threshold for a given mu and number of bunch crossings at which the natural rate is 20 or 50 Hz.

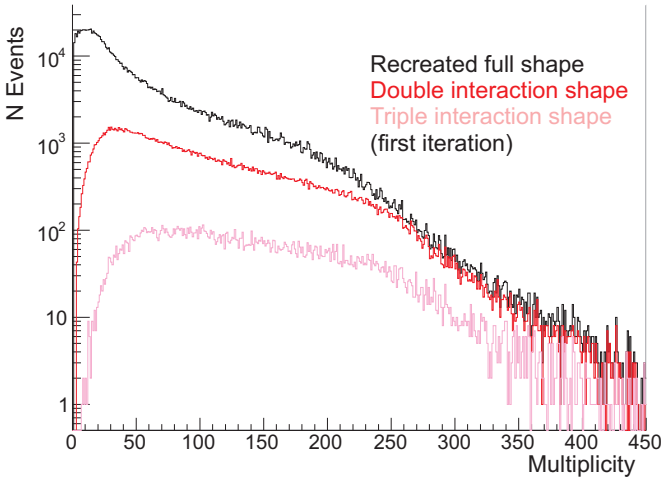

Figure 4.3: The "first guess" full and pile-up multiplicity distributions using a PYTHIA 6 "full shape" as a guess for the single interaction shape.

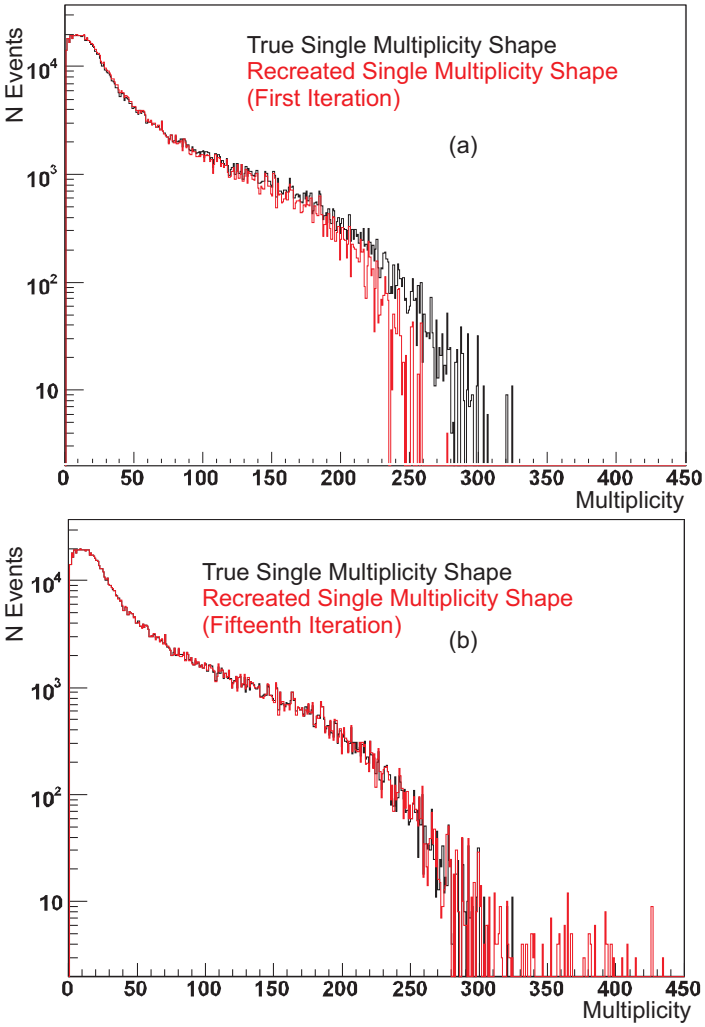

Figure 4.4: (a) The "true" and "first guess" PYTHIA 6 single interaction distributions (b) The "true" and 15th iteration PYTHIA 6 single interaction distributions

true single shape, as shown in Figure 4.4. Appendix C shows that because the pile-up is overall a smaller contribution to the total multiplicity than the single shape, this result is expected. This method may also be applied to many other shapes.

Because, as with the MC study, finite sample sizes filled with random numbers are used, the high tail can have poor statistics, making this method less effective. In order to prevent this problem, the last bin of all multiplicity distributions is set to be no less than 10 (the first bin to drop below this contains the sum of any subsequent bins with less than 10). The effect of this correction is shown in Figure 4.5. It is clear that there is excellent agreement between the two shapes.

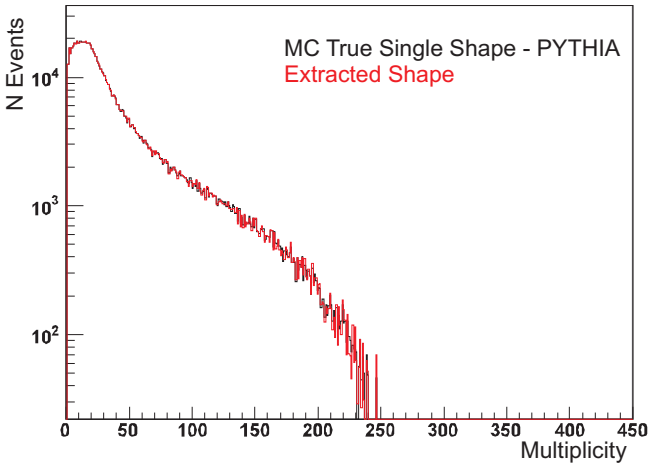

Figure 4.5: The extracted and true PYTHIA 6 single-interaction multiplicity distributions in the case of minimum bin-content of 10

Depending on μ and sample size one might see the "first guess" pile-up contributions exceed that of the measured multiplicity, leading to a negative high tail in subsequent iterations. The shape still eventually converges, and this negative part gradually becomes smaller and higher in multiplicity. However, as negative multiplicity is unphysical, a correction was put in place to remove this effect. During the creation and removal of the pile-up shapes, which was done one "interaction" at a time, each time an interaction threatened to lead to a negative multiplicity in the next iteration, it was rejected, and lower multiplicities were tried, until a physical value was found. Care was taken to ensure the probabilities were not affected by this, so that the shapes still had the correct normalisation, but there was an effective weighting of the rare, high multiplicity events to be placed

as high in multiplicity as was physical. This meant that the first guess shapes found an appropriate slope in the first iteration, making a conversion to the true shape much faster. A demonstration of this effect is shown in Figure 4.6, which shows the measured χ^2 over 15 iterations. The statistical error was used in the χ^2 calculation. Here, it took only 3 iterations to converge, compared with 7 iterations in the case where no constraint was placed on the histograms to be positive.

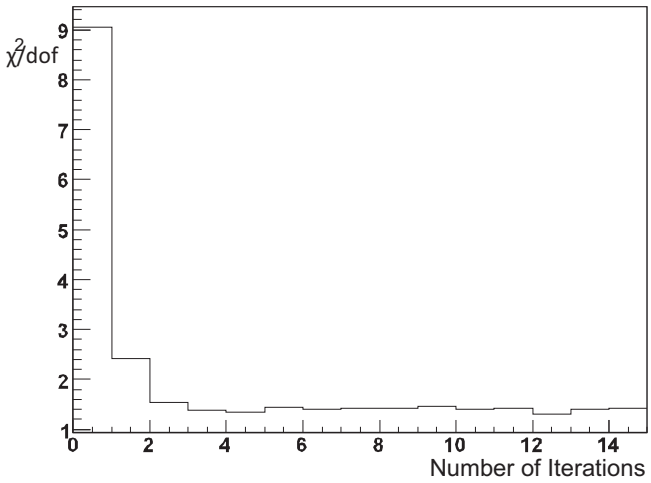

Figure 4.6: The χ^2 per degree of freedom of each of 15 iterations, looking at the difference between extracted and "true" PYTHIA 6 single-interaction distributions, in the case where pile-up shapes were forces to allow only positive values for the next iteration.

4.1.6 Offline Pile-up Removal using SPD

It is assumed for this study that pile-up can be removed offline to a very high accuracy, and that the only limitation on how much contamination can be tolerated relates to the rate of pure events obtained. The motivation for this assumption is explained below.

Multiple interactions in the same bunch crossing can be removed using offline multiple-vertex finding software [136]. During reconstruction, a primary vertex is found using information from the tracking detectors (ITS and TPC). Once one primary vertex has been found, a further iteration can be used to search for a second primary vertex. Reconstruction efficiency depends upon the multiplicity of each vertex and their separation depends on the position resolution. The software

can be tuned to require a minimum multiplicity in the second vertex, and a minimum separation between the vertices, and this should be tuned to reduce false positives (from poorly reconstructed single-interaction event primary vertices) and contamination (from missed second vertices). Two primary vertices can be distinguished with as little as 750μm separation [93] assuming both vertices can be reconstructed. The event can then be classed as pile-up and removed. Given the primary vertex distribution is Gaussian along z, one can simulate the positions of multiple vertices and plot the distribution for their separation. This is shown in Figure 4.7, using a Gaussian distribution with σ=7.5cm. By removing the 'events' with separation larger than 1mm, the remaining pile-up was reduced by a factor 10^3 (in a sample of 1 million events, less than 1000 remained).

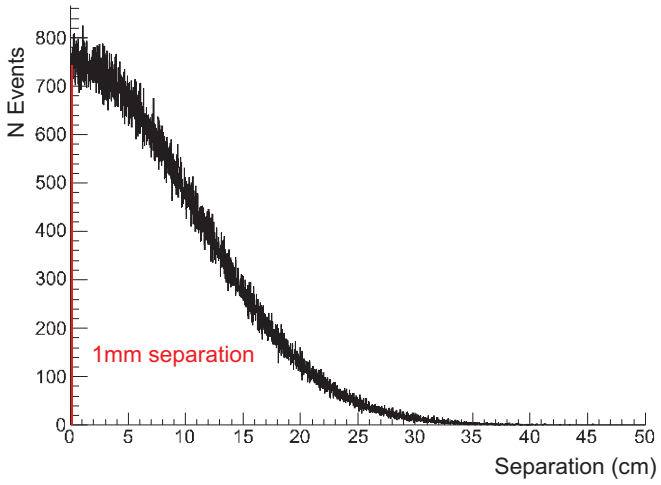

Figure 4.7: Separation of two vertices along z, given that their vertex distributions along z are Gaussian with σ of 7.5.

The efficiency and contamination of offline pile-up tagging, at the time of writing this thesis, are still under study. However, both vary with multiplicity, and at high multiplicities the efficiency is expected to be very high, as both vertices are more likely to be reconstructible. Early studies on real data [137] find optimal requirements of separation d >0.8cm and number of contributors $N_{cont}\geq$3. By comparing pile-up removed multiplicity in these conditions with the extracted single-interaction multiplicity (using the author's method) gives results consistent with 100% efficiency for multiplicity greater than 20 outer pixel chips [137]. However, accurate estimation of the efficiency

of the pile-up removal cannot be established without ALICE pile-up simulation, which, at the time of writing this thesis, did not exist.

4.1.7 Uncertainties on Purity and Corrections to the High Multiplicity Data Sample

The uncertainties and corrections for the extraction of purity are minimal due to the simplicity of the information used - the threshold is set on the number of pixel chips, so using the pixel-chip multiplicity for the study reduces required corrections on the obtained threshold. However, as conditions change from run to run, it is important to recalculate the purity for each new run. In addition to this, it is important to remove beam-gas background contributions to the multiplicity shape. As shown in Figure 4.8, beam-gas events can start to dominate the sample at high multiplicity, but the use of the V0 timing information removes this.

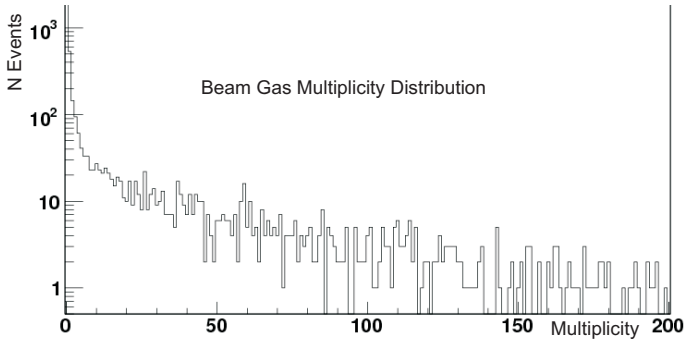

Figure 4.8: The multiplicity distribution caused by beam-gas events.

The main source of uncertainty in the extraction of the single shape is the estimation of μ. μ is measured from the CTP's L0 scalers and fluctuates depending on beam conditions. A study estimating the effect of an incorrect measurement of μ is shown in Figure 4.9. The associated error on the purity is estimated to be no greater than 10 %, given that μ is <0.2. This, however, assumes that the extraction of the single interaction shape is redone for each new run having measured μ again.

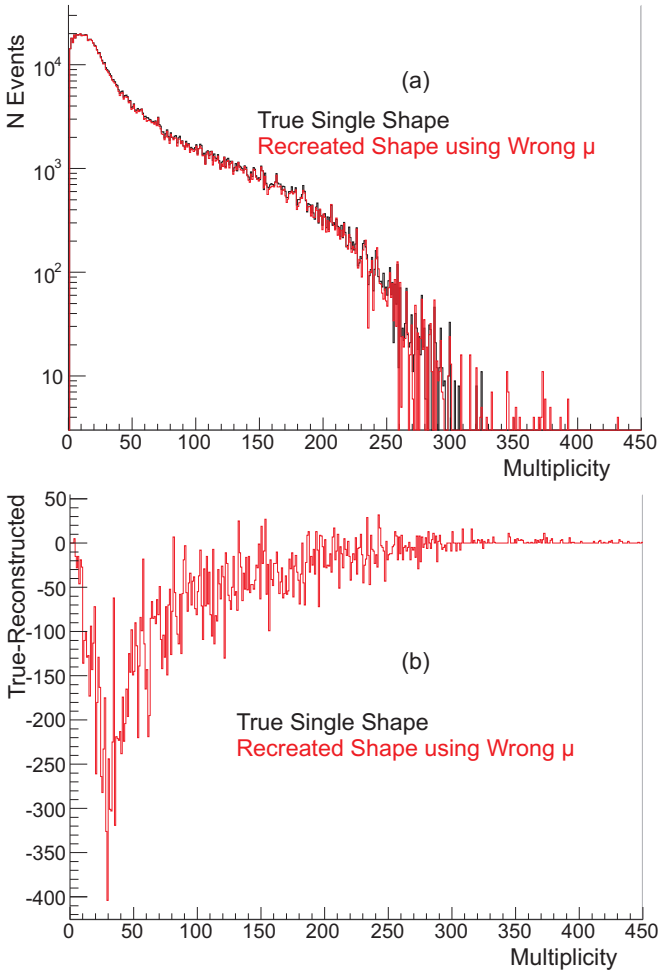

Figure 4.9: (a) PYTHIA single interaction multiplicity, created using μ of 0.2 (black), and the estimated full multiplicity distribution using a μ of 0.22 to extract the single-interaction and pile-up distributions (red). (b) Difference between PYTHIA true single interaction multiplicity and the extracted shape using μ of 0.22. The resulting χ^2 was 2.

An important point to note is that the multiplicity used is from the pixel-chips of the SPD. Each layer saturates when the multiplicity approaches the number of chips, (400 inner layer chips and 800 outer layer chips). One can see from Figure 4.10 that the inner layer pixel chip multiplicity can be linearly related to dN/dη at a pixel chip multiplicity only up to 200, whereas the outer layer can reach around 400. For this reason, outer layer pixel chip multiplicity was used for the trigger.

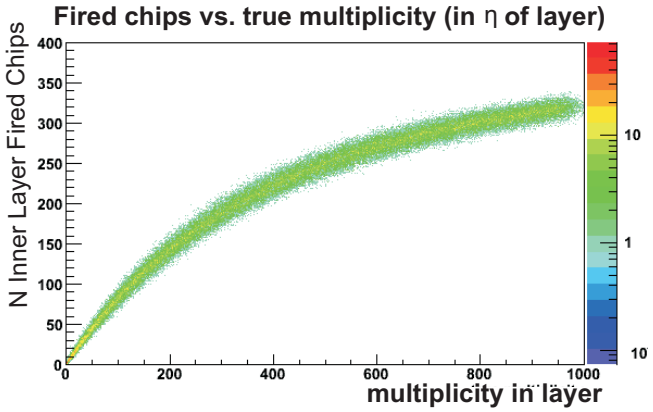

Figure 4.10: SPD pixel chip hits (inner layer) as a function of true multiplicity.

4.1.8 Purity and Proposed Threshold for 2010 using 7 TeV Data

The first use of this method came during May 2010, when the μ provided was around 0.1 and the number of bunch crossings per orbit was 8 (where each bunch orbits at a rate of just over 11kHz). μ was established using the CTP scalers, as shown in Figure 4.11. A run with μ of 0.1 was selected for study, to demonstrate how the purity as a function of multiplicity threshold could be established. The threshold was calculated given these conditions. The results are outlined below. However, during later runs, conditions became more optimal, with more bunches and a lower μ as requested (eventually averaging at 0.06), allowing for more data to be taken at high multiplicity. Section 4.2 describes a feasibility study estimating the statistics that could be achieved over a short period for strangeness studies. In fact, even more HM data than originally proposed have been obtained.

The raw pixel-chip multiplicity shape is shown in Figure 4.12, overlayed with the extracted single-

interaction shape and pile-up contributions, after 15 iterations. The drop-off of the fraction of remaining events as a function of threshold, shown in Figure 4.13, was used to calculate the rate for a given threshold. This figure also shows the single interaction fraction drop-off (red). The ratio of these provides the purity, shown in 4.14.

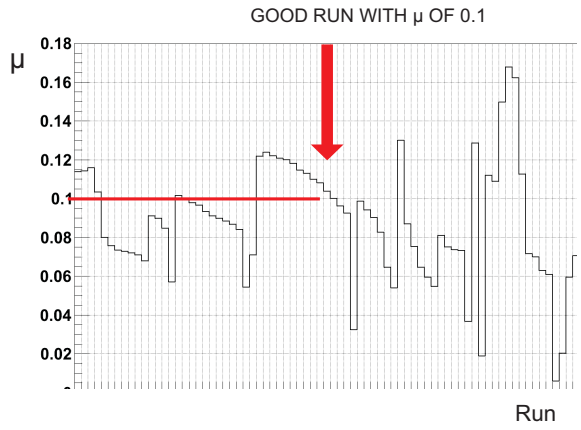

Figure 4.11: Measured interaction rate/bc, μ, taken from the CTP L0 scalers during 7 TeV p-p data-taking in 2010.

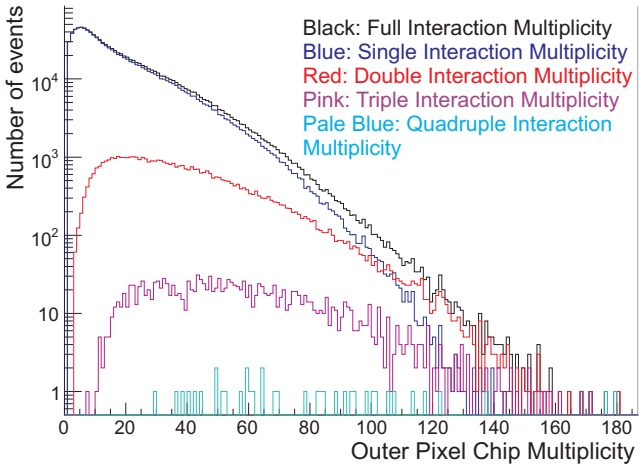

Figure 4.12: .Measured full, and extracted single and pile-up outer pixel-chip multiplicity distributions using a measured interaction rate of 0.1 ints/bc: 7 TeV p-p data 2010.

The optimal threshold was obtained by considering the rates and purity for different thresholds. The conclusion was that for these conditions, one could take data at the threshold where the rate allowed (10-100 Hz) was the naturally occurring rate of HM events, whilst still improving upon

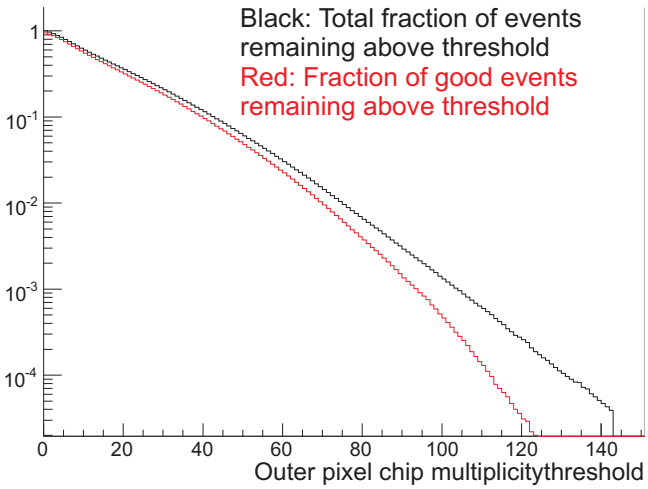

Figure 4.13: Fraction of single (red) and total (black) events remaining as a function of the pixel-chip trigger threshold used: 7 TeV p-p data 2010.

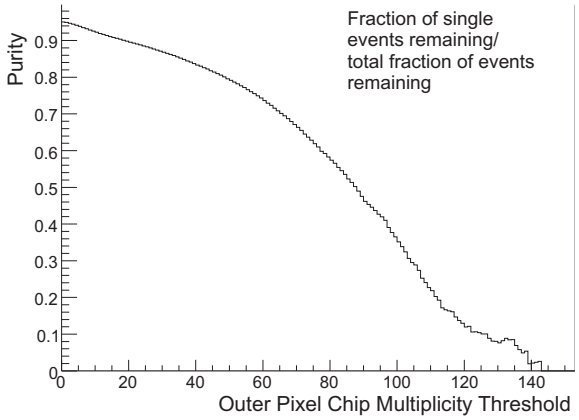

Figure 4.14: Purity (fraction of single interactions remaining to total events remaining) as a function of the pixel-chip trigger threshold used: 7 TeV p-p data 2010.

minimum bias, and achieving a purity that allowed reasonable statistics. The results are outlined in Table 4.1.

Table 4.1: Optimal High Multiplicity Thresholds for different data taking rates: Inner + Outer and Outer only pixel chip multiplicity

Rate (Hz)	Threshold: I+O	Threshold: O	Purity (%)
100	150	73	63
50	170	81	55
10	210	103	32

4.1.9 Summary

This section has shown that μ, N_{bc} and the detector's data-taking rate influence where a threshold can be placed for a rare trigger. The author's method for extracting the true single interaction shape has given a much more quantitative understanding of what conditions are optimal, and at what point conditions are unacceptable for acquiring a suitable HM data sample, via the purity and fractional rate loss graphs. It has shown that μ of greater than 0.2 causes pile-up to become problematic, and with too low N_{bc} the natural rate at high multiplicity is low compared with the maximum data-taking rate. The higher N_{bc} becomes, the more enhanced a HM trigger can be compared with minimum bias, without reducing purity. During early data-taking, the LHC suggested a set of running conditions for ALICE - μ of 0.2 and N_{bc} of 6 - and these conditions were rejected because of the results of this study. Since the run shown above, with μ of 0.1 and N_{bc} of 8, conditions for data-taking were greatly improved, guided by these quantitative predictions.

Given suitable running conditions and a sensible threshold for HM data-taking, the next consideration is whether a HM sample can probe some of the HM physics discussed within a reasonable timescale. This is difficult to quantify, but depends at least on the factor increase in multiplicity a HM sample could provide. For this study, it is taken that a factor of 5 times the mean $\mathrm{dN/d}\eta$ is required to begin to investigate the interesting HM effects.

The author conducted a study using a specific ALICE analysis - strangeness - to assess whether it was feasible to analyse events at such high multiplicity within a reasonable time frame (three months of data taking), under the assumption of fairly optimal conditions. The next section describes this study.

4.2 Strangeness in p-p collisions at ALICE

4.2.1 Strangeness: Evidence of Quark Gluon Plasma

Ratios of strange to non-strange particles in A-A collisions (e.g. at SPS [138], RHIC [139]) are enhanced compared with pp collisions. The yields in Pb-Pb collisions at the SPS and Au-Au collisions at RHIC can be described well by a grand-canonical system in equilibrium [140]. This suggests that saturation of strangeness has occurred upon hadronisation of the system [141]. One possible mechanism for this fast chemical equilibration of hadrons is that a quark gluon plasma has been formed, where strange quarks can reach equilibrium quickly - this system would produce a high abundance of strange and anti-strange pairs because of the temperature. As a grand canonical system, the medium appears to require only global strangeness conservation, and this results in the relatively easy production of strange hadrons during hadronisation.

It is also proposed that in pp collisions, strangeness production is suppressed by the limited volume of the colliding system, which requires local strangeness conservation [134], [142]. This would mean that the production of strange particles would be more suppressed with increasing strangeness content.

This approach assumes both systems are able to reach equilibrium for strangeness production. For a discussion surrounding this assumption, see Section 4.3.1.

4.2.2 High Multiplicity: Scope for Strangeness at ALICE

A feasibility study was conducted to establish the early data-taking potential for high-multiplicity strangeness measurements. This included the relative yields of π/K/p, yields of Λ and $\overline{\Lambda}$, and eventually Ξ and $\overline{\Xi}$, in minimum-bias data and for high multiplicity events taken with a proposed trigger. For reasons outlined in the next section, the ϕ yield is also of great interest in these data, and was considered in the same feasibility study.

The strategy was based on analysing a sample collected during the first three months of data-taking. This would provide a first look at high multiplicity. The required statistics for each analysis needed to be established to verify that a HM trigger would be capable of obtaining such a sample. The ideal way to estimate this would be to analyse simulated HM data. However, at the time of writing this thesis, enhanced HM simulated data for the ALICE detector has not been produced. Estimates were therefore made by projecting minimum bias samples.

The first step for this was to establish the minimum required statistics for minimum-bias study, using 7 TeV MC data (except for Λ and Ξ, where only 10 TeV MC data was available). These numbers were provided by the strangeness working groups using standard analysis code. Estimates were based on requiring a significance of 10 and a statistical error of less than 10% for bins below a p_T of 3.5 GeV/c. It was assumed only TPC PID information would be available for the analyses (3 σ). The results are given in the first part of Table 4.2.

The next step, undertaken by the author, was to consider the scaling of the required statistics with multiplicity. This is described in detail in the next section. It was assumed that multiplicities of at least $5\times <$ dN/d$\eta >$ would be needed for the high multiplicity sample to begin to investigate physics effects. The results of this are shown in the second part of Table 4.2.

Following this, the next step was to establish how high in multiplicity one could reach (expressed as a threshold), during 3 months of data-taking with the appropriate use of a HM trigger, and still obtain the statistics required, given realistic assumptions regarding running conditions. The

Table 4.2: The estimated numbers of events needed for each analysis.

	π/K/p	$\Lambda/\overline{\Lambda}$	ϕ	$\Xi/\overline{\Xi}$
N (10^3 Events) - Minimum Bias (MB)	10	200	300	1500
N (10^3 Events) High Multiplicity (HM)	5	50	300	500

results of this are shown in Table 4.3.

Significance: Scaling to a HM Sample

For each case, approximate scaling of significance with $\mathrm{d}N/\mathrm{d}\eta$ and number of events was considered in order to obtain the required sample, as shown in Table 4.2.

The following assumptions are made:

A significance of 10 is enough Studies with MC conducted by the strangeness working groups have established the statistics required for this to be true in MB.

No strangeness enhancement This means that for final state charged particles, the ratio of signal to background, $\frac{S}{B}$ does not change with multiplicity

Scaling of significance with multiplicity can be approximated The analysis method will influence the scaling of background, but signal should increase linearly as with multiplicity, provided there is no strangeness enhancement

The significance of a sample describes how much the signal of the desired particle, for example the number of kaons measured, exceeds the background:

$$\text{Significance} = \frac{S}{\sqrt{S+B}} \tag{4.3}$$

Consider a sample of N minimum bias events, providing a suitable significance for a given measurement. For this study, it is useful to approximate the statistics required for an equivalent

significance at high multiplicity;

$$\frac{S_1}{\sqrt{S_1 + B_1}} = \frac{S_2}{\sqrt{S_2 + B_2}} \tag{4.4}$$

where S_1 is the signal in minimum bias data and S_2 is the signal of our high multiplicity sample.

Charged particles

Based on the assumption that for final state particles such as kaons, $\frac{S}{B}$ is constant with increasing multiplicity, (signal and background both increase linearly, as with an increase in statistics), one can describe the expected significance of the new sample as;

$$\frac{S_2}{\sqrt{S_2 + B_2}} = \frac{\sqrt{yCS_1}}{\sqrt{1 + x}} \tag{4.5}$$

where C is the factor increase in multiplicity, y is the factor change in statistics, and x is the ratio $\frac{B_1}{S_1}$ of the minimum-bias sample. Here, it is assumed that $S_2{=}yCS_1$ and $B_2{=}yCB_1$. One can easily show from this that for the same significance increasing the multiplicity reduces the required sample size;

$$y_{\text{ideal}} = \frac{1}{C} \tag{4.6}$$

It was estimated that at high multiplicity, for significance of 10 (where kaons and protons are S and pions are B), only a few thousand events would be required compared with 10,000 minimum-bias events, with S/B of 3.3.

Resonances

In comparison, when measuring short-lived particles such as ϕ using the invariant mass method (as outlined in Section 4.3.3), the combinatorial background of the decay products (for example, kaon pairs) increases as the square of C. This means $\frac{S}{B}$ scales as $\frac{1}{C}$ and $B_2{=}yC^2B_1$, giving;

$$\frac{S_2}{\sqrt{S_2 + B_2}} = \frac{\sqrt{yCS_1}}{\sqrt{1 + Cx}} \tag{4.7}$$

This means that it is no longer clear whether increasing multiplicity reduces the required sample size;

$$y_{\text{ideal}} = \frac{1 + Cx}{C(1 + x)} \tag{4.8}$$

It was estimated that to achieve a significance of 10 for the ϕ analysis, with limited PID, 300,000 events were required - just as in the minimum bias case. Here, S/B is 0.3.

V0s

For Λ and Ξ production, because their vertices are reconstructed, it is expected that the background scaling can be reduced, and that y can approximate to Equation 4.6. It was estimated that to achieve significance of 10, for Λ only 50,000 HM events were required, with resulting S/B of 5, and for Ξ only around 500,000 events were required, with a resulting S/B of 3.3.

Estimated Reach in Multiplicity for Strangeness

Whilst in some cases less events are required for a high multiplicity study than for minimum-bias, an increase in multiplicity leads to an exponential decrease in statistics and an increase in contamination from pile-up, as explained in the previous section. For this reason, a preliminary study was conducted to estimate how high a multiplicity trigger threshold could be set whilst still achieving the required statistics shown above. A realistic early (first three months) running scenario for the LHC at 7 TeV energy for ALICE pp collisions was assumed for this study (assuming accelerator efficiency of 300,000 seconds per month, [143]). Whilst the run studied in Section 4.1 had less than ideal conditions, there were many runs following it with conditions similar to, and even better than, those assumed here. The interaction rate was assumed to be 0.06 interactions/bc, with 24 bunches. It was expected that 70% of the triggering time would be dedicated to minimum-bias event selection (1 kHz). Within the remaining 30%, other rare triggers would be used, and the total rate for rare triggers must not exceed 100Hz (in order to keep deadtime to a minimum). For this study, it was assumed that other rare triggers would share this rate, and a rate of 10Hz

Table 4.3: For each analysis, estimated statistics required for the high multiplicity samples; given 3 months of data-taking, the corresponding maximum pixel chip multiplicity threshold (I+O) achievable whilst still obtaining those statistics; natural rate using each threshold; minimum $\mathrm{d}N/\mathrm{d}\eta$ of the resulting sample; factor increase in $<\mathrm{d}N/\mathrm{d}\eta>$ compared to minimum bias data.

	π/K/p	$\Lambda/\overline{\Lambda}$	ϕ	$\Xi/\overline{\Xi}$
N (10^3 Events)	5	50	300	500
Max. Threshold (at least 5% pure)	255	236	208	199
Rate (Hz)	1	2.4	7.2	10.6 (Max.)
Min. $\mathrm{d}N/\mathrm{d}\eta$	64	59	52	50
Factor $\times<\mathrm{d}N/\mathrm{d}\eta>$	8.5	7.8	6.9	6.6

would be maximum. In reality, HM was the only rare trigger used, so this picture was pessimistic by an order of magnitude in data-taking rates. It was also assumed that a purity of at least 5% would keep contamination at a safe level. This has since been supported by MC studies carried out at Birmingham University [137]. PYTHIA MC simulation was used to generate the minimum bias distribution.

Table 4.3 shows the maximum pixel chip multiplicity threshold and corresponding factor increase in $< \mathrm{d}N/\mathrm{d}\eta >$ (assumed to be 7.5 for a minimum bias sample) for a trigger threshold in order to obtain the yields given in Table 4.2 required for a first analysis at high multiplicity. In reality, as described in Section 4.1, the threshold for data taking will be set such that the natural rate matches the maximum rare trigger data-taking rate. As can be seen from the rates in Table 4.2, all of the samples can be taken with a 10.5 Hz trigger. This means that even in the most statistically demanding analysis, in a few months a suitable sample of events of almost $7\times< \mathrm{d}N/\mathrm{d}\eta >$ can be obtained. After a full year of running, a sample with appropriately high $< \mathrm{d}N/\mathrm{d}\eta >$ or statistics can be acquired based on what is found.

4.2.3 Summary

The estimation of required statistics at HM, whilst only approximate, allowed for a quantitative investigation of the prospects of using a HM trigger. From Table 4.3 we can see that, given good running conditions, reasonable statistics at very high multiplicity ($6.6\times < \mathrm{d}N/\mathrm{d}\eta >$) can be acquired in a short period of time for all of the strangeness analyses considered.

Data-taking from pp collisions at the LHC at 900 GeV began in November 2009 and the results of the minimum bias strangeness analyses at 900 GeV can be found in [144] and [145]. 7 TeV data-taking began in March 2010, and high-multiplicity data were first taken in May 2010 and continued for several months. Despite the conditions of the very early 7 TeV data (as shown in Section 4.1), the majority of the HM events were taken under similar conditions to those assumed in the study (μ of 0.04 to 0.08, N_{bc} from 22 to 36). In addition to this, no other rare triggers were used during the 2010 7 TeV pp run, so a data-taking rate of 100 Hz was possible. More than 16 million HM events were acquired. Even after background removal this is believed to be ample statistics for the studies described.

The estimation of required statistics for reasonable analyses came before 7 TeV data were available, and instead relied upon MC. The assumption that TPC PID was available had a reasonably large influence on the estimations. In particular, the ϕ required a significance of 10 for suitable analysis, and although it has been shown to be possible to analyse the data with no PID, much less statistics were required given the TPC PID could be used. For an early HM analysis of the ϕ, PID was thought to be essential. The next section looks at the influence of TPC PID on the significance of the ϕ using real minimum bias data.

4.3 Outlook for HM Strangeness: The $\phi(1020) \rightarrow K^+K^-$ Channel

4.3.1 The ϕ as a Probe of Phase Transitions

Resonances in Chiral Symmetry Restoration

Resonances can have short enough formation times to be produced in a QGP [146]. Short-lived resonances can decay during different stages of the medium's evolution. Within the plasma, they may experience shifts in mass and width, caused by partial chiral symmetry restoration [147], [148]. Those that decay within the plasma are sensitive to any mass and width effects, and reconstructing their decay products could identify these. Leptonic decay products do not interact with the plasma, making them ideal for studying these early system effects, whilst hadronic ones may be dissolved or rescattered, and the resonance may be regenerated and decay again. Yields of resonances decaying inside the medium to hadrons therefore provide information about the later stages of evolution of the fireball, as the measurement largely depends on final state effects.

The $\rho(770)$, for example, is a copiously produced resonance with a width of about 150 MeV i.e. a lifetime of the order of 1 fm/c [7]. There is evidence for mass shift effects at lower energies [149]. Most ρs produced in Pb-Pb collisions at ALICE are therefore expected to decay within the fireball, which leaves them very susceptible to final state effects. It has a fairly large width and is one of several resonances decaying to the $\pi^+\pi^-$ spectrum, which makes precise mass and width measurements difficult. It is therefore very important to reconstruct the ρ in simulated Pb-Pb collisions, to understand fully any systematic effects not relating to the QGP.

In contrast, the $\phi(1020)$ is an $s\bar{s}$ resonance with a narrow width ($\Gamma\sim$4 MeV) [7]. Its production in pp interactions gives information about the strangeness content of the nucleon. In Pb-Pb collisions, the ϕ lifetime (τ=44 fm/c) indicates that most ϕs decay outside the fireball, which makes them less susceptible to final state effects. This means that meaningful measurements can come from

its dominant decay channel, $\phi \rightarrow K^+K^-$. Because the ϕ is made up of strange and anti-strange quarks, in addition to its mass and width giving valuable information (its mass being likely to shift in the event of partial chiral symmetry restoration), its yield holds vital information alongside an early measurement of strangeness enhancement [150].

The ϕ in the QGP

Enhancement of the ϕ meson in A-A with respect to pp collisions has been measured [30], [31] and is similar to that of a doubly-strange particle. This cannot be explained by canonical suppression, because the ϕ has a net strangeness of zero, and therefore according to the statistical model, should not be inhibited by volume as it does not violate local strangeness conservation [134], [142].

The γ_s factor [135] - which describes the fraction of s and $\overline{s}$ quarks produced with respect to saturation - is unity in the case where the system reaches equilibrium, and this is the assumption in a thermodynamic picture. The γ_s factor affects strange and anti-strange quarks equally, and γ_s of non-unity would be needed to help describe suppression of the ϕ in pp with respect to A-A collisions in this model [151], [152].

So far here the mechanisms by which ϕ resonances would be produced has not been considered. Because a colourless state cannot be formed from a single gluon, interactions of ϕ with non-strange particles in a non-QGP environment is suppressed heavily. This is known as OZI suppression [153], [154], [155]. However, an abundance of s$\overline{s}$ pairs in a QGP, and the potential reduction of the ϕ mass in the case of partial chiral symmetry restoration, would lift this suppression and allow an enhancement of ϕ with respect to p-p collisions [156].

The ϕ in HM pp Collisions

The study of ϕ in HM proton-proton collisions is interesting for several reasons. If a QGP could form in pp collisions, chemical equilibrium would be more quickly reached. Therefore, if γ_s is not

unity in minimum bias pp collisions, it may be larger in HM collisions. If this is the cause of the enhancement of ϕ in heavy ions, and a QGP is formed in HM pp, one would expect to see enhancement in these events with respect to minimum bias pp events. The volume of the collision is small, so if enhancement was seen, it could not be explained by canonical suppression without imposing some "effective volume".

The ϕ is also interesting for probing chiral symmetry restoration in HM pp collisions. Whilst a ϕ mass shift from partial chiral symmetry restoration would be relatively small, its narrow width means this effect would be likely to show up clearly. As discussed in Section 4.3.3, which looks at ϕ production in 7 TeV minimum bias pp data, with reasonable significance the ϕ mass can be measured accurately even with limited (or no) PID.

4.3.2 Requirements for Measuring ϕ in HM pp Collisions

The ALICE experiment allows the study of both leptonic and hadronic decay modes of resonances. The narrow width of the ϕ allows its signal in pp interactions to be detected easily above large backgrounds with limited statistics. For this reason, the ϕ can even be considered for early study, before the PID system has been fully calibrated. The ϕ decays predominantly to K^+K^-, and is measured using an invariant mass distribution, as outlined in section 4.3.3. Since the feasibility studies of Section 4.2 were carried out, large samples of HM events have been acquired, far exceeding those required for a good analysis of the ϕ.

However, in order to conduct a study of the ϕ in HM vs minimum bias events, there are several other requirements and considerations:

Yield in minimum bias data The $\phi \rightarrow K^+K^-$ is measured in 7 TeV MB data (with and without TPC PID) in section 4.3.3. MC must be used to correct this to obtain the total ϕ yield, as recently shown in [157].

Yield in HM The same analysis must be done for high multiplicity data. This requires:

HM MC High multiplicity MC simulated and GEANT-reconstructed data, with which bias and efficiency of the trigger can be established, and raw yields can be corrected. If this was carried out using MB simulated data, the data sample would take far too long to produce. One method for production would be to reject events on multiplicity at the generator level, reconstructing only the events which have high multiplicity. This may be especially interesting in EPOS [132], where high multiplicity pp interactions can produce mini-plasmas

Pile-up MC Simulated pile-up events, with which the efficiency of the pile-up removal can be established

Pile-up Removal The offline pile-up removal needs to be optimised based on efficiency and used on the data

Definition of Multiplicity A consistent standard definition of what multiplicity means is essential. Firstly this requires deciding upon a technical definition of what constitutes a track, as various possibilities exist, using different detectors, numbers of clusters and acceptance ranges.

Definition of Multiplicity: part 2 Once multiplicity is corrected in MC, it then becomes necessary to consider whether the signal itself should be counted as part of a charged particle multiplicity.

Multiplicity vs Signal It must be checked that the MB and HM samples match up when looking at the yields as a function of multiplicity.

Physics Considerations It was assumed in section 4.2 that the sample may begin to probe the effects considered, given a multiplicity enhancement of 5 times the mean multiplicity. However, it remains to be considered how much of the high multiplicity sample actually contained high energy densities, as 'mini-jet' formation is likely at the LHC. In order to quantify effectively the thermodynamic effects of high energy density events, the contribution to the HM sample from jet-like events needs to be evaluated in some way.

The next section shows the analysis of the ϕ in a K^+K^- invariant mass spectrum, using 7 TeV minimum bias data. However, at the time of writing this thesis, no simulations of HM events or pile-up were available. These are required in order to analyse the ϕ at HM, and indeed will be crucial for any HM analysis.

4.3.3 Measuring ϕ in K^+K^- Invariant Mass Spectrum

A MC study from 2010 [158] demonstrated the possibility of measuring the ϕ before detector PID was available. The cited study looked at achievable significance above p_T of 1 GeV/c using around 4 million p-p events. The events were simulated using PYTHIA 6 and no PID information was used. The following measurement uses around 14 million 7 TeV p-p events to support this study and demonstrate the very positive outlook for High Multiplicity analysis.

An invariant mass distribution is created by first selecting final-state charged particles. In this case, we are interested in the decay of a ϕ to two charged kaons, K^+ and K^-. The charged particles have a measured momentum and can be assigned the kaon mass. In pairing each negative particle to every positive particle in that event and calculating the invariant mass of the pairs, those pairs from a two-body decay to kaons (ie $\phi \rightarrow K^+ K^-$) show a peak at the mass of the decayed particle (in this case around 1020 MeV) above a continuum of unconnected particle pair invariant masses (proportional to the square of the number of particles). Once this background has been removed, the remaining peak of ϕ is fit in order to obtain the mass and width. In this study, a Breit Wigner fit is used. This is a continuous probability distribution given by:

$$\frac{dN}{dm} = A \times \frac{\Gamma}{(m - m_0)^2 + \frac{\Gamma^2}{4}} \tag{4.9}$$

Here, m_0 is the mass of the resonance, A is the amplitude of the fit and Γ is the width.

Background Removal Methods

A "like-sign" background subtraction method can sometimes be used to remove this continuum. This means approximating the shape of the continuum by calculating the invariant mass of all negative pairs and all positive pairs, and combining the two. This can be done in two ways: either simply summing the two distributions and normalising to the original invariant mass shape, known as the "sum like-sign method", or taking twice the square root of the product of the two shapes, known as the "product like-sign method". However, when using data quality cuts to improve significance, the like-sign background shape does not always reproduce the continuous background. An alternative approach can be to do "event mixing", where the invariant mass of particles from different events is used to reproduce the background. In principle this should better reproduce the average continuum, but only for events with, for example, similar multiplicity. This can make event-mixing more tricky.

Another approach, used in the ALICE ϕ analysis at 900 GeV [144], is to fit a polynomial to the background. In this study, a Granet function [159] is used:

$$\alpha(m - m_{thresh})^{b_1} \exp\left(-(b_2 m + b_3 m^2)\right) \tag{4.10}$$

where the size α and parameters b_1, b_2 and b_3 are free, and m_{thresh} is the lower mass limit (twice the kaon mass).

Particle Identification with TPC

Limited PID from the TPC was available from the early stages of pp running, so the early ϕ analyses could achieve a high significance with less events (the invariant mass distribution contains less continuous background from, e.g. misidentified pions). A study was carried out using limited TPC information to investigate how this improved significance.

Figure 4.15(a) shows the Bethe Bloch distribution from the TPC in a 7 TeV p-p data sample. In Figure 4.15(b) a loose cut is applied, around the kaon part of the TPC Bethe Bloch distribution (dE/dx vs momentum), of 3 σ for momenta above 0.35 GeV/c and 5 σ below. As shown in Table 4.4, this improves the significance at low p_T compared with the "no PID" case.

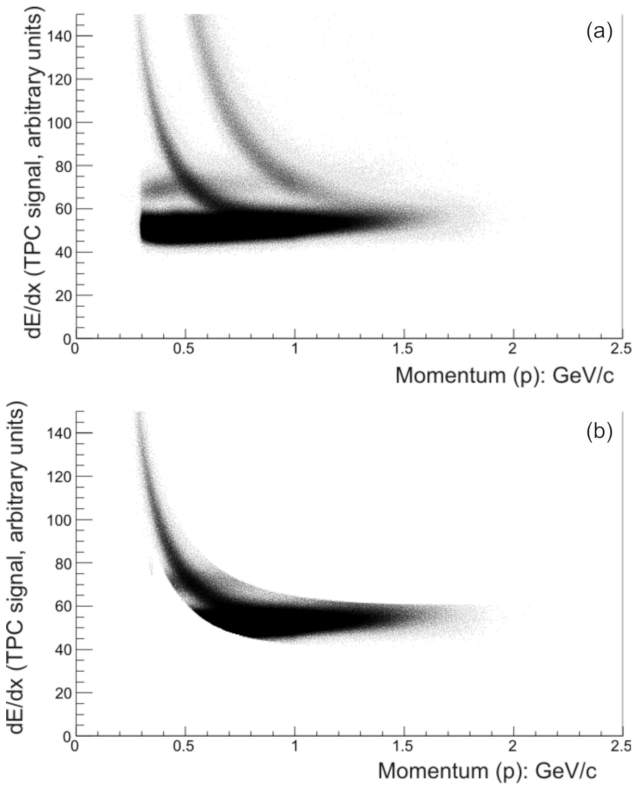

Figure 4.15: (a) The Bethe-Bloch distribution for 3×10^6 7 TeV p-p events using the TPC; (b) A 3σ cut on the K mass.

ϕ: Cuts and Corrections

Tracks were reconstructed using the TPC and ITS. This involves locating charge "clusters" for each track, where it interacts with the detector (e.g. in pads/silicon sensors). In the SPD there are a maximum of two clusters for each track. For each track at least 1 SPD "cluster" and 70 TPC clusters were required, with a maximum χ^2 of 4 required for each SPD cluster. This ensured the quality of the tracks and a well reconstructed primary vertex.

The ϕ is so shortlived that its decay products appear to come from the primary vertex. For this reason, a cut on the distance of closest approach (DCA) of the track to the vertex was made, of 5 mm in x and y, and 3 cm in z.

The rapidity Y of the invariant mass pair of the particles was calculated and a cut of 0.5 was made, so that the range of ϕ measured was well defined.

Results

Figures 4.16, 4.17 and 4.18 show the K^+ K^- invariant mass spectrum for a 7 TeV data sample of 14×10^6 events, with 1 GeV/c $< p_T <$ 3 GeV/c (no PID), 0.3 GeV/c $< p_T <$ 1 GeV/c (no PID) and 0.3 GeV/c $< p_T <$ 1 GeV/c using limited TPC PID, respectively. Each one shows the fit to the ϕ peak using a BW and to the background using a Granet function.

Table 4.4 shows the measured significance for high p_T (above 1 GeV/c) and low p_T (0.3 - 1 GeV/c) without PID. This demonstrates that a reasonable significance can be achieved in pp interactions with no PID. It also shows limited PID improved significance (calculated with the reduced background after PID).

Table 4.4: Measured Masses, widths, signal to background ratios and significance for reconstructed ϕ mesons for low (with and without PID) and high (without PID) p_T.

PID	p_T (GeV/c)	Mass (GeV)	Width (GeV)	S/B	S/$\sqrt{S+B}$	χ^2
None	0.3≤p_T≤1	1.019±0.0002	0.0049±0.0008	0.0095	9.367	9
None	1≤p_T≤3	1.0196±0.0002	0.0045±0.0008	0.059	9.398	9
TPC PID	0.3≤p_T≤1	1.0191±0.0002	0.0055±0.0007	0.0323	13.582	10

Once TOF PID is available alongside TPC information, the improvement of significance can be achieved at higher momenta. An early look at the minimum bias analysis of the ϕ can be found in [157].

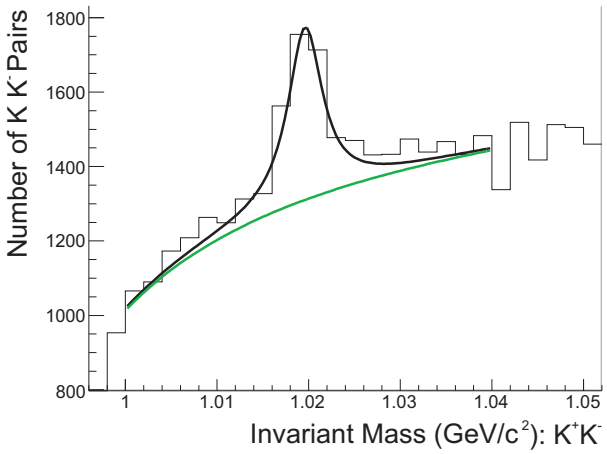

Figure 4.16: The "no PID" K^+K^- invariant mass spectrum for 14×10^6 7 TeV p-p events with $1 < p_T < 3$ GeV/c, showing the ϕ peak, a Breit Wigner fit to the peak and a Granet fit to the background.

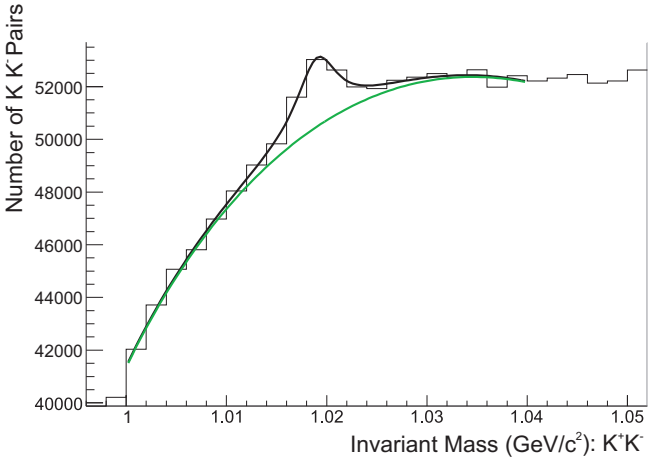

Figure 4.17: The "no PID" K^+K^- invariant mass spectrum for 14×10^6 7 TeV p-p events with $0.3 < p_T < 1$ GeV/c, showing the ϕ peak, a Breit Wigner fit to the peak and a Granet fit to the background.

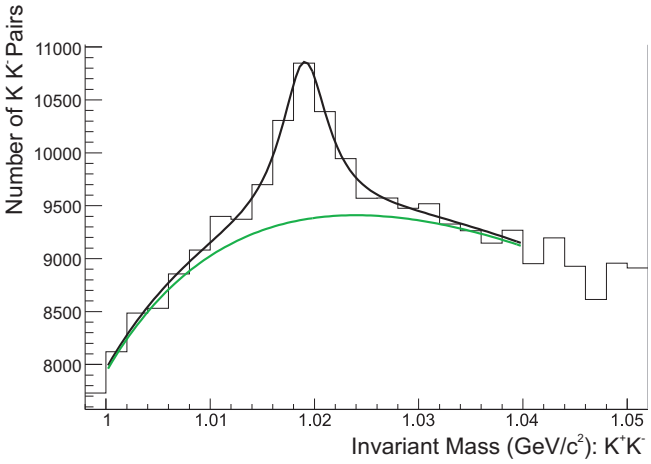

Figure 4.18: The limited TPC PID K^+K^- invariant mass spectrum for 14×10^6 7 TeV p-p events with 0.3 $< p_T <$ 1 GeV/c, showing the ϕ peak, a Breit Wigner fit to the peak and a Granet fit to the background.

4.3.4 HM ϕ Analysis: Summary

At the time of writing this thesis, the outlook is bright for the high multiplicity ϕ analysis, and other analyses using HM data. However, various requirements remain to be met, and considerations remain to be decided upon.

Crucially, MC simulation enhanced with high multiplicity events is not available, and pile-up simulation still does not exist. Without these, various efficiencies and corrections cannot be evaluated in HM data, and so the analysis of the ϕ, as well as other HM analyses, remains on hold. One of the main reasons for this is priority: once Pb-Pb collisions began, ALICE resources were focused on heavy ion studies.

In addition to this, other, less straightforward considerations remain under discussion, such as the approach to be taken regarding events containing high p_T hadrons, and how to treat the definition of multiplicity.

The timeline of the author's PhD drew to a close before strangeness analyses were complete and before HM data could be analysed. However, the outcomes of this field are enthusiastically anticipated.

Chapter 5

Conclusions

5.1 Diffraction

The author devised a method to estimate the contribution of diffractive events to the inelastic cross-section. The method involved using a series of independent triggers, using the ALICE V0, SPD and ZDC detectors. Minimum bias data were taken using the SPD and V0 and a modified version of the author's method, using subsets of the minimum bias trigger, was used to obtain the fractions. The final diffractive fractions are measured to be:

- f_{SD} =0.201±0.086
- f_{DD} =0.077±0.052
- f_{ND} =0.722± 0.055
- N^{inel} = 351800±22800

for 900 GeV, and:

- f_{SD} =0.229±0.095

- f_{DD} =0.051±0.06
- f_{ND} = 0.72±0.054
- N^{inel}=306300±22300

for 7 TeV. The results are compatible with ATLAS [120] and ALICE [79] results.

Double diffraction and single diffraction were not well distinguished. The reasons for this were alluded to in the MC study in Section 3.4.3. Firstly, SD and DD can appear kinematically similar in the measured range, especially given that DD events can be asymmetric. Measurements from the ZDC would improve the sensitivity to the SD to DD ratio, increasing the acceptance and degrees of freedom of the fit. Secondly, SD and DD kinematics have larger model uncertainty than ND. The contour in Figure 3.9 shows that, even in the case of 32 triggers, SD and DD fractions are anticorrelated in the fit, so whilst the kinematic uncertainty remains large, determining this ratio via this method may remain difficult.

Further work for this measurement would include tuning specific parts of the MCs available to try to refine the effects of model uncertainty (e.g. the importance of hard diffraction). However, the systematic and model uncertainties demonstrate the need for a more sensitive, less model-dependent measurement, and a more constrained prediction of the kinematic distributions. It is also worth noting that whilst the uncertainty of the measurements is large, there are more sources of uncertainty that may have been underestimated. An important assumption made in this thesis is that PYTHIA 6, PYTHIA 8 and PHOJET describe the uncertainty in theoretical kinematic distributions, which is not necessarily true. The systematic impact of uncertainty in material budget was estimated globally, but clearly localised effects could affect diffractive measurements more dramatically.

The ALICE Detector is undergoing an upgrade [160] using scintillator counters covering the currently blind pseudorapidity range between the V0 (FMD) and ZDC detectors. This will improve the acceptance and increase the potential degrees of freedom for this method of measuring diffrac-

tion. Ideally, Roman pots would be used for identifying intact protons in single-diffractive and elastic events. This will be carried out by TOTEM.

5.2 High Multiplicity

The object of the studies in Chapter 4 was to determine appropriate conditions for high multiplicity data-taking. This required identifying the relevant parameters that would influence a choice of multiplicity threshold:

- Natural rate (influenced by N_{bc} and μ): How does this compare with the maximum minimum bias data-taking rate? How does it compare with the maximum rare trigger data-taking rate?
- Background (pile-up, influenced by μ): what purity would be achieved at a given threshold? At what point does the pile-up become too much?
- Running time (influenced by LHC): What is the accelerator efficiency likely to be over a month? What μ and N_{bc} is achievable during early running?
- Physics considerations: How high in multiplicity would a sample need to be in order to begin probing the physics discussed? What statistics are required for analysis?

Section 4.1 shows that the author established quantitative ideals addressing the first two points. To achieve this successfully, the author investigated the effect of pile-up on multiplicity for a variety of interaction rates and developed a model-independent tool for extracting the purity of a sample as a function of pixel chip multiplicity threshold. It was established that optimal data-taking could be achieved by balancing high N_{bc} (around 20 or higher) with a low μ (higher than 0.2 would have too large a contamination at any useful multiplicity threshold). μ=0.05 is sufficiently low, and much lower drops the rate too much. As shown in Section 4.2, the author then demonstrated, under these optimal conditions, that the resulting data sample could be used in strangeness analysis - the required statistics could be obtained in three months for π/K/p ratios, ϕ, Λ and Ξ yields, with

suitable significance and greater than 5 times the mean $dN/d\eta$. This served as an example of the importance of the data and the conditions in which it was taken.

Because of these studies, ALICE rejected the offer from the LHC to take data with μ of 0.2 and N_{bc} of 6, and running conditions were eventually optimised, with 22 to 36 bunches per orbit and 0.04 $\leq \mu \leq$ 0.07. The author's purity extraction method and rate consideration was used for obtaining ideal thresholds for each run. The data-taking rate was at first thought to be limited to 10 Hz per rare trigger, but the HM trigger was actually given 100 Hz. Over 16 million HM events have been obtained, and after background removal the statistics far exceed those required for the strangeness analyses.

Studies of the pile-up removal software [137] have shown hints that its efficiency is very high at high multiplicity - the extracted single interaction multiplicity shape was compared with the multiplicity distribution using pile-up-removed data, and the tail is perfectly reproduced. This implies the large amount of contamination tolerated in the HM events can be removed successfully, as was assumed. This is not so surprising, as with greater multiplicity, primary and additional vertices will be more easily reconstructed.

The final section focuses on one particular analysis - the ϕ - which has interesting physics implications at high multiplicity. The chapter outlines some of the details involved in analysing real data, and demonstrates that TPC PID improves the significance of the ϕ at low momenta. This minimum bias study is a hint of the 7 TeV analysis ongoing in the ALICE resonances group, which is discussed in [157]. Strangeness in minimum bias 900 GeV data has been published [144], [145]. Analysis of the HM data is underway, and with additional PID available from other subdetectors, significance will be improved at high p_T.

Appendix A

Mandelstam Variables

The relativistic energy-momentum relation (using natural units) is:

$$M^2 = E^2 - p^2 \tag{A.1}$$

where M is the mass of a body and E and p are its energy and momentum respectively. M^2 is a Lorentz invariant quantity, known as "invariant mass" squared.

Consider a relativistic two particle to two particle exchange, such as ab→cd, as indicated in Figure A.1.

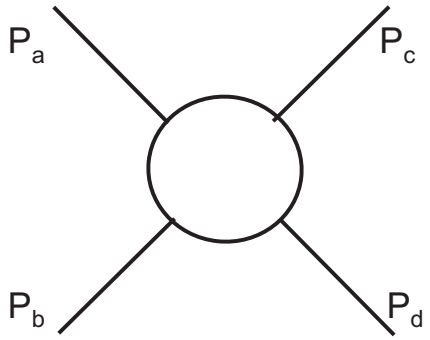

Figure A.1: Schematic diagram of two particles, a and b, interacting and leaving as particles c and d.

P_a and P_b are the four-momenta, P (E, p_x, p_y, p_z) of the two incoming particles and P_c and P_d are the four-momenta of the leaving particles, in the centre of mass frame. To conserve energy and momentum, a number of variables known as Mandelstam variables can be defined:

$$s = (P_a + P_b)^2 = (P_c + P_d)^2; \tag{A.2}$$

$$t = (P_a - P_c)^2 = (P_b - P_d)^2; \tag{A.3}$$

$$u = (P_a - P_d)^2 = (P_b - P_c)^2; \tag{A.4}$$

$$\tag{A.5}$$

s is the centre of mass energy squared and t can be thought of as the momentum transfer squared in the exchange.

Appendix B

Supplementary tables for Diffractive Fractions Analysis

Table B.1: The uncorrelated trigger efficiencies and number of triggered events for the 900 GeV PYTHIA 6 sample. Triggers 1 - 16.

Trigger	ε_{ND}	ε_{SD}	ε_{DD}	N^{trig}
Tr1	0.001	0.282	0.138	7971
Tr2	0.003	0.038	0.041	1529
Tr3	0.001	0.064	0.064	2281
Tr4	0.034	0.172	0.174	8139
Tr5	0.002	0.084	0.096	3153
Tr6	0.025	0.140	0.167	6787
Tr7	0.005	0.003	0.043	907
Tr8	0.919	0.188	0.234	67295
Tr9	0	0.006	0.004	173
Tr10	0	0	0.001	25
Tr11	0	0	0.002	31
Tr12	0	0.001	0.005	100
Tr13	0	0.002	0.001	57
Tr14	0	0.002	0.003	91
Tr15	0	0	0.001	12
Tr16	0.007	0.002	0.004	560

Table B.2: The uncorrelated trigger efficiencies and number of triggered events for the 900 GeV PYTHIA 6 sample. Triggers 17 to 32.

Trigger	ε_{ND}	ε_{SD}	ε_{DD}	N^{trig}
Tr17	0	0.007	0.005	217
Tr18	0	0.001	0.001	33
Tr19	0	0.002	0.001	44
Tr20	0	0.003	0.002	101
Tr21	0	0	0.003	36
Tr22	0	0	0.005	80
Tr23	0	0	0.001	12
Tr24	0.004	0.003	0.004	355
Tr25	0	0	0	4
Tr26	0	0	0	0
Tr27	0	0	0	0
Tr28	0	0	0	2
Tr29	0	0	0	1
Tr30	0	0	0	0
Tr31	0	0	0	0
Tr32	0	0	0	4

Table B.3: The uncorrelated trigger efficiencies and number of triggered events for the 900 GeV PHOJET sample. Triggers 1 - 16.

Trigger	ε_{ND}	ε_{SD}	ε_{DD}	N^{trig}
Tr1	0	0.184	0.04	3850
Tr2	0.001	0.013	0.056	808
Tr3	0	0.071	0.039	1731
Tr4	0.033	0.203	0.152	7546
Tr5	0.001	0.095	0.053	2320
Tr6	0.019	0.166	0.127	5603
Tr7	0.001	0	0.036	424
Tr8	0.925	0.248	0.476	75777
Tr9	0	0.003	0.001	64
Tr10	0	0	0	3
Tr11	0	0	0.001	9
Tr12	0.001	0.001	0.002	84
Tr13	0	0.001	0.001	30
Tr14	0	0.002	0	66
Tr15	0	0	0.001	8
Tr16	0.010	0.003	0.005	805

Table B.4: The uncorrelated trigger efficiencies and number of triggered events for the 900 GeV PHOJET sample. Triggers 17 - 32.

Trigger	ε_{ND}	ε_{SD}	ε_{DD}	N^{trig}
Tr17	0	0.003	0	59
Tr18	0	0	0	3
Tr19	0	0.001	0	21
Tr20	0.001	0.002	0.001	73
Tr21	0	0	0	6
Tr22	0	0	0.002	41
Tr23	0	0	0.001	8
Tr24	0.008	0.003	0.006	643
Tr25	0	0	0	0
Tr26	0	0	0	0
Tr27	0	0	0	0
Tr28	0	0	0	2
Tr29	0	0	0	0
Tr30	0	0	0	0
Tr31	0	0	0	1
Tr32	0	0	0	15

Table B.5: The number of triggered events N^{trig} for PHOJET, 50 % PYTHIA-PHOJET mix, and PYTHIA, using fixed fractions given in table 3.6. Triggers 1 - 16.

Trigger	N^{trig}_{PHOJET}	$N^{trig}_{50\%PYTHIA}$	N^{trig}_{PYTHIA}
Tr1	4184	5738	7293
Tr2	937	1170	1402
Tr3	1910	1986	2063
Tr4	8029	7843	7658
Tr5	2560	2703	2845
Tr6	6032	6183	6333
Tr7	493	663	832
Tr8	73903	71813	69723
Tr9	69	113	157
Tr10	3	12	22
Tr11	10	18	26
Tr12	86	87	88
Tr13	33	42	51
Tr14	71	77	82
Tr15	8	9	10
Tr16	785	679	572

Table B.6: The number of triggered events N^{trig} for PHOJET, 50 % PYTHIA-PHOJET mix, and PYTHIA, using fixed fractions given in table 3.6. Triggers 17-32.

Trigger	N^{trig}_{PHOJET}	$N^{trig}_{50\%PYTHIA}$	N^{trig}_{PYTHIA}
Tr17	64	130	197
Tr18	2	16	29
Tr19	22	31	40
Tr20	77	85	92
Tr21	6	18	30
Tr22	45	57	69
Tr23	9	10	10
Tr24	630	493	355
Tr25	0	1	3
Tr26	0	0	0
Tr27	0	0	0
Tr28	2	1	1
Tr29	0	0	0
Tr30	0	0	0
Tr31	1	0	0
Tr32	14	9	4

Table B.7: The uncorrelated trigger efficiencies and number of triggered events for the 7 TeV PYTHIA 6 sample corresponding to the 7 TeV data sample used. Triggers 1 - 16.

Trigger	ε_{ND}	ε_{SD}	ε_{DD}	N^{trig}
Tr1	0.00026	0.10177	0.0181	6654
Tr2	0.00006	0.00226	0.00092	179
Tr3	0.00052	0.03164	0.01201	2409
Tr4	0.00207	0.03525	0.01608	3090
Tr5	0.00122	0.04482	0.02128	3674
Tr6	0.0028	0.02885	0.01485	2820
Tr7	0.00311	0.01148	0.01816	2006
Tr8	0.344	0.14091	0.07	80736
Tr9	0.00015	0.07388	0.02958	5465
Tr10	0.00004	0.00112	0.00141	129
Tr11	0.00036	0.00048	0.01895	841
Tr12	0.00127	0.00335	0.02535	1442
Tr13	0.00069	0.06013	0.02822	4725
Tr14	0.00195	0.03686	0.02156	3372
Tr15	0.00218	0.00849	0.02366	1859
Tr16	0.22248	0.10165	0.08976	54562

Table B.8: The uncorrelated trigger efficiencies and number of triggered events for the 7 TeV PYTHIA 6 sample corresponding to the 7 TeV data sample used. Triggers 17 to 32.

Trigger	ε_{ND}	ε_{SD}	ε_{DD}	N^{trig}
Tr17	0.00019	0.09486	0.02794	6624
Tr18	0.00006	0.00193	0.00207	205
Tr19	0.0004	0.046	0.01695	3406
Tr20	0.00151	0.0473	0.02108	3870
Tr21	0.00068	0.00123	0.03286	1438
Tr22	0.00191	0.00394	0.02487	1647
Tr23	0.00224	0.00886	0.02397	1904
Tr24	0.24556	0.09832	0.10011	59460
Tr25	0.00005	0.00116	0.0492	1999
Tr26	0.00002	0	0.00213	88
Tr27	0.00017	0.00006	0.02558	1038
Tr28	0.00099	0.00041	0.03275	1504
Tr29	0.00047	0.00081	0.04492	1897
Tr30	0.00139	0.00078	0.03165	1564
Tr31	0.00159	0.00076	0.03163	1601
Tr32	0.15959	0.01065	0.12241	37798

Table B.9: The uncorrelated trigger efficiencies and number of triggered events for the 7 TeV PHOJET sample corresponding to the 7 TeV data sample used. Triggers 1 - 16.

Trigger	ε_{ND}	ε_{SD}	ε_{DD}	N^{trig}
Tr1	0.00007	0.09811	0.01878	4340
Tr2	0.00002	0.00072	0.00744	180
Tr3	0.00027	0.047	0.037	2687
Tr4	0.0018	0.05664	0.05897	3864
Tr5	0.00043	0.06937	0.05325	3946
Tr6	0.00187	0.05026	0.04981	3442
Tr7	0.00184	0.00414	0.02273	1042
Tr8	0.40773	0.23302	0.22979	108175
Tr9	0.00002	0.04944	0.01083	2211
Tr10	0.00001	0.00009	0	6
Tr11	0.00016	0.00017	0.01073	255
Tr12	0.0008	0.00079	0.01448	504
Tr13	0.00029	0.05108	0.01301	2383
Tr14	0.00101	0.02864	0.00881	1562
Tr15	0.00109	0.00112	0.01579	608
Tr16	0.2114	0.079	0.10781	54178

Table B.10: The uncorrelated trigger efficiencies and number of triggered events for the 7 TeV PHOJET sample corresponding to the 7 TeV data sample used. Triggers 17 - 32.

Trigger	ε_{ND}	ε_{SD}	ε_{DD}	N^{trig}
Tr17	0.00003	0.06393	0.01159	2812
Tr18	0.00001	0.0003	0.0002	19
Tr19	0.00019	0.0373	0.00769	1697
Tr20	0.00115	0.03549	0.00815	1856
Tr21	0.00026	0.00119	0.02131	530
Tr22	0.00101	0.00099	0.01701	610
Tr23	0.00117	0.00169	0.01524	639
Tr24	0.236	0.07453	0.11449	59816
Tr25	0.00002	0.00077	0.01174	268
Tr26	0	0.00002	0.00015	5
Tr27	0.00008	0.00007	0.00663	154
Tr28	0.00058	0.00015	0.00896	318
Tr29	0.00017	0.00082	0.01655	399
Tr30	0.00061	0.0004	0.00931	342
Tr31	0.00076	0.00009	0.01103	397
Tr32	0.12912	0.01268	0.08083	31955

Table B.11: The uncorrelated trigger efficiencies and number of triggered events for the 7 TeV PYTHIA 8 sample corresponding to the 7 TeV data sample used. Triggers 1 - 16.

Trigger	ε_{ND}	ε_{SD}	ε_{DD}	N^{trig}
Tr1	0	0.11412	0.02317	3748
Tr2	0	0.00014	0	4
Tr3	0.00004	0.04087	0.01636	1505
Tr4	0.00058	0.04808	0.02296	1899
Tr5	0.00001	0.05775	0.03211	2299
Tr6	0.00041	0.03952	0.0251	1676
Tr7	0.00058	0.00153	0.01753	449
Tr8	0.38987	0.20275	0.09765	47799
Tr9	0	0.07207	0.03348	2738
Tr10	0	0.0001	0.00015	6
Tr11	0.00003	0.00003	0.02434	483
Tr12	0.00056	0.00038	0.03409	739
Tr13	0.00002	0.04368	0.02479	1750
Tr14	0.00044	0.02926	0.01951	1273
Tr15	0.00037	0.00042	0.01605	366
Tr16	0.21683	0.08077	0.0912	26387

Table B.12: The uncorrelated trigger efficiencies and number of triggered events for the 7 TeV PYTHIA 8 sample corresponding to the 7 TeV data sample used. Triggers 17 - 32.

Trigger	ε_{ND}	ε_{SD}	ε_{DD}	N^{trig}
Tr17	0	0.09606	0.03175	3396
Tr18	0	0.00024	0.0002	11
Tr19	0.00001	0.03283	0.01423	1228
Tr20	0.00046	0.04472	0.02098	1750
Tr21	0.00002	0.00066	0.04379	883
Tr22	0.00058	0.00069	0.03155	701
Tr23	0.00052	0.00066	0.01494	366
Tr24	0.23932	0.08212	0.10877	29081
Tr25	0	0.00139	0.04887	1002
Tr26	0	0	0.0003	6
Tr27	0.00002	0	0.01804	357
Tr28	0.00039	0	0.02606	553
Tr29	0.00005	0.00035	0.0346	697
Tr30	0.00045	0.00045	0.02418	535
Tr31	0.00037	0.00003	0.01285	292
Tr32	0.14805	0.00835	0.09038	17221

Table B.13: The number of triggered events in the 900 GeV and 7 TeV data samples in the 28 measured triggers. Triggers 1 - 16 (no Tr1 or Tr9).

Trigger	900 GeV N^{trig}	900 GeV N^{trig}_{corr}	7 TeV N^{trig}	7 TeV N^{trig}_{corr}
Tr1	n/a	n/a	n/a	n/a
Tr2	1182	1139	756	616
Tr3	10274	10050	3658	3350
Tr4	11218	10843	3772	3268
Tr5	17761	17201	5832	5665
Tr6	10732	10587	3500	3310
Tr7	8520	8516	1997	1997
Tr8	260355	260343	115278	115270
Tr9	n/a	n/a	n/a	n/a
Tr10	29	29	124	124
Tr11	155	154	826	826
Tr12	224	224	1222	1222
Tr13	613	613	3538	3536
Tr14	310	308	1948	1930
Tr15	260	260	1199	1199
Tr16	5433	5433	46480	46480

Table B.14: The number of triggered events in the 900 GeV and 7 TeV data samples in the 28 measured triggers. Triggers 17 - 32 (no Tr17 or Tr25).

Trigger	900 GeV N^{trig}	900 GeV N^{trig}_{corr}	7 TeV N^{trig}	7 TeV N^{trig}_{corr}
Tr17	n/a	n/a	n/a	n/a
Tr18	23	23	182	180
Tr19	402	399	2435	2350
Tr20	305	299	2452	1548
Tr21	340	340	1548	1548
Tr22	296	296	1543	1543
Tr23	318	318	1425	1423
Tr24	6628	6628	56322	56322
Tr25	n/a	n/a	n/a	n/a
Tr26	0	0	54	54
Tr27	2	2	606	606
Tr28	14	14	817	817
Tr29	14	14	1090	1090
Tr30	8	8	932	932
Tr31	7	7	920	920
Tr32	170	170	26970	26970

Appendix C

Measured Diffraction as a Fraction of Minimum Bias Data

Correcting the measured fractions of the inelastic cross-section for minimum bias efficiency, the fractions of the minimum bias data sample can be obtained and are found to be

- f_{SD}(MB) =0.166±0.071
- f_{DD}(MB) =0.075±0.051
- f_{ND}(MB) =0.759±0.058

and for 7 TeV:

- f_{SD}(MB) =0.179 ±0.074
- f_{DD}(MB) =0.048 ±0.057
- f_{ND}(MB) =0.772 ±0.058

Appendix D

Iterative Method for Extracting Multiplicity Shape

Consider the form of the multiplicity distribution

$$\frac{\mathrm{d}N}{\mathrm{d}m} = f(m), \tag{D.1}$$

where m is the measured multiplicity and $f(m)$ is normalised to 1. The probabilities $\mathrm{P}(\mu, n)$, from Poisson statistics, determine the probabilities for n-fold pile-up. In ALICE μ is <0.1, so only the first few pile-up terms are needed.

The distribution for double-interaction pile-up, $F_2(m)$, is the sum of two interactions each following the shape of the original distribution independent of one another, normalised to the probability associated with double-interactions. This is given by

$$\mathrm{F}_2(m) \quad = \quad \frac{1}{a_2} \int_{l_1}^{l_2} \int_{l_1}^{l_2} f(m_1) f(m_2)\, \delta(m - m_1 - m_2)\, \mathrm{d}m_1 \mathrm{d}m_2,$$

$$a_2(l_1, l_3) = \int_{l_1}^{l_3} \int_{l_1}^{l_2} \int_{l_1}^{l_2} f(m_1) f(m_2)\, \delta(m - m_1 - m_2)\, \mathrm{d}m_1 \mathrm{d}m_2 \mathrm{d}m \tag{D.2}$$

where l_1, l_2 and l_3 are the limits of the multiplicity ranges being considered, as only a finite sample will be used. Generalizing,

$$\mathrm{F}_n(m) = \frac{1}{a_n} \int_{l_1}^{l_2} \ldots \int_{l_1}^{l_2} f(m_1) \ldots f(m_n)\, \delta(m - m_1 - \ldots m_n)\, \mathrm{d}m_1 \ldots \mathrm{d}m_n \tag{D.3}$$

with

$$a_n(l_1, l_j) = \int_{l_1}^{l_j} \ldots \int_{l_1}^{l_2} f(m_1) \ldots f(m_n)\, \delta(m - m_1 - \ldots m_n)\, \mathrm{d}m_1 \ldots \mathrm{d}m_n\, \mathrm{d}m \tag{D.4}$$

In the remainder of this text, the integral limits l_1, l_2 ... l_j are implied but not written explicitly.

Integrals $\mathrm{H}_{jk}(m)$, corresponding to the convolution of two of the $\mathrm{F}_j(m)$, can be defined:

$$\begin{aligned}
\mathrm{H}_{jk}(m) &= \int \mathrm{F}_j(m_1) \mathrm{F}_k(m_2)\, \delta(m - m_1 - m_2)\, \mathrm{d}m_1 \mathrm{d}m_2 \\
&= \frac{1}{a_j a_k} \int \ldots \int f(m_3) \ldots f(m_{3+j-1}) f(m_{3+j}) \ldots f(m_{3+j+k-1}) \times \\
&\quad \delta(m - m_1 - m_2)\, \delta(m_1 - m_3 - \ldots m_{3+j-1}) \times \\
&\quad \delta(m_2 - m_{3+j} - \ldots\ m_{3+j+k-1})\, \mathrm{d}m_1 \ldots \mathrm{d}m_{3+j+k-1} \\
&= \frac{1}{a_j a_k} \int \ldots \int f(m_3) \ldots\ f(m_{3+j+k-1}) \times \\
&\quad \delta(m - m_3 - m_{3+j+k-1}) \mathrm{d}m_3 \mathrm{d}m_{3+j+k-1} \\
&= \frac{a_{j+k}}{a_j a_k} \mathrm{F}_{j+k}(m)
\end{aligned} \tag{D.5}$$

For example, for the first few cases:

$$\begin{aligned}
\mathrm{H}_{11} &= \frac{a_2}{a_1^2}\ \mathrm{F}_2(m), \\
\mathrm{H}_{21} &= \frac{a_3}{a_1 a_2}\ \mathrm{F}_3(m),
\end{aligned}$$

$$\begin{aligned} \mathrm{H}_{31} &= \frac{a_4}{a_3 a_1} \quad \mathrm{F}_4(m), \\ \mathrm{H}_{22} &= \frac{a_4}{a_2 a_2} \quad \mathrm{F}_4(m). \end{aligned} \tag{D.6}$$

The iterative method for extracting the single interaction shape, as outlined in Section 4.1.5, can now be considered. Let the overall multiplicity distribution (including pile-up) be written as $\mathcal{G}(m)$, where

$$\begin{aligned} \frac{\mathrm{d}N_{\mathrm{meas}}}{\mathrm{d}m} &\equiv \mathcal{G}(m) \\ &= f(m) + p(2)\mathrm{F}_2(m) + p(3)\mathrm{F}_3(m) \end{aligned} \tag{D.7}$$

where

$$p(n) = \frac{\mathrm{P}(\mu, n)}{\mathrm{P}(\mu, 1)} \tag{D.8}$$

The principle of the iterative method is to use the total distribution, $\mathcal{G}(m)$ as a first approximation to the 'single interaction' distribution $f(m)$. Writing $\mathcal{F}^{(n)}$ as the nth iteration approximation to the single interaction distribution, with $\mathcal{F}^{(0)}(m) \equiv \mathcal{G}(m)$;

$$\begin{aligned} \mathcal{F}_2^{(0)}(m) &= \frac{1}{\alpha_2^0} \int\int \mathcal{F}^{(0)}(m_1)\mathcal{F}^{(0)}(m_2)\delta(m - m_1 - m_2)\mathrm{d}m_1\mathrm{d}m_2 \\ &= \frac{1}{\alpha_2^0} \int\int \left(f(m_1) + p(2)\mathrm{F}_2(m_1)\right)\left(f(m_2) + p(2)\mathrm{F}_2(m_2)\right) \\ &\quad \times\delta(m - m_1 - m_2)\mathrm{d}m_1\mathrm{d}m_2 \end{aligned} \tag{D.9}$$

where α_2^0 is a suitable normalization factor, defined similarly to a_2:

$$\alpha_2^{(n)} = \int \mathcal{F}_2^{(n)}(m)dm, \tag{D.10}$$

where the superscript '(n)' refers to the iteration number (see below). Expanding this out and using equations (D.5) and (D.6) gives

$$\begin{aligned} \mathcal{F}_2^{(0)}(m) &= \frac{1}{\alpha_2^{(0)}} \int\int \left(f(m_1) + p(2)\mathrm{F}_2(m_1)\right)\left(f(m_2) + p(2)\mathrm{F}_2(m_2)\right) \\ &\quad \times\delta(m - m_1 - m_2)\mathrm{d}m_1\mathrm{d}m_2 \end{aligned}$$

$$
\begin{aligned}
&= \frac{1}{\alpha_2^{(0)}} \left\{ a_2 \mathrm{F}_2(m) + 2\, p(2) \mathrm{H}_{12}(m) + p(2))^2 \mathrm{H}_{22}(m) \right\} \\
&= \frac{1}{\alpha_2^{(0)}} \left\{ a_2 \mathrm{F}_2(m) + 2p(2) \frac{a_3}{a_1 a_2} \mathrm{F}_3(m) + p(2)^2 \frac{a_4}{a_2 a_2}\, \mathrm{F}_4(m) \right\} \qquad \text{(D.11)}
\end{aligned}
$$

The next step of the iterative method involves subtracting the estimate of the pile-up from the original distribution $\mathrm{G}(m)$ to obtain the next-iteration estimate of the 'single' distribution, $\mathcal{F}_1(m)$:

$$
\begin{aligned}
\mathcal{F}_1^{(1)}(m) &= f(m) + p(2) \left(1 - \frac{a_2}{\alpha_2^{(0)}} \right) - \frac{1}{\alpha_2^{(0)}} p(2)^2 \frac{a_3}{a_2 a_1} \mathrm{F}_3(m) \\
&\quad - \frac{1}{\alpha_2^{(0)}} p(2)^3 \frac{a_4}{a_2 a_1} \mathrm{F}_4(m) \qquad \text{(D.12)}
\end{aligned}
$$

One can see that the later terms are small, provided that that μ is small (making the higher order terms less probable) and provided that the normalisation ratios $\frac{a_3}{a_2 a_1}$ and $\frac{a_4}{a_2 a_1}$ (and the other normalisation ratios found in $\mathrm{H}_{jk}(m)$) are also small. The additional terms tend to vanish as iterations increase, and we eventually obtain:

$$
\mathcal{F}_1^{(n)}(m) \quad \rightarrow \quad f(m) \qquad \text{(D.13)}
$$

as required.

Bibliography

[1] A. Aamodt *et al.*; The ALICE Collaboration. First proton-proton collisions at the LHC as observed with the ALICE detector: measurement of the charged-particle pseudorapidity density at $\sqrt{s}$=900 GeV. *Eur. Phys. J*, C65:111–125, 2010. [2, 70]

[2] Z. L. Matthews. Estimating the fractions of diffractive processes using the ALICE detectors. *ALICE Internal Note*, ALICE-INT-2009-027 v2, 2009. [2, 71]

[3] Z. L. Matthews. Strangeness in high multiplicity proton-proton collisions in the ALICE experiment. *J. Phys. G: Nucl. and Part. Phys.*, 37 SI(094048), 2010. [4]

[4] A. Bhasin *et al.* for The ALICE Collaboration. Resonance Production at ALICE: ρ and ϕ. *I. J. Phys*, 84:1739–1743, 2010. [4]

[5] W. K. H. Panofsky. Electromagnetic Interactions: Low q^2 Electrodynamics: Elastic and Inelastic Electron and muon Scattering. *Proc. 14th Int. Conf. on High Energy Physics (Vienna)*, page 37, Aug 1968. [5]

[6] W.J. Stirling R.K. Ellis and B.R. Webber. *QCD and collider physics*. Cambridge University Press, 1996. [5, 8, 9]

[7] C. Amsler et al. Review of Particle Physics. *Physics Letters B*, 1, 2008. Particle Data Group. [5, 142]

[8] M. R. Pennington. Swimming With Quarks. *J. Phys. Conf. Ser.*, 18(1), 2004. [6, 8]

[9] V. M. Bannur. E. O. S. for a Non-Ideal Quark Gluon Plasma. *Phys. Lett.*, B 362(7), 1995. [7]

[10] D. Bailin and A. Love. *Introduction to Gauge Field Theory.* University of Sussex Press, 1986. [7]

[11] E. Laermann F. Karsch and A. Piekert. The pressure in 2, 2+ 1 and 3 flavour QCD. *Phys. Lett.*, B 478(447), 2000. [8]

[12] K. Safarik S. Margetis and O. Villalobos Baillie. Strangeness Production in Heavy-Ion Collisions. *Annu. Rev. Nucl. Part. Sci.*, 50:299–342, 2000. [9, 16]

[13] K. Johnson A Chodos, R. L. Jaffe and C. B. Thorn. Baryon Structure in the Bag Theory. *Phys. Rev.*, D 10(8), 1974. [10]

[14] D. N. Schramm *et al.* Quark Matter and Cosmology. *Fermilab Conference, Nucl. Phys.*, A544:267c–278c, 1992. [11]

[15] B. Holzman for The E917 Collaboration. Systematic Study of Au-Au Collisions with AGS Experiment E917. *Nucl. Phys.*, A698:643–646, 2002. [11]

[16] B. Tore Knudsen. Presentation of the WA97 Experiment at CERN. *Czech. J. Phys.*, 47(9):925–929, 1997. [11]

[17] T. Ludlam M. Harrison and S. Ozaki. RHIC project overview. *Nuclear Instruments and Methods in Physics Research, Section A*, 499(2-3):235–244, March 2003. [11]

[18] J. W. Harris and The STAR Collaboration. The STAR Experiment at the Relativistic Heavy Ion Collider. *Nucl. Phys.*, A 566(277c-286c), 1994. [11]

[19] B. Wyslouch. The PHOBOS Experiment at RHIC and AGS. *Nucl. Phys.*, A 566(305c), 1994. [11]

[20] The PHENIX Collaboration D. P. Morrison *et al.* The PHENIX Experiment at RHIC. *Nucl. Phys.*, A 638:565–570, 1998. [11]

[21] F Videbaek for the BRAHMS Collaboration. The BRAHMS Experiment at RHIC. *Nucl. Phys.*, A 566(299c-304c), 1994. [11]

[22] J. Schukraft. Heavy ions at the LHC: Physics perspectives and experimental program. *Nucl. Phys.*, A 698:287, 2002. CERN-ALI-2001-009. [11, 12]

[23] A. Toia for The ALICE Collaboration. *Proc. for QM Annecy*, 2011. [12]

[24] J. Lettessier and J. Rafelski. *Hadrons and Quark-Gluon Plasma.* Cambridge University Press, 2002. [15]

[25] C. A. Ogilvie. Dense, strongly interacting matter: strangeness in heavy-ion reactions 1-10 A GeV. *J. Phys. G - Nucl. Part. Phys.*, 25:159, 1999. Proc. Strangeness in Quark Matter 1998, Padua. [16]

[26] J. B. Kinson. Overview of the experimental situation at CERN. *J. Phys. G - Nucl. Part. Phys.*, 25:143, 1999. Proc. Strangeness in Quark Matter 1998, Padua. [16]

[27] F. Antinori *et al. for The WA97 Collaboration. Phys. Lett.*, B433:209, 1998. [16]

[28] E. Shuryak. *Phys. Rep.*, 391:381, 2004. [16]

[29] G. Torrieri and J. Rafelski. Strange Hadron Resonances and QGP Freeze-out. *J. Phys. G: Nucl. Phys.*, 3(12):1, February 2002. Proceedings of Strangeness in Quark Matter 2001, Frankfurt. [16]

[30] S. Afanasiev *et al.*; The NA49 Collaboration. *Phys. Lett.*, B 491(59), 2000. [16, 143]

[31] N. Xu *et al. J. Phys.*, G 35(044031), 2008. [16, 143]

[32] R. Matsui and H. Satz. J/ψ Suppression by Quark-Gluon Plasma formation. *Phys. Lett.*, B 178(4):416–422, 1986. [17]

[33] H. Satz. Colour Deconfinement and J/ψ Suppression in High Energy Nuclear Collisions. Lecture given at the 35th Course of the International School of Subnuclear Physics, Erice/Sicily: arXiv:hep-ph/9711289v1, 26th August 1997. [17]

[34] The NA50 Collaboration B. Alessandro *et al.* A New Measurement of J/ψ suppression in Pb-Pb collisions at 158 GeV per Nucleon. *Eur. Phys. J.*, C 39:335–345, 2005. [17]

[35] S. Gavin and R. Vogt. J/ψ Suppression from Hadron-Nucleus to Nucleus-Nucleus Collisions. *Nucl. Phys.*, B345:104–124, 1990. [17]

[36] P. Pillot for The ALICE Collaboration. J/ψ production in Pb-Pb collisions at $\sqrt{s_{NN}}$=2.76 TeV. *Proc. for QM Annecy*, (arXiv:1108.3795v1 [hep-ex]), 2011. [17]

[37] J. D. Bjorken. Energy Loss of Energetic Partons in Quark-Gluon Plasma: Possible Extinction of High p_T Jets in Hadron-Hadron Collisions. Fermilab report: Fermilab-Pub-82/59-THY, 1982. [18, 24, 118]

[38] X.-N. Wang and M. Gyulassy. *Phys. Rev. Lett.*, 68:1480, 1992. [18]

[39] J. Adams *et al.*; The STAR Collaboration. Transverse momentum and collision energy dependence of high p_T hadron suppression in Au+Au collisions at ultrarelativistic energies. *Phys. Rev. Lett.*, 91(172302), 2003. [18]

[40] J. Adams *et al.*; The STAR Collaboration. Evidence from $d + Au$ Measurements for Final-State Suppression of High-p_T Hadrons in $Au + Au$ Collisions at RHIC. *Phys. Rev. Lett.*, 91(7):072304, 2003. [18]

[41] B. Mueller and J. L. Nagle. Results from the Relativistic Heavy Ion Collider. *Annu. Rev. Nucl. Part. Sci.*, 56:93–135, 2006. [18, 23]

[42] Berkeley Laboratory. Jetting into the Quark Gluon Plasma. *Berkeley Laboratory homepage, http://newscenter.lbl.gov/wp-content/uploads/jet-quench.jpg*, 2010. [18]

[43] K. Aamodt *et al.*; The ALICE Collaboration. Suppression of Charged Particle Production at Large Transverse Momentum in Central Pb-Pb Collisions at $\sqrt{s} = 2.76$ TeV. *Phys. Lett.*, B696:30–39, 2011. [18]

[44] A. M. Poskanzer S. A. Voloshin and R. Snellings. Collective phenomena in non-central nuclear collisions. *arXiv:0809.2949v2 [nucl-ex]*, 2008. [21, 22]

[45] H. A. Gustafsson *et al.* Collective Flow Observed in Relativistic Nuclear Collisions. *Phys. Rev. Lett.*, 52(18), 1984. [21]

[46] The E895 Collaboration C. Pinkenburg *et al. Phys. Rev. Lett.*, 83(1295), 1999. [21]

[47] P. Saturnini for the NA50 Collaboration. *Nucl. Phys.*, A661(345c), 1999. [21]

[48] The STAR Collaboration K. H. Ackermann *et al.* Flow. *Phys. Rev. Lett.*, 86:402–407, 2001. [21]

[49] The ALICE Collaboration K. Aamodt *et al.* Elliptic flow of charged particles in Pb-Pb collisions at 2.76 TeV. *Phys. Rev. Lett.*, 105(252302), 2010. [21, 23]

[50] J. P. Wessels N. Herrmann and T. Wienold. Collective Flow in Heavy Ion Collisions. *Ann. Rev. Nucl. Part. Sci.*, 49:581–632, 1999. [21]

[51] R. Snellings. Elliptic Flow: A Brief Review. *arXiv:1102.3010v1 [nucl-ex]*, 2011. [22]

[52] L. P. Csernai. Detonation Across a Time-like Surface for Relativistic Systems. *Zh. Eksp. Teor. Fiz.*, 92:379, 1987. [23]

[53] A. O. Starinets P. Kovtun, D. T. Son. *Phys. Rev. Lett.*, 94(11):1601, 2005. [23]

[54] J. P. Revol. First Measurements at LHC: Early Hadronic Physics (Soft and QCD) With ALICE, ATLAS, CMS, TOTEM and LHCb. *Nuclear Physics*, B (Proc. Supplement), 2008. [23]

[55] J. D. Bjorken. Highly relativistic nucleus-nucleus collisions: The central rapidity region. *Phys. Rev.*, D 27:140, 1983. [23, 117]

[56] J. D. Bjorken. Rapidity gaps and jets as a new-physics signature in very-high-energy hadron-hadron collisions. *Phys. Rev.*, D47(1):1, 1993. [24, 29]

[57] C. B. Chui. Evidence for Regge Poles and Hadron Collisions at High Energies. *Ann. Rev. Nucl. Sci.*, 22:255, 1972. [25]

[58] M. Perl. *High Energy Hadron Physics.* Wiley, 1974. [25]

[59] D. H. Perkins. *Introduction to High Energy Physics*. Addison-Wesley, 1972. [25]

[60] M. Froissart. Asymptotic Behavior and Subtractions in the Mandelstam Representation. *Phys. Rev.*, 123:1053–1057, 1961. [26]

[61] G. F. Chew. S-Matrix Theory of Strong Interactions Without Elementary Particles. *Rev. Mod. Phys.*, 34(3), 1962. [27]

[62] A. Donnachie and P. V. Landshoff. *Phys. Lett.*, B296:227, 1992. [28]

[63] A. H. Mueller. *Phys. Rev.*, D2:2963, 1970. [28]

[64] O. V. Kancheli. *Pisma Zh. Eksp. Teor. Fiz.*, 11:397, 1970. [28]

[65] V. Barone and E. Predazzi. *High-Energy Particle Diffraction*. Springer, 2002. [29, 32]

[66] A. B. Kaidalov. The Quark-Gluon Structure of the Pomeron and the Rise of Inclusive Spectra at High Energies. *Phys. Lett.*, B 116:459, 1982. [31, 74]

[67] H. O. Bengtsson and T. Sjostrand. *Comput. Phys. Commun.*, 46(43), 1987. [31, 71, 119]

[68] R. Engel. *Hadronic Interactions of Photons at High Energies*. PhD thesis, Universitat Gesamthochschule Siegen, 7 February 1997. [31, 71, 119]

[69] U. Maor E. Gotsman, E. Levin and J. S. Miller. A QCD motivated model for soft interactions at high energies. *Eur. Phys. J.*, C57:689–709, 2008. [31]

[70] The UA5 Collaboration G. J. Alner *et al.* antiproton-proton cross sections at 200 and 900 gev c.m. energy. *Z. Phys.*, 1986. [31, 76]

[71] The UA5 Collaboration R. E. Ansorge *et al.* Diffraction Dissociation at the CERN Pulsed p-anti p collider at c.m. energies of 900 GeV and 200 GeV. *Z. Phys.*, C(33):175, 1988. [31, 77]

[72] F. Abe *et al.*; The CDF Collaboration. Measurement of antiproton-proton single diffraction dissociation at $\sqrt{s}$=546 and 1800 GeV. *Phys. Rev.*, D50(9), 1994. [31]

[73] F. Abe *et al.*; The CDF Collaboration. Measurement of the antiproton-proton total cross section at $\sqrt{s}$=546 and 1800 GeV. *Phys. Rev.*, D50(9), 1994. [31]

[74] T. Affolder *et al.*; The CDF Collaboration. Double Diffraction Dissociation at the Fermilab Tevatron Collider. *Phys. Rev. Lett.*, 87(14), 2001. [31]

[75] N. A. Amos *et al.* for The E-710 Collaboration. Diffractive dissociation in proton-antiproton collisions at $\sqrt{s}$=1.8 TeV. *Phys. Lett.*, B301:313–316, 1993. [31]

[76] N. A. Amos *et al.* for The E-710 Collaboration. A luminosity measurement of the proton-antiproton total cross section at $\sqrt{s}$=1.8 TeV. *Phys. Lett.*, B243(1,2), 1990. [31]

[77] C. Avila *et al.* for The E811 Collaboration. A measurement of the proton-antiproton total cross section at $\sqrt{s}$=1.8 TeV. *Phys. Lett.*, B445:419–422, 1999. [31]

[78] G. Aad *et al.*; The ATLAS Collaboration. Measurement of the Inelastic Proton-Proton Cross-Section at $\sqrt{s}$ = 7 TeV with the ATLAS Detector. *Nat. Comm.*, 2:463, 2011. [31]

[79] M. Pogoshyan for The ALICE Collaboration. Diffractive Dissociation in proton-proton collisions at $\sqrt{s}$=0.9 TeV, 2.76 TeV and 7 TeV. *Proc. for QM Anneccy*, 2011. [31, 78, 114, 154]

[80] K. Oyama *et al.* for The ALICE Collaboration. Inelastic Cross Section of pp collisions at ALICE. *Proc. for QM Anneccy*, 2011. [31, 114]

[81] P. V. Landshoff A. Donnachie, G. Dosch and O. Nachtmann. *Pomeron Physics and QCD.* Cambridge University Press, 2002. [30]

[82] S. Ostapchenko. *Phys. Rev.*, D81(114028), 2010. [30]

[83] S. Ostapchenko. *Phys. Lett.*, B703:588, 2011. [30]

[84] A. B. Kaidalov and M.G. Poghosyan. *Eur. Phys. J.*, C67:397, 2010. [30]

[85] M. L. Good and W. D. Walker. Diffraction Dissociation of Beam Particles. *Phys. Rev.*, 120:1857–1860, 1960. [30]

[86] E. Levin E. Gotsman and U. Maor. *Eur. Phys. J.*, C71(1553), 2010. [30]

[87] A.D. Martin M.G. Ryskin and V.A. Khoze. *Eur. Phys. J.*, C71(1617), 2011. [30]

[88] L. Evans and P. Bryant (ed). LHC Machine. *JINST*, 3(S08001), 2008. [33]

[89] CERN. LHC Machine Outreach: LHC Schematic. *LHC Machine Public Website; http://lhc-machine-outreach.web.cern.ch/lhc-machine-outreach/images/lhc-schematic.jpg*, 2011. [34]

[90] CERN. LHC 2008 Inauguration. *https://lhc2008.web.cern.ch/LHC2008/inauguration/lhcexpo.html*, 2008. [36]

[91] The ATLAS Collaboration G. Aad *et al.* The ATLAS Experiment at the CERN LHC. *JINST*, 3(S08003), 2008. [39]

[92] The CMS Collaboration D. Abbaneo *et al.* The CMS Experiment at the CERN LHC. *JINST*, 3(S08004), 2008. [39]

[93] The ALICE Collaboration K. Aamodt *et al.* The ALICE Experiment at the CERN LHC. *JINST*, 3(S08002), 2008. [39, 56, 58, 59, 128]

[94] The LHCb Collaboration L. Abadie *et al.* The LHCb Experiment at the CERN LHC. *JINST*, 3(S08005), 2008. [39]

[95] The LHCf Collaboration O. Adriani *et al.* The LHCf Experiment at the CERN LHC. *JINST*, 3(S08006), 2008. [39]

[96] The TOTEM Collaboration G. Anelli *et al.* The TOTEM Experiment at the CERN LHC. *JINST*, 3(S08007), 2008. [39, 75]

[97] The ALICE Collaboration K. Aamodt *et al.* The ALICE Experiment. CERN ALICE Technical Paper, 3 June 2001. [39]

[98] J. F. Grosse-Oetringhaus. PhD thesis, Wilhelms-Universität Münster, 2009. [39, 119]

[99] The ALICE Collaboration K. Aamodt *et al.* ALICE Technical Design Report of the Inner Tracking System. Technical report, CERN, CERN /LHCC 99-012. [39]

[100] A. Kluge G. Aglieri Rinella and M. Krivda. The Level 0 Pixel Trigger system for the ALICE Experiment. *JINST*, 2(P01007), 2007. [43]

[101] The ALICE Collaboration K. Aamodt *et al.* ALICE Technical Design Report of the Time Projection Chamber. Technical report, CERN, CERN /LHCC 2000-001. [44]

[102] L. Musa. Talk to the Technical Board, 14 Sept. 2006. [45]

[103] H. R. Schmidt. The ALICE TPC: Status and Perspectives. *J. Phys. Conf. Series*, 230(012023), 2010. [45]

[104] W. Blum and L. Rolandi. *Particle Detection with Drift Chambers*, chapter 2. Springer-Verlag, 1994. [46]

[105] A. Kalweit for the ALICE Collaboration. Official ALICE Figure. Proc. QM Annecy; To appear in J. Phys. G arXiv:1107.1514v1, 2011. ALI-PERF-4849. [47]

[106] The ALICE Collaboration K. Aamodt *et al.* ALICE Technical Design Report of the Transition Radiation Detector. Technical report, CERN, CERN /LHCC 2001-021. [49]

[107] The ALICE Collaboration K. Aamodt *et al.* ALICE Technical Design Report of the Time Of Flight Detector. Technical report, CERN, CERN /LHCC 2002-016. [49]

[108] E. Scapparone. Private Communication, 27 October 2008. [50]

[109] Y Zoccarato *et al.* Front end electronics and First Results of the ALICE V0 Detector. *Instr. Meth. Phys. Res.*, A(90-96):626–627, 2011. [53]

[110] ALICE ZDC Detector Homepage. The ZDC Detectors. *http://oldsite.to.infn.it/pinot/webcern/webcerndetectors.htm*, 2011. [54]

[111] The ALICE Collaboration K. Aamodt *et al.* ALICE Technical Design Report of the Computing. Technical report, CERN, CERN /LHCC 2005-018. [59]

[112] P. Jovanovic. ALICE CTP Documentation: TooBUSY: a Tool for Monitoring of Subdetectors' BUSY Response. http://epweb2.ph.bham.ac.uk/user/pedja/alice/ctp/ctp.htm, 15 October 2008. [59, 60]

[113] CERN. ROOT. *ROOT Framework; http://root.cern.ch/drupal/*, 2011. [67]

[114] P. Skands. The Perugia Tunes. *Fermilab-CONF-09-113-T*, 2009. [71]

[115] S. Navin *et. al.* Diffraction in PYTHIA. ALICE Internal Note, MCNET-10-09, LUTP-09-23, arXiv:1005.3894 [hep-ph], May 2010. [71, 75]

[116] B. Andersson. *The Lund Model.* Cambridge University Press, 1998. [72]

[117] G. A. Schuler and T. Sjostrand. Hadronic Diffractive Cross Sections and the Rise of the Total Cross section. *Phys. Rev.*, D49(5), 1994. [72]

[118] A. Capella *et al.* Dual Parton Model. *Phys. Rep.*, 236:225, 1994. [74]

[119] F. Abe *et al.*; The CDF Collaboration. The cdf detector: An overview. *Nucl.Instrum.Meth.*, A271(FERMILAB-PUB-88-25-E):387–403, 1988. [75]

[120] G. Aad *et al.*; The ATLAS Collaboration. Rapidity Gap Cross Sections in pp Interactions at $\sqrt{s} = 7$ TeV. *ATLAS Note*, ATLAS-CONF-2011-059, 2011. [75, 116, 154]

[121] The UA5 Collaboration G. J. Alner *et al.* The UA5 experiment. *Physics Reports*, (154):247, 1987. [76]

[122] S. Agostinelli. GEANT Simulation. *Nucl. Instr. and Meth.*, A, 2003. [79]

[123] J. Conrad *et al.* Minimum Bias Triggers in Proton-Proton Collisions with the VZERO and Silicon Pixel Detectors. ALICE Internal Note, ALICE-INT-2005-025, 2005. [80]

[124] F. James. MINUIT. *CERN Prog. Lib.*, D(506), 1998. Long Write-up. [82, 87]

[125] N. De Marco. ZDC For Event Selection. Talk Given at ALICE General First Physics Meeting, 24 October 2008. [84]

[126] G. Luparello. *Performance of the ALICE Zero Degree Calorimeters in pp collisions.* PhD thesis, Universita degli Studi di Torino, 2011. [91]

[127] G. Antchev *et al.* for The TOTEM Collaboration. Proton-proton elastic scattering at the LHC energy of $\sqrt{s}$=7 TeV. *Eur. Phys. Lett.*, 95(41001), 2011. [116]

[128] A. Aamodt *et al.*; The ALICE Collaboration. Charged-particle multiplicity measurement in 7 TeV pp collisions with ALICE at LHC. *Eur. Phys. J.*, C68:345–354, 2010. [117]

[129] S. S. Adler*et al. Phys. Rev.*, C 71(034908), 2005. [117]

[130] E. Darin *et al. Phys. Rev.*, D 65(072005), 2002. [118]

[131] J. Schukraft. Talk for the ALICE Collaboration, ALICE Week, Prague, 2008. [118]

[132] K. Werner. *Nucl. Phys.*, B Proc. Suppl. 175(81), 2008. [118, 145]

[133] K. Werner. On QGP formation in pp collisions at 7 TeV. *Proc. for QM Annecy arXiv:1106.5909v1 [hep-ph]*, 2011. [118, 119]

[134] I. Kraus *et al. Phys. Rev.*, C 76(064903), 2007. [119, 135, 143]

[135] J. Rafelski. Strange Particles from Dense Hadronic Matter. *Acta Physica Polonica*, B27(5), 1996. [119, 143]

[136] F. Prino. ALICE Internal Note, ALICE-INT-2009-026, 2009. [127]

[137] A. Palaha. Pile-up Efficiency. *Presentation for ALICE High Multipicity Effort, June 2010*, 2010. [128, 140, 156]

[138] E. Andersen *et al. Phys. Lett.*, B 433(209), 1998. [135]

[139] B. I. Abelev *et al. Phys. Rev.*, C 77(044908), 2008. [135]

[140] P. Braun-Munzinger A. Andronić and J. Stachel. *Nucl. Phys.*, A 772:167, 2006. [135]

[141] R. Stock. *Phys. Lett.*, B 456:277, 1999. [135]

[142] H. Oeschler I. Kraus, J. Cleymans and K. Redlich. Prospects for strangeness production in pp collisions at LHC. *J. Phys. G: Nucl. Part. Phys.*, 37(094021), 2010. [135, 143]

[143] F. Antinori. Trigger and running preparation. *Presentation for ALICE Week July*, 2009. [139]

[144] A. Aamodt *et al.* for The ALICE Collaboration. Strange particle production in proton-proton collisions at $\sqrt{s}$=0.9 TeV with ALICE at the LHC. *Eur. Phys. J.*, C71(1594), 2011. [141, 147, 156]

[145] K. Aamodt *et al.*; The ALICE Collaboration. Production of pions, kaons and protons in pp collisions at $\sqrt{s} = 900$ GeV with ALICE at the LHC. *Eur. Phys. J*, C71(6):1655, 2011. [141, 156]

[146] P. Fachini. *J. Phys. G: Nucl. Part. Phys.*, 35(044032), 2008. [142]

[147] R. D. Pisarski. *Phys. Lett.*, B 100:55, 1982. [142]

[148] R. Rapp and J. Wambach. *Adv. Nucl. Phys.*, 25(1), 2000. [142]

[149] G. Agakichiev *et al.*; the CERES Collaboration. *Nucl. Phys.*, A661:673, 1999. [142]

[150] F. Antinori *et al. Phys. Lett.*, B 449:401, 1999. [143]

[151] F. Beccattini *et al. J. Phys.*, G 36(064019), 2009. [143]

[152] M. Petran and J. Rafelski. Multistrange particle production and the statistical hadronisation model. *Phys. Rev.*, C82:011901, 2010. [143]

[153] S. Obuko. *Phys. Rev.*, D16:2336, 1977. [143]

[154] H. Lipkin. *Phys. Lett.*, B60:371, 1976. [143]

[155] G. Zweig. *CERN-TH*, 412, 1964. [143]

[156] A. Shor. ϕ Meson Production as a Probe of the Quark-Gluon Plasma. *Phys. Lett.*, 54(11), 1985. [143]

[157] A. Pulvirenti for the ALICE Collaboration. Resonance measurements in pp and Pb-Pb collisions with the ALICE detector. *e-Print arXiv:1106.4230 [hep-ex]*, 2011. [144, 149, 156]

[158] J. D. Tapia Takaki. *Physics Performance Studies for the ALICE Experiment at CERN, LHC.* PhD thesis, University of Birmingham, 2008. [146]

[159] P. Granet. Inclusive Production Cross Sections of Resonances in 32 GeV K^+p Interactions. *Nucl. Phys.*, B140(3):389–408, 1978. [147]

[160] M. Bombara *et al.* AD detector array: Diffractive and Photon-induced physics with ALICE. *ALICE Internal Note*, ALICE-INT-2010-014, 2010. [154]